DESIGN, SYNTHESIS, AND CHARACTERIZATION OF AMPHIPHILIC COLLOIDAL FORMULATIONS FOR BIOMEDICAL AND PERSONAL CARE APPLICATIONS

by

ALYSHA EILEEN MORETTI

A dissertation submitted to the

School of Graduate Studies

Rutgers, The State University of New Jersey

In partial fulfillment of the requirements

For the degree of

Doctor of Philosophy

Graduate Program in Chemistry and Chemical Biology

Written under the direction of

Dr. Kathryn E. Uhrich

And approved by

_____

_____

_____

_____

New Brunswick, New Jersey

OCTOBER, 2017

ABSTRACT OF THE DISSERTATION

Design, synthesis, and characterization of amphiphilic colloidal formulations for biomedical and personal care applications

by ALYSHA EILEEN MORETTI

Dissertation Director:

Kathryn E. Uhrich

Amphiphilic molecules comprised of a hydrophilic and hydrophobic domain are able to self-assemble into a variety of higher order aggregates. These aggregate structures, and their diverse morphologies, have been utilized for the delivery of bioactive agents. Additionally, amphiphiles can be tailored to exhibit inherent bioactivity. This dissertation describes the design and synthesis of amphiphilic molecules that self-assemble into aggregate structures with defined physicochemical properties. Their formulation and biological activity for diverse biomedical and personal care applications are fully characterized.

Amphiphilic macromolecules (AMs) conjugated to ligands known to activate the G-coupled protein receptor TGR5 were investigated as nanoparticle (NP) formulations for the reduction of inflammation in atherosclerotic macrophages. Macrophages propagate the atherosclerotic cascade by uncontrolled internalization of oxidized low-density lipoprotein

(oxLDL) and subsequent secretion of inflammatory cytokines. AMs, based on an acylated sugar backbone conjugated to poly(ethylene glycol) (PEG), were synthesized containing a lithocholic acid (LCA) moiety, a known TGR5 agonist. Ligand-conjugated AMs were formulated into NPs to mitigate the lipid burden and inflammatory phenotype by competitively inhibiting oxLDL uptake through scavenger receptor (SR) interactions and activating the athero-protective receptor TGR5. Ligand-conjugated AM NPs significantly reduce oxLDL uptake compared to untreated controls and lower expression of inflammatory genes under direct control of TGR5. These studies demonstrate the potential of ligand-conjugated AM NPs to reduce the atherosclerotic phenotype in activated macrophages.

Modifications were also made to AMs to enable their incorporation into distearoylphosphatidylcholine- (DSPC-) based liposomes for delivery applications. Liposome use has aided in the bioavailability, solubility, and improved pharmacokinetic profiles of a wide variety of active ingredients for biomedical and personal care products. This work expands upon the AM design to generate two series of molecules that simultaneously stabilize liposome colloidal properties and can be utilized to fine-tune release profiles of encapsulated cargo. Two series of AMs were synthesized with variations in their hydrophobic domains. All AMs improve upon stability properties at storage and physiological temperatures compared to DSPC-based liposomes alone. The chemical features of AMs, particularly the degree of unsaturation in the hydrophobic domain, influence release of hydrophilic molecules from liposomes' interior. Molecular dynamics (MD) simulations reveal that AMs' chemical structures influence local lipid properties, leading to the experimentally observed results. Together, this data offers insight that can be applied to design AMs with desirable physicochemical properties for bioactive delivery.

Small molecule cationic amphiphiles (CAms) were designed to combat the rapid rise in drug resistant bacteria. CAms were designed to target and compromise the structural integrity of bacteria membranes, leading to cell rupture and death. Discrete structural features of CAms were

varied and structure-activity relationship studies were performed to guide the rational design of potent antimicrobials with desirable selectivity and cytocompatibility profiles. In particular, the effect of cationic conformational flexibility, hydrophobic domain flexibility, and hydrophobic domain architecture were evaluated. Their influence on antimicrobial efficacy in Gram-positive and Gram-negative bacteria was determined, and their safety profiles established by assessing their impact on mammalian cells. All CAms have potent activity against bacteria and hydrophobic domain rigidity and branched architecture contribute to specificity. The insights gained from this project will aid in the optimization of CAm structures.

Together, these three primary projects build upon the design of biocompatible amphiphiles that enable the delivery of bioactive molecules. Thorough structure-activity relationship studies were performed in each chapter to identify and generate amphiphiles with desirable outcomes for the specific application.

PREFACE

"Don't tell me the sky is the limit when there are footprints on the moon." -Paul Brandt

DEDICATION

Dedicated to my moon and my stars.

ACKNOWLEDGEMENTS

I would like to express my gratitude for all of my family, colleagues, friends, and mentors who have directly or indirectly aided in the completion of my PhD dissertation. It is your loving support, guidance, intellectual conversation, and positive attitudes that have sculpted me into the person and scientist that I am today.

I would like to specifically thank Dr. Kathryn Uhrich for advising me through my graduate studies, giving me the freedom to develop my scientific intellect, and encouraging me to forge new relationships to further my research. I have particularly valued your strength, courage, and positive outlook. Your approach to tackling challenges in your career path will continue to serve as a model as I encounter challenges of my own. You truly are an inspiration.

My committee members, Dr. Larry Romsted, Dr. Jean Baum, and Dr. Laurie Joseph have been an integral part of my professional development, and I am grateful for the time you all have dedicated to helping me grow and learn. You have offered invaluable insight into my research projects, facilitated the development of those projects, and aided in the acquisition of my technical understanding and skillsets that will be invaluable as I embark upon my future endeavors.

A special thanks is also necessary for my collaborators and individuals that have aided in the fruition of the research projects that have shaped my dissertation. Without your help, this would not be possible. You have helped me learn that true science is accomplished through collaboration. Thank you Dr. Prabhas Moghe, Dr. Michael Chikindas, Dr. Meenakshi Dutt, Dr. Charles Roth, Dr. Grace Guo, Rebecca Chmielowski, Richard (Matt) Weeks, Bin Zhang, Qi (Ricky) Li, Dr. Daniel Lewis, Dr. Latrisha Petersen, Dr. Bo Kong, Runbin Sun, Jackie Sikora, Ana Monica Nunes.

I would also like to thank Dr. Loyd Bastin for his guidance though my undergraduate education. Your open and accepting attitude enabled me to develop my own ideas and challenge scientific concepts. Exposing me to research at the undergraduate level initiated the drive that led

to this dissertation. It goes without saying that you have been, and continue to be, one of the most caring and thought-provoking advisors and mentors that a student could ask for.

I would like to extend my thanks to my loving and supportive family. In particular, my parents, Kim and Les, have been my primary source of motivation to succeed. It is your daily encouragement and praise that has provided the foundation for this work. I would like to thank my grandparents, Vera, Les, and the late, but beloved Joan, who I truly feel believe in me the most. I will forever be grateful for your unconditional support and faith. I would also like to acknowledge the love and support of my Aunt Eileen and Zia who have encouraged me along the way.

The family I have built over the years, Cory, Roslyn, and Khaleesi, have been the core of my support and encouragement throughout this journey. It is your patience through the dinnerless nights, the early morning wakings, the weekend absences, and the untended to home that have made this possible. Your unconditional love and acceptance has allowed me to focus and remain motivated through the years. I truly appreciate all that you have given in support of my intellectual and personal growth. It will never be taken for granted.

I would also like to thank my peers and mentors that I have worked with in both my undergraduate and graduate studies. Your fun and welcoming personalities have made the experience enjoyable and fruitful. I would like to extend a special thanks to Kevin Blattner, Michael Polen, Chris Annunziato, Dr. Nicholas Stebbins, Dr. Allison Faig, Dr. Jon Faig, Dr. Yingyue (Joanna) Zhang, Dr. Jennifer Chan, Dr. Jeannette Marine, Dr. Jason Hackenberg, Stephan Bien-Aime, Dania Davie, Ning Wang, Dr. Ruslan Guliyev, Dr. Renxun Chen, Dr. Vidya Ganapathy, Harini Kantamneni, Dr. Margot Zevon, Daniel Martin, Nanxia Zhao, Gabriella Composto, Enoch Yue, Courtney Amster, James Sharp, Yeseo Han, Drym Oh, Bernice Lee, Dr. Louise Liable-Sands, Dr. Andrea Martin, and Dr. Scott Van Bramer.

Finally, I would like to thank all of Rutgers University faculty and staff members. Your assistance has not gone unappreciated. Thanks Allison Larkin, Arielle L'Esperance, Karen Fowler, Ann Doeffinger, Dr. Shan Wan, Kate Krueger, Dr. Gail Ferstanding-Arnold. I must also thank the National Institute of Health, U.S. Department of Education, and Rutgers University for financial support. For those not mentioned, please know that your assistance and support has not gone unnoticed.

TABLE OF CONTENTS

LIST OF TABLES

LIST OF ILLUSTRATIONS

LIST OF ABBREVIATIONS

[(M+2)/2]	Mass plus two, divided by two
[M-1]	Mass minus one
[M+1]	Mass plus one
[M+23]	Mass plus sodium
2-MeTHF	2-Methyltetrahydrofuran
%	Percent
˚	Degrees
˚C	Degrees Celsius
±	Plus or minus
~	Approximately
$	Dollars
^{13}C	Carbon (when describing NMR)
^{1}H	Proton (when describing NMR)
α	Alpha
Å	Angstrom
ABCA1	Adenosine Triphosphate Binding Cassette Transporter A1
AcOH	Acetic Acid
AIDS	Acquired Autoimmunodeficiency Syndrome
AM	Amphiphilic macromolecule
AMP	Antimicrobial peptide
amu	Atomic Mass Unit
AOT	Aerosol octoyl
ApoA1	Apolipoprotein A1
Boc	Tert-butyloxycarbonyl
B	Beta
b	Block
br	Broad
C	Apolar
CAm	Cationic Amphiphilic Molecule
cAMP	Cyclic Adenosine Monophosphate
C=O	Carbonyl
CD36	Scavenger receptor B
CD_3OD	Deuterated methanol
$CDCl_3$	Deuterated chloroform
CFU	Colony forming units
CG	Course Grained
$CHCl_3$	Chloroform
cm^{-1}	Wavenumber units
CMC	Critical micelle concentration
COMU	(1-Cyano-2-ethoxy-2-oxoethylidenaminooxy)dimethylamino-morpholino-carbenium hexafluorophosphate
CPME	Cyclopentylmethylether
CRE	Cyclic Adenosine Monophosphate Response Element
d	Doublet, day
Da	Dalton
DBT	Dibenzyl tartrate
DCC	Dicyclohexyl carbodiimide
DCM	Dichloromethane

d of d	Doublet of doublets
DiO	3,3'-dioctadecyl oxacarbocyanine
DLS	Dynamic light scattering
DMAP	4-dimethylamino pyridine
DMEM	Dulbecco's Modified Eagle's Medium
DMF	Dimethylformamide
DMSO-d_6	Deuterated dimethyl sulfoxide
DNA	deoxyribonucleic acid
DOPC	1,2-dioleoyl-sn-glycero-3-phosphocholine
DOPE	1,2-dioleoyl-sn-glycero-3-phosphoethanolamine
DOPG	1,2-dioleoyl-sn-glycero-3-phospho-(1'-rac-glycerol)
DOTAP	1,2-dioleoyl-3-trimethylammonium-propane
DPPC	Dipalmitoyl-phosphatidylcholine
DPTS	4-(dimethylamino) pyridinium 4-toluene sulfonate
DSPC	disteroyl-phosphatidylcholine
DTT	Dithiothreitol
EDC	1-ethyl-3-(3-dimethyl aminopropyl)carbo diimide
EDTA	Ethylenediaminetetraacetic acid
eq	Equivalents
ESI	Electrospray ionization
FBS	Fetal bovine serum
FNP	Flash Nanoprecipitation
FT-IR	Fourier transform infrared spectroscopy
FXR	Farnesoid X Receptor
g	g-force
g	Gram
G-	Gram-negative
G+	Gram-positive
GPBAR-1	G-Protein Coupled Bile Acid Receptor- 1
GPC	Gel permeation chromatography
h	Hour
H	Proton
H_2	Hydrogen gas
H_2O	Water
H_2SO_4	Sulfuric Acid
HC_{50}	Percent Required for 50 Percent Hemolysis
HCl	Hydrochloric acid
HEK	Human Embryonic Kidney
HEPES	4-(2-hydroxyethyl)-1-piperazineethane sulfonic acid
HLB	Hydrophilic-Lipophilic Balance
HMDM	Human monocyte-derived macrophage
HMG-CoA	3-hydroxy-3-methyl-glutaryl-coenzyme A
HPLC	High pressure liquid chromatography
HSPC	Hydrogenated Soy phosphatidylcholine

I	Intensity
IL	Interleukin
K_2CO_3	Potassium carbonate
KBr	Potassium bromide
kDa	Kilodalton
$KHSO_4$	Potassium bisulfite
KOH	Potassium hydroxide
L	Liter
LAMMPS	Large-scale Atomic/Molecular Massively Parallel Simulator
LCA	Lithocholic Acid
LDL	Low-density lipoprotein
LJ	Lennard-Jones
LPS	Lipopolysaccharide
Luc	Luciferase
LUV	Large unilamellar vesicle
LXR	Liver X Receptor
M	Molar
m	Multiplet
M2	Macrophage Phenotype 2
MCP-1	Monocyte chemoattractant protein 1
M-CSF	Macrophage colony-stimulating factor
MD	Molecular Dyanmics
m/z	Mass-to-charge ratio
MeOH	Methanol
MES	2-(N-morpholino) ethanesulfonic acid
MFI	Mean fluorescence intensity
mg	Milligram
$MgSO_4$	Magnesium sulfate
MHz	Megahertz
MIC	Minimum inhibitory concentration
min	Minute
mL	Milliliter
mm	Millimeter
mM	Millimolar
mmol	Millimole
MMP	Matrix Metalloproteinase
MOPS	(3-(N-morpholino) propanesulfonic acid
mPEG-NH_2	Monomethoxy-poly(ethylene glycol)-amine
MS	Mass spectrometry
Mw	Weight averaged molecular weight
N	Nitrogen, Non-polar
N_2	Nitrogen gas
Na_2CO_3	Sodium carbonate
$NaHCO_3$	Sodium bicarbonate
ng	Nanogram
NHS	N-hydroxysuccinimide
nm	Nanometer
NMR	Nuclear magnetic resonance
NP	Nanoparticle
ns	nanosecond
OD	Optical Density
oxLDL	Oxidized low-density lipoprotein
P	Polar

PCR	Polymerase Chain Reaction
PBMC	Peripheral blood mononuclear cell
PBS	Phosphate buffered saline
Pd/C	Palladium on carbon
PDI	Polydispersity index
PEG	Poly(ethylene glycol)
PPARɣ	Peroxisome Proliferator-Activated Receptor Gamma
ppm	Parts per million
PS	Polystyrene
PTFE	Polytetrafluoroethylene
Q	Charged
quin	Quintet
RNA	ribonucleic acid
rpm	Revolutions per minute
RPMI	Roswell Park Memorial Institute
RXR	Retinoid X Receptor
RT	Room temperature
s	Singlet, second
SDS	Sodium dodecyl sulfate
SI	Selectivity Index
SN2	Nucleophilic substitution 2
SRA	Scavenger receptor A
SRB	Sulforhodamine B
SREBP1	Sterol Regulatory Element Binding Protein 1
t	Triplet
TBAF	Tetra-n-butylammonium fluoride
TBDMS	Tert-butyldimethylsilyl
TEA	Triethylamine
TFA	Trifluoroacetic acid
TGR5	Transmembrane G-Coupled Protein Receptor 5
THF	Tetrahydrofuran
TLC	Thin layer chromatography
Tm	Melting temperature
TMS	Trimethylsilane
TNFα	Tumor Necrosis Factor Alpha
UV-Vis	Ultraviolet-visible
vs.	versus
w/w	Weight by weight
wt %	Weight percent
X	times
$ZnCl_2$	Zinc Chloride
δ	Chemical shift
µg	Microgram
µL	Microliter
µM	Micromolar
ζ	Zeta

1. INTRODUCTION

1.1 Amphiphilic Molecules

Amphiphiles are molecules that have discrete hydrophobic and hydrophilic domains (**Figure 1.1**) covalently bonded together [1-3]. Amphiphilic molecules can have varying chemical structures and architectures as shown in the examples presented in **Figure 1.1**. Conventional amphiphiles have a single hydrophilic, polar group that varies in identity (e.g., sulfate, ammonium, zwitterion, alcohol) and is covalently attached to a hydrocarbon chain, saturated or unsaturated, of variable length [4, 5]. This general structure is often depicted as a spherical polar head group attached to a long wavy line representing the alkyl hydrophobic domain as shown in **Figure 1.1**. Although this general structure captures the essence of amphiphiles, they vary greatly in chemical structure [1, 3, 6]. Despite their diversity, all amphiphiles are comprised of a hydrophobic domain that can be linear, branched, or cyclic. The water-soluble hydrophilic domains of amphiphiles are also variable and can be charged or neutral. Additionally, amphiphiles are not limited to small molecules and can be polymeric in nature [1, 5]. For example, the hydrophilic domains of many polymeric amphiphiles consist of poly(ethylene glycol) (PEG), such as those found in Pluronics®, which is frequently used to aid hydrophobic polymer block solubilization [5].

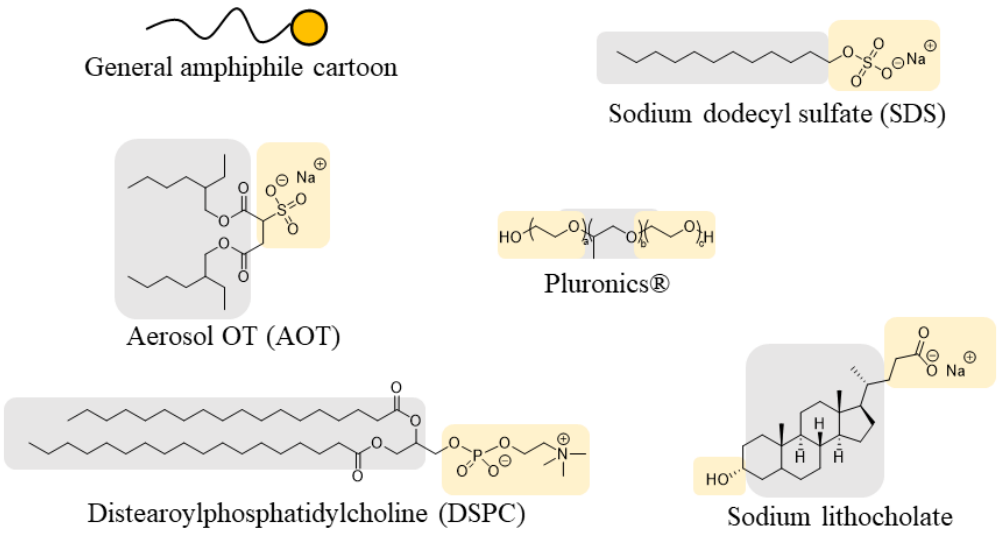

Figure 1.1: Representative structures of amphiphiles. Hydrophilic domains are highlighted in yellow and correlate to the yellow sphere in the general head/tail amphiphile cartoon. Hydrophobic domains are highlighted in grey and correspond to the waved line in the general amphiphile cartoon.

1.2 Amphiphile Self-Assembly

Amphiphilic molecules have the innate ability to self-assemble into a variety of higher order aggregate structures in aqueous solutions [2, 3, 7]. When the concentration of amphiphiles reaches a specific value, known as the critical micelle concentration (CMC), they begin a self-assembly process to maximize the entropy of the bulk water [2, 3]. This is a dynamic process driven by non-covalent interactions (e.g., hydrogen bonding, the hydrophobic effect) that results in aggregate morphologies specific to the different amphiphile characteristics, namely the packing parameter [8, 9]. The packing parameter is a metric that calculates the relationship between the volume and length of the surfactant tail and the surface area of the headgroup in the aggregate structure at equilibrium. This parameter can be used to predict or describe the size and shape of the supramolecular structure that the aggregate will form at a particular concentration [8, 9] (**Figure 1.2**). Although the packing parameter serves as a tool to understand the self-assembly process,

aggregate morphologies can also greatly vary depending on temperature, pH, ionic strength, and the presence of other organic molecules (e.g., other amphiphiles) [10-12]. This thesis will focus on dynamic micelles and lamellar supramolecular architectures, in addition to kinetically trapped nanoparticles (NPs). At concentrations above the CMC, micelles occur where the hydrophilic domains of amphiphiles are in contact with water, and the hydrophobic domains are shielded in the core of the aggregate structure from the aqueous environment. A common example is sodium dodecyl sulfate (SDS), which forms spherical micelles at room temperature above 8-10 mM [13]. Lamellar vesicle structures, also called liposomes, result when amphiphiles form a spherical curved bilayer structures in which hydrophobic tails are also shielded from water [7, 14]. Liposomes have an aqueous core, hydrophobic bilayer interior, and hydrophilic groups that are in contact with both the aqueous vesicle core and the surrounding bulk exterior [7]. Liposomes often result from the dissolution of phospholipids, such as distearoylphosphatidyl choline (DSPC), in water [7].

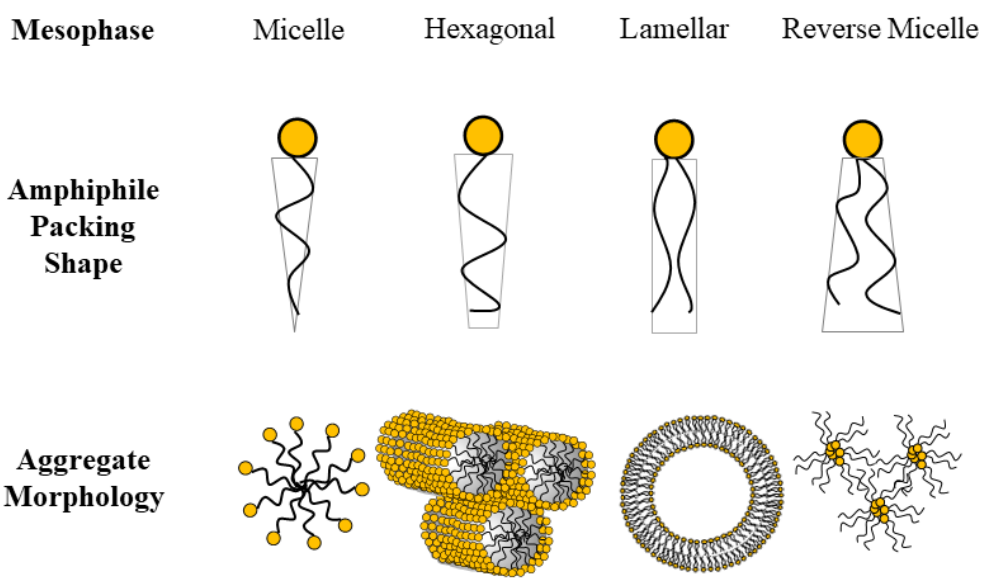

Figure 1.2: Schematic describing the relationship between amphiphile packing shape and aggregate morphology [3, 9, 15]. Hydrophilic head group is shown in yellow and hydrophobic tails are shown in black. Depicted are amphiphiles with a cone-like packing shape and corresponding spherical micelle structure, truncated cone-like packing shape and corresponding cylindrical hexagonal morphology, double-tailed rectangular packing shape and corresponding lamellar vesicle aggregate, and truncated inverse cone-like amphiphile shape and corresponding reverse micelle structures.

NPs that are described in this thesis are formed via a flash nanoprecipitation (FNP) procedure (**Figure 1.3**) [16]. FNP occurs when an organic stream containing a compatible hydrophobe and amphiphile are rapidly injected and mixed with an aqueous stream. The hydrophobe precipitates from solution and the amphiphile surrounds the precipitate forming kinetically trapped NPs. NPs formed through this process are not susceptible to dissociation by solution dilution and have demonstrated colloidal stability over extended time periods (i.e., several months) [16-18].

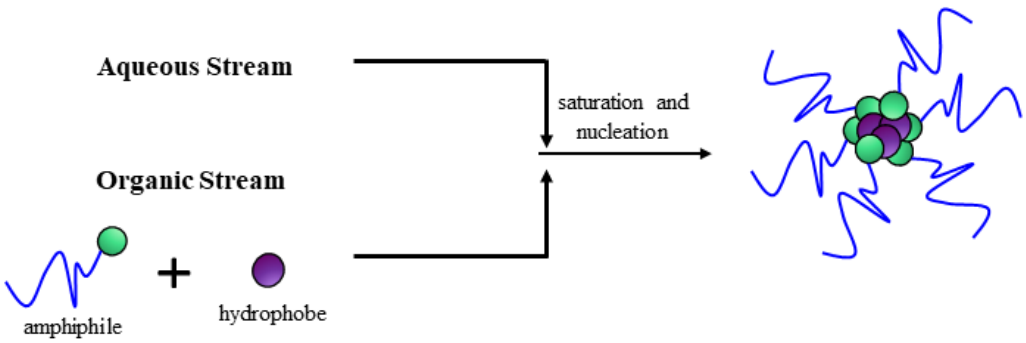

Figure 1.3: FNP process by which kinetically trapped NPs are formed. An amphiphile (hydrophobic domain shown in green, hydrophilic domain shown in blue) and a hydrophobe (shown in purple) are dissolved in an organic solution and rapidly mixed with an aqueous stream in a confined impinging jet mixer to generate NPs.

1.3 Applications of Amphiphilic Molecules

The chemical structure of amphiphilic molecules and their resulting aggregate structure have led to a variety of applications, both natural and commercial. Naturally existing amphiphiles, particularly lipids and peptides/proteins, form the structures that allow for life to exist. Lipids assemble in the plasma membrane structure that encloses most organisms, from humans to single-cell bacteria, as well as the intracellular vesicles that transport materials required for survival [19]. Proteins are formed by sequences of amino acids and can be both amphiphilic in primary structure or amphipathic in their folded forms [6, 20]. It is the unique, often self-assembled, structures of proteins that results in their discrete functions and specificity for particular ligands [6, 21, 22]. A relevant example of amphipathic peptides, known as antimicrobial peptides (AMPs), are synthesized in nearly all organisms as part of the innate immune response to combat bacterial infections [23, 24]. AMPs form facially amphipathic secondary structures that allow for electrostatic and hydrophobic interactions with the negatively charged molecules of bacterial cell membranes, leading to a loss of membrane integrity and bacterial lysis [24]. This secondary

structure only occurs in the presence of negatively charged bacterial membranes, and thus elicits a specific effect over host cell membranes [24].

Although extremely diverse in nature, synthetic approaches have enabled the development of amphiphilic molecules that are used for bioactive delivery in medicine, nutrition, detergents, and emulsifiers in personal care and cosmetic products [25-28]. In pharmaceutical delivery applications, micellar and liposomal vehicles aid in the solubilization of otherwise insoluble drugs, thereby improving their bioavailability [27]. Additionally, the use of delivery vehicles has drastically improved the delivery of cancer drugs to tumor sites, as their size results in preferential accumulation at tumor sites via the enhanced permeability and retention (EPR) effect [29]. A notable example is the development of Doxil®, a PEG-liposome based delivery vehicle for doxorubicin. Doxil® has been shown to improve the bioavailability of doxorubicin and improve patient outcomes as an approved treatment for metastatic breast cancer [30, 31]. Amphiphilic molecules have a wide range of applications owing to their structural diversity and ability to self-assemble into numerous aggregate structures. As such, this thesis outlines the design and evaluation of novel amphiphilic molecules for biomedical and personal care applications.

1.4 Specific Projects

1.4.1. Ligand Conjugated Amphiphilic Macromolecules Reduce Inflammation as Macrophage-Targeted Nanotherapeutics

Cardiovascular disease begins with atherosclerosis, in which unregulated internalization of oxidized low-density lipoprotein (oxLDL) occurs in macrophages, leading to foam cell formation, fatty streaks, and arterial plaques [32]. The Uhrich group has designed several series of amphiphilic macromolecules (AMs) that reduce lipid loading in macrophages by competitively interacting with scavenger receptors (SRs), the primary pathway of oxLDL uptake (**Figure 1.4**) [17, 33-36]. The

hydrophobic domain of AMs, comprised of a linear sugar backbone acylated with fatty acid pendants, is conjugated to PEG to serve as the hydrophilic segment [33, 34].

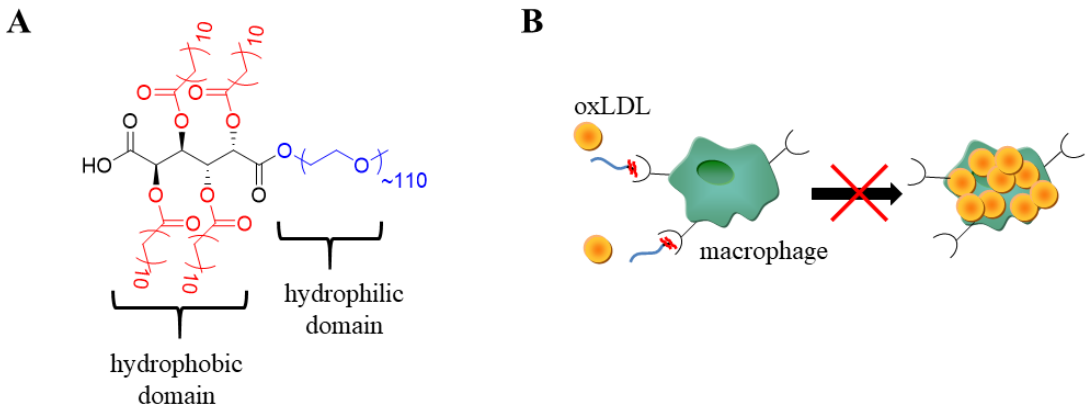

Figure 1.4: Chemical structure of lead AM in treatment of atherosclerotic phenotypes highlighting hydrophobic and hydrophilic domains (A). AMs competitively interact with SRs on macrophages to prevent the uncontrolled uptake of oxLDL (B).

The amphiphilic nature of AMs enables their self-assembly into nanoscale micelles at low CMCs, as well as the generation of NPs via the aforementioned FNP process. Previously designed AM NPs with a core/shell design showed elevated potency to counteract oxLDL uptake in atherosclerotic macrophages compared to micellar counterparts, but elicited inherent inflammation and failed to address inflammation associated with the disease phenotype [17, 35]. One approach to minimize this effect is to activate a receptor known to counteract inflammation, such as the G-protein coupled receptor TGR5 [37]. Lithocholic acid (LCA), a natural TGR5 agonist was incorporated into AMs to simultaneously reduce macrophage lipid burden and pro-inflammatory cytokine secretion. LCA was conjugated to AMs for favorable interaction with TGR5 and was also hydrophobically modified to enable NP core encapsulation. Conjugates were formulated into negatively charged NPs with different core/shell combinations, mimicking oxLDL. NPs with LCA-containing shells exhibited reduced sizes, and all NPs reduced oxLDL uptake to <30% of untreated

controls, while slightly downregulating SR expression. Pro-inflammatory cytokine expression known to be influenced by TGR5, including IL-1β, IL-8, and IL-10, was strongly dependent on NP composition, with LCA-modified cores most strongly downregulating inflammation. LCA-conjugated AM NPs offer a unique approach to minimize atherogenesis and counteract inflammation by simultaneously reducing oxLDL uptake and mitigating the inflammatory phenotype (**Figure 1.5**).

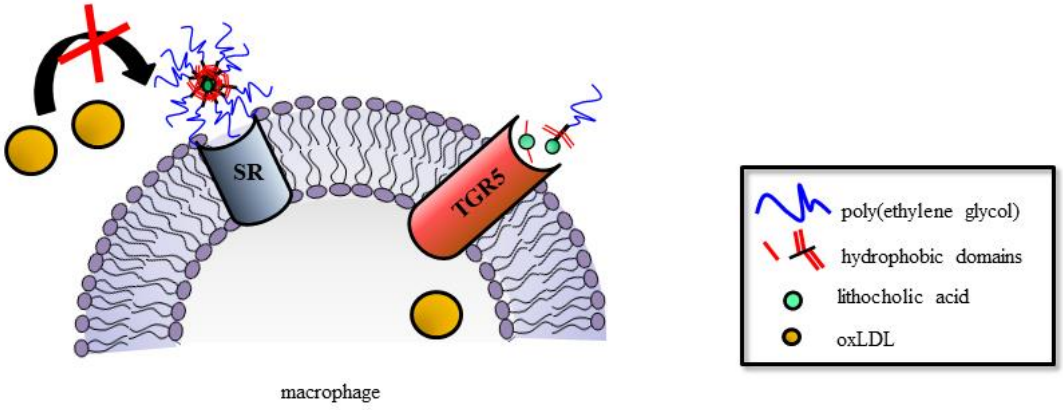

Figure 1.5: Schematic representation of hypothesized mechanism by which LCA-conjugated NPs reduce inflammation and prevent oxLDL uptake in activated macrophages. NPs are shown having the dual capacity to inhibit oxLDL uptake by competitively binding to scavenger receptors and lower inflammation by dissociating into unimers and agonizing TGR5.

1.4.2. Amphiphilic Macromolecules' Degree of Unsaturation and Backbone Orientation Influence Local Lipid Properties in Liposomes

Liposomes have become increasingly common in the delivery of bioactive agents due to their ability to encapsulate hydrophobic and hydrophilic drugs with excellent biocompatibility [14]. While commercial liposome formulations improve bioavailability of otherwise quickly eliminated or insoluble drugs, liposomal delivery systems may still suffer from poor drug retention and

colloidal stability [38, 39]. In an effort to overcome these difficulties, complex formulations that include a variety of excipients for different purposes are often employed. As an example, PEGylated lipids are commonly used to provide steric stabilization against liposome aggregation, while formulation with hydrogels is often used to achieve sustained drug release rates [40, 41].

Two series of AMs consisting of acylated polyol backbones conjugated to PEG were designed, synthesized, and characterized in this work. These AMs can serve as the sole additives to stabilize and control hydrophilic molecule release rates from DSPC-based liposomes. As compared to DSPC alone, all AMs stabilize liposomes at low incorporation ratios, and the AM's degree of unsaturation and hydrophobe conformation have profound impacts on stability duration. The AM's chemical structures, particularly hydrophobe unsaturation, also impact the rate of hydrophilic drug release, presumably due to changes in local lipid properties (**Figure 1.6**). Course-grained molecular dynamics simulations were utilized to better understand the influence of AM structure on lipid properties and potential liposomal stabilization. Results indicate that both hydrophobic domain structure and PEG density can be utilized to fine-tune liposome properties for the desired application. Collectively, AMs demonstrate potential to simultaneously stabilize and control the release profile of hydrophilic cargo.

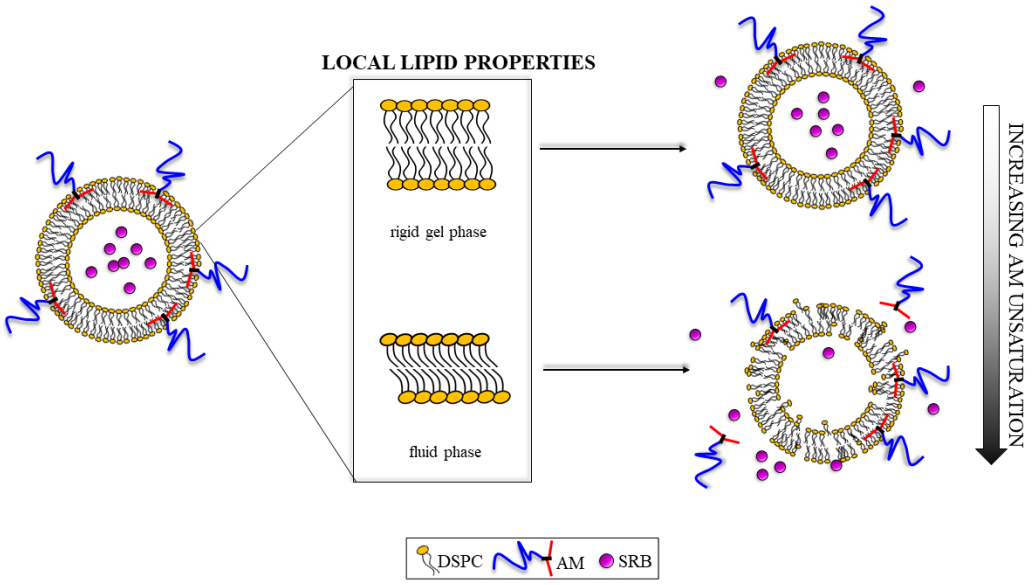

Figure 1.6: Schematic representation describing AMs effect on local lipid properties in DSPC liposomes. AMs with higher degrees of unsaturation cause more significant disruptions in bilayer packing, leading to liposome dissociation, aggregation, and increased permeability. These effects lead to a quicker rate of sulforhodamine B (SRB) dye release from vesicles compared to liposomes with completely saturated AMs.

1.4.3. Cationic Amphiphiles as Antimicrobial Peptide Mimics: Flexibility and Architecture Influence Membrane Activity and Specificity Against Bacteria

The misuse and overuse of antibiotics has led to a rise in multi-drug resistant bacteria and a need for alternatives to traditional antibiotics [42]. AMPs have a unique ability to specifically target and damage bacterial membranes, making it difficult for bacteria to develop resistance via genetic mutations [23, 24]. As such, widespread interest in AMPs has focused on identifying structural features that contribute to their bacterial potency and limited toxicity towards mammalian cells [43, 44].

Small molecule cationic amphiphiles (CAms) were designed and synthesized as AMP mimics that consist of an alkylated sugar backbone modified with amine functionalities. Structure-activity relationship studies guided the optimization of CAm structures, as the contribution of the cationic conformational flexibility, combinatorial effects of cationic and hydrophobic domain flexibility, and branched hydrophobic domain architecture to antibacterial activity were evaluated (**Figure 1.7**). Several key features that impart CAms with high potency against representative Gram-negative and Gram-positive bacteria have been identified by evaluating their minimum inhibitory concentrations (MICs). Hemolysis and cytotoxicity studies were further used to determine the safety profile of CAms, and their selectivity for bacteria cells over mammalian cells was elucidated via *in vitro* assays with model vesicles mimicking mammalian and bacteria cellular membrane components. Results indicate that CAm charge flexibility is a significant structural feature that contributes to toxicity against Gram-negative bacteria, the combinatorial effect of charge and hydrophobic flexibility influence the safety profile of CAms, and branched architecture resulted in high potency against Gram-negative bacteria. Lead compounds have MICs in the micromolar range and are cytocompatible, demonstrating promise for CAms use as antibiotic alternatives.

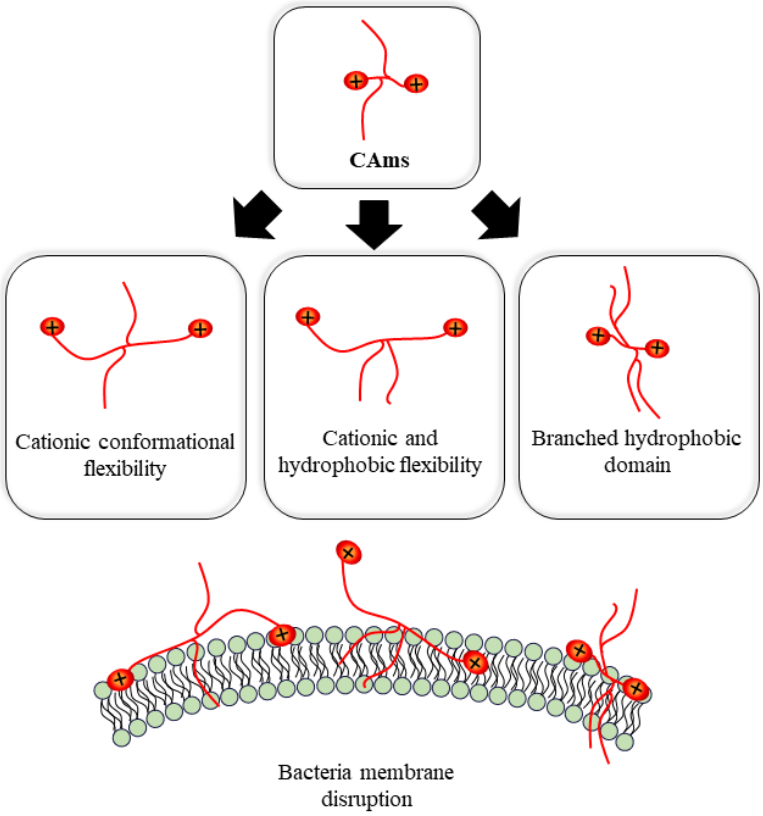

Figure 1.7: Schematic representation of CAms' structural variations that may lead to differences in bacteria membrane interactions and antimicrobial potency. CAms are depicted with extended linker lengths between the cationic charge and the backbone to increase cationic conformational flexibility (left), a combination of conformational cationic flexibility and hydrophobic domain flexibility (center), and branched architecture in the hydrophobic domain (right).

1.5 Summary

Amphiphilic molecules lend themselves to numerous applications. When tailoring amphiphiles for particular applications, it is critical to understand how chemical features alter self-assembly characteristics, interactions with other molecules (e.g., membranes, proteins), and ultimately, their desired activity. By systematically altering structural elements of the amphiphilic molecules herein, systems were developed that exhibit desirable outcomes in combating

atherogenesis, achieving liposomal colloidal stability and controlled release, and targeting and disrupting bacterial membranes over host cells.

1.6 References

[1] Alexandridis P, Lindman B. Amphiphilic block copolymers: self-assembly and applications: Elsevier; 2000.

[2] Lombardo D, Kiselev M, magazù S, Calandra P. Amphiphiles Self-Assembly: Basic Concepts and Future Perspectives of Supramolecular Approaches2015.

[3] Romsted LS. Introduction to Surfactant Self-Assembly. Supramolecular Chemistry: From Molecules to Nanomaterials. 2012.

[4] Rosen MJ, Kunjappu JT. Surfactants and interfacial phenomena: John Wiley & Sons; 2012.

[5] Holmberg K, Jönsson B, Kronberg B, Lindman B. Surfactants and polymers in aqueous solution: Wiley Online Library; 2002.

[6] Whitesides GM, Grzybowski B. Self-Assembly at All Scales. Science. 2002;295:2418-21.

[7] Marsh D. Thermodynamics of phospholipid self-assembly. Biophysical journal. 2012;102:1079-87.

[8] Israelachvili JN, Mitchell DJ, Ninham BW. Theory of self-assembly of hydrocarbon amphiphiles into micelles and bilayers. Journal of the Chemical Society, Faraday Transactions 2: Molecular and Chemical Physics. 1976;72:1525-68.

[9] Nagarajan R. Molecular Packing Parameter and Surfactant Self-Assembly: The Neglected Role of the Surfactant Tail. Langmuir. 2002;18:31-8.

[10] Raghavan SR, Fritz G, Kaler EW. Wormlike micelles formed by synergistic self-assembly in mixtures of anionic and cationic surfactants. Langmuir. 2002;18:3797-803.

[11] Sorrenti A, Illa O, Ortuno R. Amphiphiles in aqueous solution: Well beyond a soap bubble. Chemical Society Reviews. 2013;42:8200-19.

[12] Savelli G, Germani R, Brinchi L. Reactivity control by aqueous amphiphilic self-assembling systems. Surfactant Science Series. 2001:175-246.

[13] Mukerjee P, Mysels KJ. Critical micelle concentrations of aqueous surfactant systems. National Standard reference data system; 1971.

[14] Akbarzadeh A, Rezaei-Sadabady R, Davaran S, Joo SW, Zarghami N, Hanifehpour Y, et al. Liposome: classification, preparation, and applications. Nanoscale Research Letters. 2013;8:102-.

[15] Stuart MC, Boekema EJ. Two distinct mechanisms of vesicle-to-micelle and micelle-to-vesicle transition are mediated by the packing parameter of phospholipid–detergent systems. Biochimica et Biophysica Acta (BBA)-Biomembranes. 2007;1768:2681-9.

[16] Johnson BK, Prud'homme RK. Flash nanoprecipitation of organic actives and block copolymers using a confined impinging jets mixer. Australian Journal of Chemistry. 2003;56:1021-4.

[17] York AW, Zablocki KR, Lewis DR, Gu L, Uhrich KE, Prud'homme RK, et al. Kinetically Assembled Nanoparticles of Bioactive Macromolecules Exhibit Enhanced Stability and Cell-Targeted Biological Efficacy. Advanced Materials. 2012;24:733-9.

[18] Zhang C, Pansare VJ, Prud'Homme RK, Priestley RD. Flash nanoprecipitation of polystyrene nanoparticles. Soft Matter. 2012;8:86-93.

[19] Cooper GM. Structure of the Plasma Membrane. The Cell: A Molecular Approach. 2 ed. Sunderland MA: Sinauer Associates; 2000.

[20] Cui H, Webber MJ, Stupp SI. Self-assembly of peptide amphiphiles: from molecules to nanostructures to biomaterials. Biopolymers. 2010;94:1-18.

[21] Weisel M, Proschak E, Kriegl JM, Schneider G. Form follows function: shape analysis of protein cavities for receptor-based drug design. Proteomics. 2009;9:451-9.

[22] Gao M, Skolnick J. The distribution of ligand-binding pockets around protein-protein interfaces suggests a general mechanism for pocket formation. Proceedings of the National Academy of Sciences. 2012;109:3784-9.

[23] Ganz T. Defensins: antimicrobial peptides of innate immunity. Nature reviews immunology. 2003;3:710-20.

[24] Hancock RE, Diamond G. The role of cationic antimicrobial peptides in innate host defences. Trends in microbiology. 2000;8:402-10.

[25] Goddard ED, Gruber JV. Principles of polymer science and technology in cosmetics and personal care: CRC Press; 1999.

[26] Keller BC. Liposomes in nutrition. Trends in Food Science & Technology. 2001;12:25-31.

[27] Kataoka K, Harada A, Nagasaki Y. Block copolymer micelles for drug delivery: design, characterization and biological significance. Advanced drug delivery reviews. 2001;47:113-31.

[28] Drummond CJ, Fong C. Surfactant self-assembly objects as novel drug delivery vehicles. Current opinion in colloid & interface science. 1999;4:449-56.

[29] Maeda H, Wu J, Sawa T, Matsumura Y, Hori K. Tumor vascular permeability and the EPR effect in macromolecular therapeutics: a review. Journal of controlled release. 2000;65:271-84.

[30] Torchilin V. Tumor delivery of macromolecular drugs based on the EPR effect. Advanced Drug Delivery Reviews. 2011;63:131-5.

[31] Gabizon A, Shmeeda H, Barenholz Y. Pharmacokinetics of pegylated liposomal doxorubicin. Clinical pharmacokinetics. 2003;42:419-36.

[32] Moore KJ, Tabas I. Macrophages in the pathogenesis of atherosclerosis. Cell. 2011;145:341-55.

[33] Chnari E, Nikitczuk JS, Uhrich KE, Moghe PV. Nanoscale anionic macromolecules can inhibit cellular uptake of differentially oxidized LDL. Biomacromolecules. 2006;7:597-603.

[34] Chnari E, Nikitczuk JS, Wang J, Uhrich KE, Moghe PV. Engineered polymeric nanoparticles for receptor-targeted blockage of oxidized low density lipoprotein uptake and atherogenesis in macrophages. Biomacromolecules. 2006;7:1796-805.

[35] Lewis DR, Petersen LK, York AW, Ahuja S, Chae H, Joseph LB, et al. Nanotherapeutics for inhibition of atherogenesis and modulation of inflammation in atherosclerotic plaques. Cardiovascular research. 2015;109:283-93.

[36] Lewis DR, Petersen LK, York AW, Zablocki KR, Joseph LB, Kholodovych V, et al. Sugar-based amphiphilic nanoparticles arrest atherosclerosis in vivo. Proceedings of the National Academy of Sciences. 2015;112:2693-8.

[37] Pols TW, Nomura M, Harach T, Sasso GL, Oosterveer MH, Thomas C, et al. TGR5 activation inhibits atherosclerosis by reducing macrophage inflammation and lipid loading. Cell metabolism. 2011;14:747-57.

[38] Sercombe L, Veerati T, Moheimani F, Wu SY, Sood AK, Hua S. Advances and Challenges of Liposome Assisted Drug Delivery. Frontiers in Pharmacology. 2015;6:286.

[39] Moghimi SM, Szebeni J. Stealth liposomes and long circulating nanoparticles: critical issues in pharmacokinetics, opsonization and protein-binding properties. Progress in Lipid Research. 2003;42:463-78.

[40] Nag OK, Awasthi V. Surface engineering of liposomes for stealth behavior. Pharmaceutics. 2013;5:542-69.

[41] Paavola A, Kilpeläinen I, Yliruusi J, Rosenberg P. Controlled release injectable liposomal gel of ibuprofen for epidural analgesia. International journal of pharmaceutics. 2000;199:85-93.

[42] Llor C, Bjerrum L. Antimicrobial resistance: risk associated with antibiotic overuse and initiatives to reduce the problem. Therapeutic advances in drug safety. 2014;5:229-41.

[43] Locock KE, Michl TD, Valentin JD, Vasilev K, Hayball JD, Qu Y, et al. Guanylated polymethacrylates: a class of potent antimicrobial polymers with low hemolytic activity. Biomacromolecules. 2013;14:4021-31.

[44] Lind TK, Polcyn P, Zielinska P, Cárdenas M, Urbanczyk-Lipkowska Z. On the antimicrobial activity of various peptide-based dendrimers of similar architecture. Molecules. 2015;20:738-53.

2. CHAPTER 1: LIGAND CONJUGATED AMPHIPHILIC MACROMOLECULES REDUCE INFLAMMATION AS MACROPHAGE-TARGETED NANOTHERAPEUTICS

[This work is in preparation for publication under the title: "Lithocholic acid-based amphiphilic macromolecules: Macrophage-targeted nanotherapeutics reduce inflammation in atherosclerosis." Qi Li, Rebecca Chmielowski, Laurie B. Joseph, Prabhas V. Moghe, and Kathryn E. Uhrich are co-authors for this work.]

2.1 Introduction

Cardiovascular disease is the leading global cause of death, claiming approximately 17.3 million lives and costing upwards of $860 billion annually [1]. Innovative methods for prevention and treatment of cardiovascular disease are needed to decrease its prevalence. Many cases begin with atherosclerosis, an inflammatory cascade culminating in calcified plaque accumulation in arterial vasculature [2]. In atherogenesis, monocytes are recruited in response to subendothelial retention of apolipoprotein B and oxidative modification of low density lipoproteins (oxLDL). Macrophages, differentiated from strongly adherent monocytes, become lipid laden foam cells as they internalize oxLDL via two primary scavenger receptors (SRs), SR-A and CD36 [3, 4]. Excessive and unregulated oxLDL internalization ultimately results in macrophage apoptosis, and ineffective clearance of cellular debris initiates plaque formation around a necrotic core [4] (**Figure 2.1**)

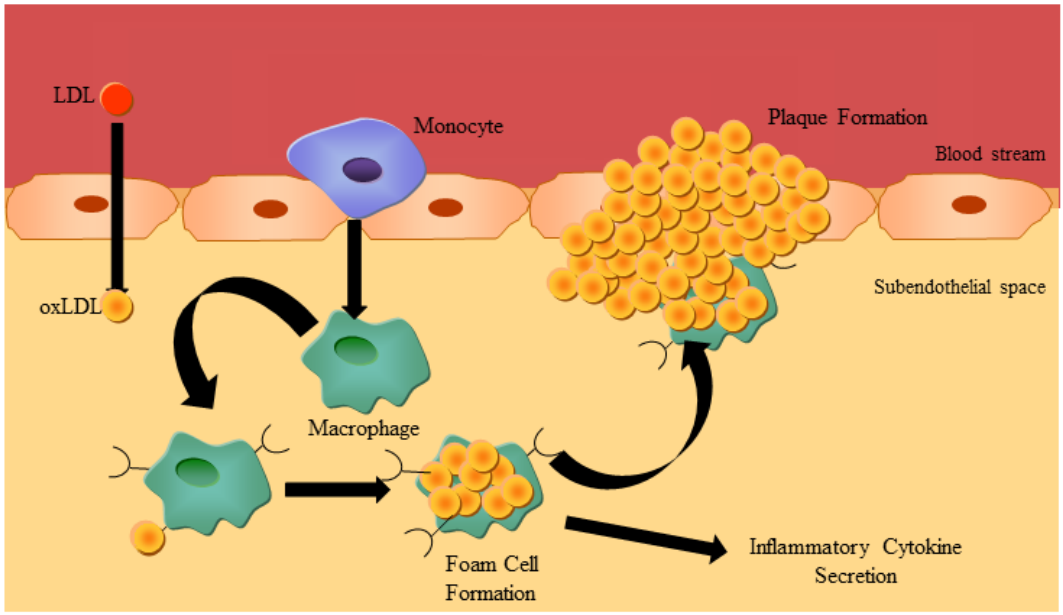

Figure 2.1: Schematic illustration showing atherosclerotic cascade. Monocytes are recruited to the site of injury where they transverse into the subendothelial space and are differentiated into macrophages. Macrophages uncontrollably internalize oxLDL forming foam cells that secrete inflammatory cytokines. Upon excessive oxLDL uptake, foam cells die and form fatty streaks and the necrotic core of arterial plaques. This figure was adapted from previous Rutgers theses [5-7].

Statins, competitive inhibitors of HMG-CoA reductase activity, represent the most commonly prescribed class of cholesterol-lowering pharmaceuticals. Statins function via inhibition of HMG-CoA reductase, the rate-limiting step of cholesterol biosynthesis, and subsequently upregulate LDL receptors [8, 9]. Although they exhibit substantially decreased hepatic and circulating cholesterol levels, systemic administration and off-target effects prove detrimental [10, 11]. HMG-CoA reductase inhibition also affects synthesis of natural products synthesized downstream of cholesterol (e.g., bile acids, sex-steroids), as well as crucial parallel biosynthetic pathways (e.g., coenzyme Q10) [11]. As such, strategically targeted approaches to ameliorate atherosclerosis are needed, including techniques to lower the recruitment of monocytes,

inhibit the deposition and accumulation of circulating LDL and atherogenic lipids at lesion sites, and counteract the athero-inflammatory cascade that leads to lesion growth.

Amphiphilic macromolecules (AMs) designed by the Uhrich group have been shown to attenuate atherosclerotic outcomes [12-17]. AMs are comprised of a linear sugar backbone with fatty acid pendants conjugated to poly(ethylene glycol) (PEG), which self-assemble into nanoscale micelles at low concentrations (~10^{-6} M). These unique compounds can successfully encapsulate and deliver anti-atherosclerotic therapeutics to macrophages, increasing drug bioavailability [14, 18]. Furthermore, the AMs exhibit inherent bioactivity against several cell types (e.g., macrophages and smooth muscle cells) involved in the atherosclerotic cascade when formulated into either micelles or kinetically trapped nanoparticles (NPs) resistant to dissociation upon dilution [19-21]. NPs have demonstrated superiority to micelle formulations as AM NPs lower macrophage oxLDL uptake to ~25% relative to untreated controls, decrease SR expression, and reduce plaque size and aortic occlusion *in vivo* [20, 22, 23]. Despite their promise for treating early stage atherosclerosis, the lead NP formulation consisting of a 1cM shell and M12 core (**Figure 2.2**) fails to ameliorate the inflammatory component of atherosclerosis that can exacerbate the disease state [21]. Thus, new AM designs are necessary to not only counteract atherogenesis, but also mitigate the accompanying inflammatory cascade.

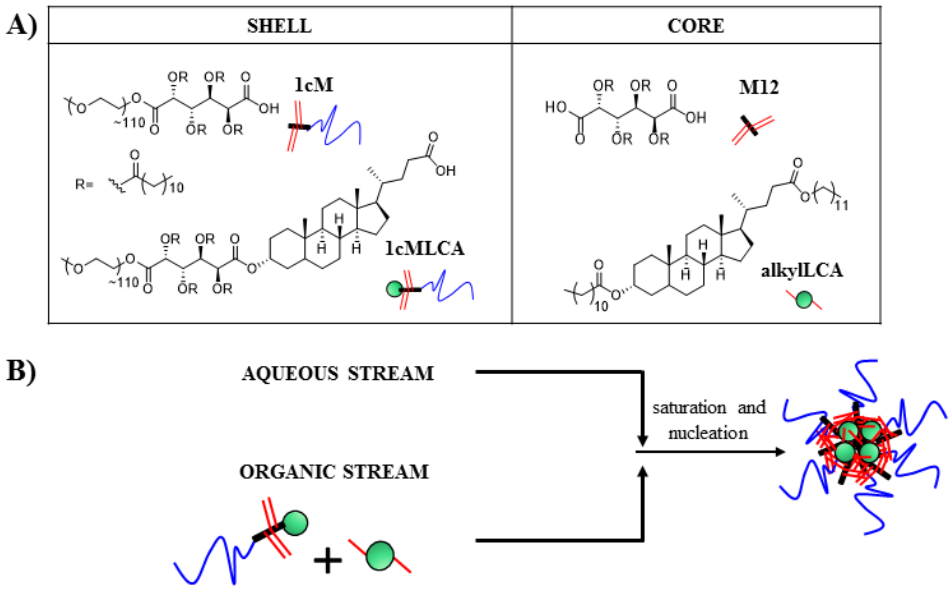

Figure 2.2: Chemical structures and schematics of shell and core molecules incorporated into NPs via FNP. Chemical structures of 1cM and 1cMLCA shells and M12 and alkylLCA cores and corresponding cartoons (A). Schematic representation of the FNP technique utilized to generate AM NPs using 1cMLCA[alkylLCA] as an example (B) where the PEG (blue lines) components extend into aqueous media from the shell and LCA (green circles) is encapsulated within the core of the NP.

Recent approaches to mitigate this effect include using anti-inflammatory molecules such as Vitamin E as the NP core component; however, these NPs exhibit compromised oxLDL uptake inhibition at low administration concentrations, and this strategy does not target the intrinsic inflammatory responses accompanying oxidized lipid uptake [21]. An alternate preventative approach is to target inherent biological pathways that combat the inflammatory response induced by both the NPs and the atherosclerotic cascade. The G-protein coupled bile acid receptor 1 (GPBAR-1, also known as TGR5) is an emerging target in mediating pro-inflammatory interleukins, and its activation reportedly reduces monocyte adhesion in endothelial cells, stabilizes the alternative M2 phenotype, and inhibits lesion formation *in vivo* [24-27]. TGR5 is activated by

the naturally occurring bile acid lithocholic acid (LCA) at 0.53 μM, suppressing lipopolysaccharide (LPS)-stimulated cytokine production [28]. Hence, conjugation of LCA to AMs could decrease the inherent inflammation associated with AM NP administration and provide benefits of activating a target implicated in anti-atherogenic outcomes both *in vitro* and *in vivo.*

The synthesis of LCA-conjugated NP components is reported herein and their bioactivity in human macrophages *in vitro* is described. LCA-conjugated constructs were strategically designed to cleave via native esterases and act as depos that release LCA to interact with TGR5 without compromising the anti-atherogenic effects of the AM NPs. NP formulations with unique core/shell combinations were evaluated for the components' influence on NP physicochemical properties, as well as the ability to inhibit oxLDL uptake and lower macrophage inflammation.

2.2. Results and Discussion

2.2.1. LCA-Conjugates Successfully Synthesized via Multi-step Reactions

LCA-conjugates were synthesized to evaluate the effect of incorporating a naturally occurring TGR5 ligand into AM NP formulations to address atherosclerotic inflammation and mitigate the proinflammatory effects observed with AM NP administration. Both an LCA-conjugated AM and a hydrophobically modified LCA-conjugate were synthesized to enable the fabrication of NPs with high LCA incorporation in the shell and core respectively.

LCA-conjugates were strategically designed to retain oxLDL uptake reduction properties, while bearing the active LCA functionality. It was previously observed that AMs with a net negative charge resulted in statistically significant reductions in oxLDL uptake compared to neutral or cationic analogs [12]. The 1cMLCA-conjugate was designed such that LCA would be at the terminal end to freely interact with TGR5 and bear a net negative charge to mimic the physicochemical properties of oxLDL for effective SR competitive inhibition and cellular uptake [29]. The carboxylic acid of LCA (**1**) was initially protected by reaction with benzyl bromide in

the presence of a mild base as shown in **Figure 2.3**. By doing so, it was assured that the lead AM from previous studies (**1cM**) would be conjugated through the hydroxyl group of **2** via subsequent carbodiimide coupling, yielding the protected 1cMLCA-conjugate (**3**). The benzyl protecting group was then removed via hydrogenolysis with 10% w/w Pd/C to yield the final 1cMLCA-conjugate (**4**).

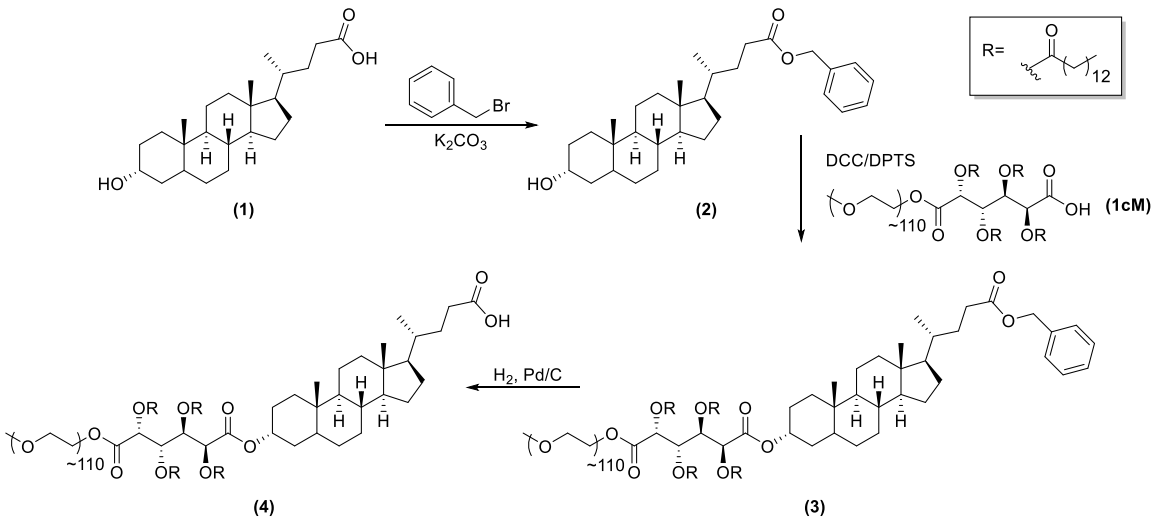

Figure 2.3: Synthetic scheme showing synthesis of 1cMLCA (**4**) from LCA (**1**) and 1cM starting materials.

A hydrophobic analog of LCA was also synthesized according to **Figure 2.4** to enable fabrication of NPs via FNP. This method combines an amphiphile (e.g., 1cMLCA) and hydrophobe (e.g., alkylLCA) in a water-miscible organic solvent prior to fabrication. The organic solution is rapidly mixed with an aqueous buffer, resulting in hydrophobe precipitation and the amphiphile assembly around the precipitates, generating NPs with a specific core/shell architecture (**Figure 2.2B**) [30, 31]. Although LCA has low aqueous solubility and is capable of forming NPs with AMs, the resulting NP stability is not sufficient, resulting in rapid NP aggregation (*data not shown*). Ansell et al. has previously demonstrated that increasing the hydrophobicity of partially water-soluble drugs via lipophilic anchor conjugation improves NP formation, extending the half-life,

and thus, bioactivity [32]. To enable efficient encapsulation of LCA and improve NP stability, the lipophilicity of LCA was increased by first acylating the hydroxyl of **2** in the presence of zinc (II) chloride to yield **5**. Following benzyl deprotection via hydrogenolysis, the free carboxylic acid was alkylated via carbodiimide coupling to yield the LCA-based hydrophobe, alkylLCA (**7**) in high purity.

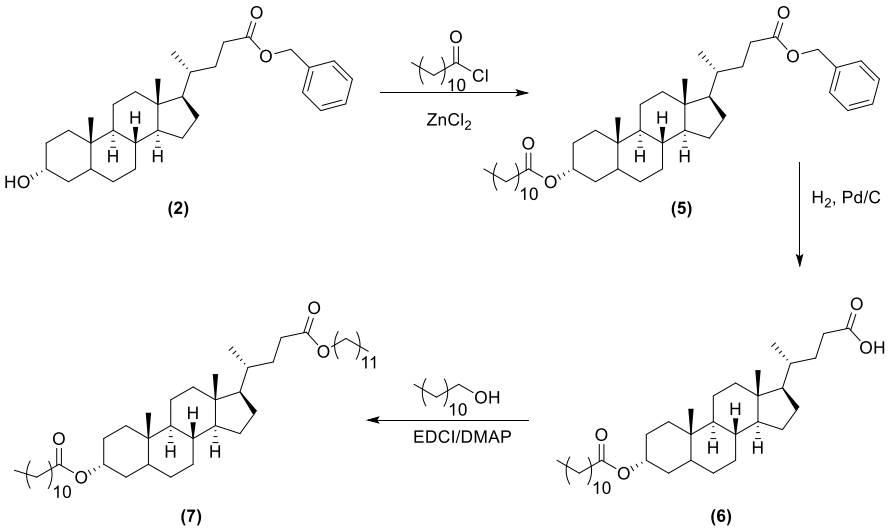

Figure 2.4: Synthetic scheme showing synthesis of alkylLCA (**7**) from benzylLCA (**2**) starting material

All small molecules were characterized via ^{1}H-NMR, ^{13}C-NMR, and FT-IR, and ESI-MS techniques, while PEGylated products were characterized via ^{1}H-NMR and GPC techniques. Several techniques, including ^{1}H-NMR and FT-IR spectroscopies were critical to elucidate the final structures of LCA-conjugates and precursors. **Figure 2.5** presents the sequential ^{1}H-NMR spectra leading to the synthesis of 1cMLCA. Successful benzyl protection of LCA's acid functionality was confirmed via the absence of the acid carbonyl and the appearance of an ester stretch at 1736.33 cm^{-1} in the FT-IR spectrum. Additionally, benzylic and aromatic protons at 5.10 ppm and 7.35 ppm, respectively, in the ^{1}H-NMR spectrum were indicative of successful protection (e and f in **Figure 2.5**). Conjugation of **2** to 1cM to generate **3** was evidenced by the relative integration of

peaks from **2** and those previously established to be characteristic of 1cM, as well as the downfield chemical shift of the C3 hydrogen from 3.61 ppm to 4.72 ppm (a in **Figure 2.5**). Generation of the final 1cMLCA conjugate (**4**) was confirmed via the disappearance of aromatic and benzylic protons in the ^{1}H-NMR spectra.

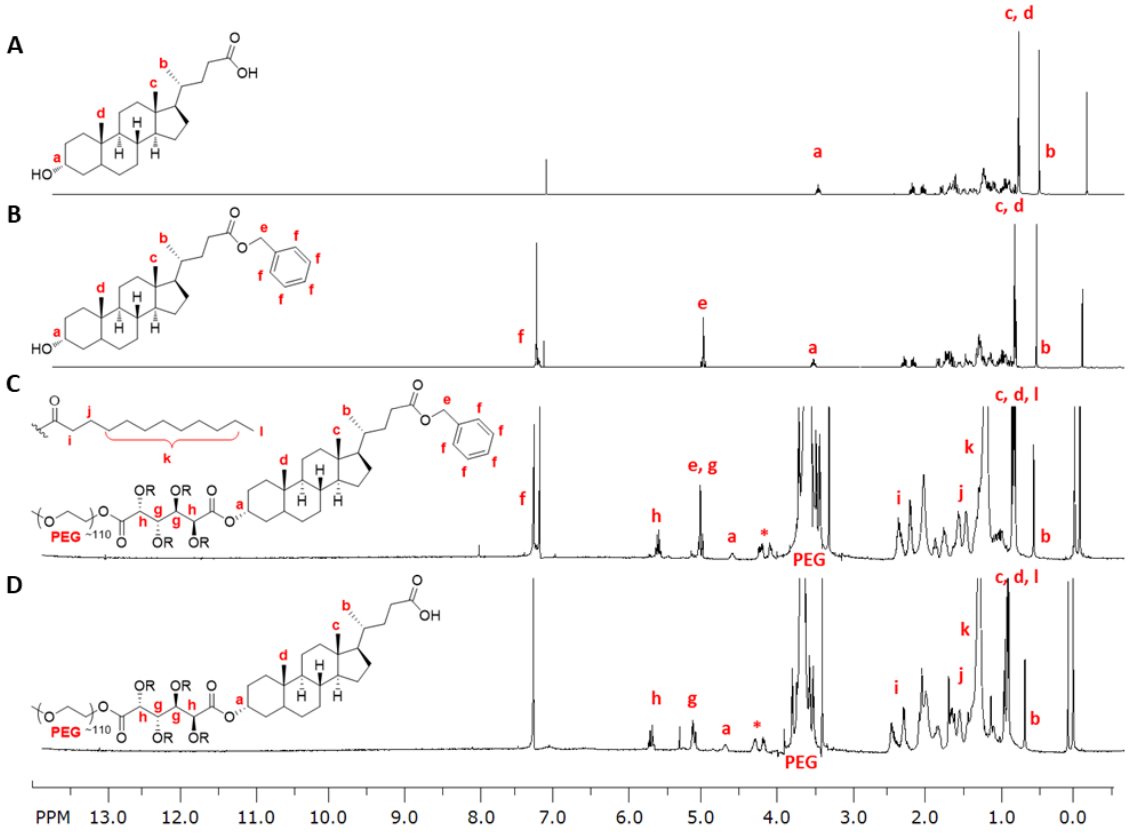

Figure 2.5: Sequential ^{1}H-NMR spectra in the synthesis of 1cMLCA. (A) LCA, (B) benzyl lithocholate, (C) 1cM benzyl lithocholate, (D) 1cMLCA. (*) represents methylene group in PEG adjacent to the ester.

Techniques including ^{1}H-NMR, FT-IR, and ESI-MS techniques were also crucial in confirming successful generation of alkylLCA (**7**). A downfield shift of the C3 hydrogen from 3.61 ppm to 4.72 ppm and disappearance of the broad -OH stretching vibration in the FT-IR spectrum confirmed hydroxyl group acylation. Benzyl deprotection was evidenced by the disappearance of benzylic and aromatic protons (e and f in **Figure 2.6**) as previously described, as

well as a parent peak in the ESI-MS at *m/z*= 557.7 $[M-1]^-$. Subsequent alkylation of the carboxylic acid was confirmed via the appearance of a triplet representing the methylene adjacent to the ester at 4.04 ppm (k in **Figure 2.6**) and disappearance of the acid carbonyl in the FT-IR spectra at 1703.15 cm^{-1}.

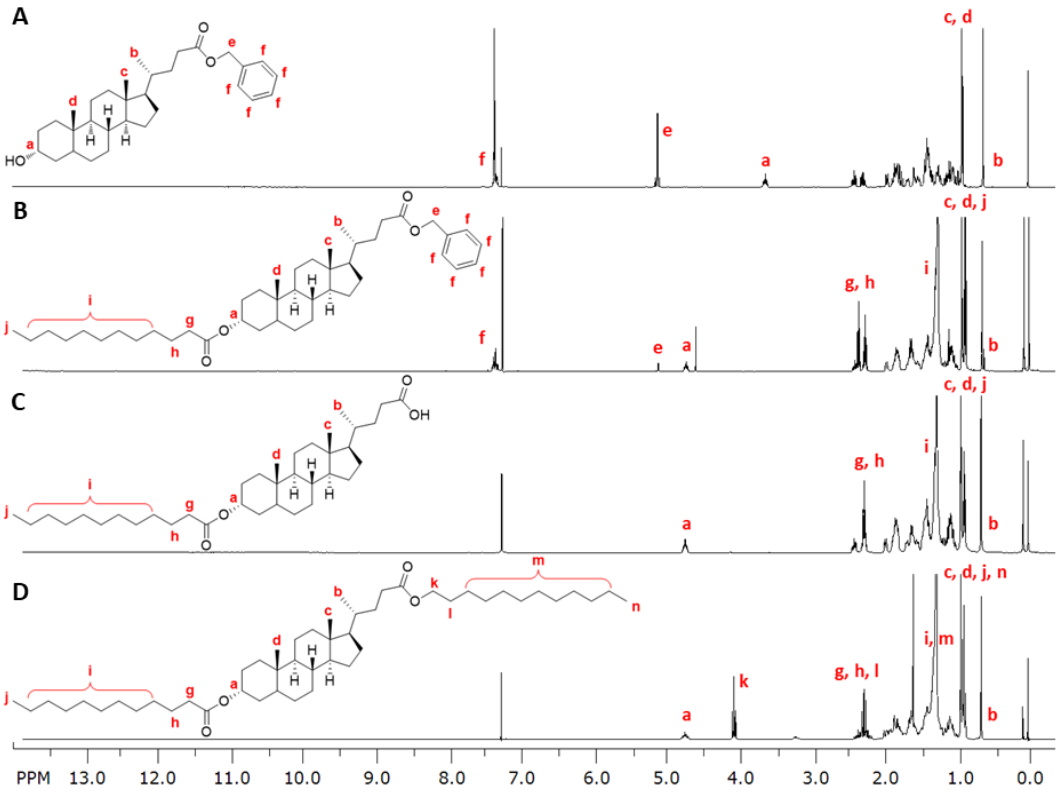

Figure 2.6: Sequential ^{1}H-NMR spectra in the synthesis of LCA-based hydrophobe. (A) benzyl lithocholate, (B) alkylated benzyl lithocholate, (C) monoalkylated LCA, (D) alkylated lithocholate.

2.2.2 Stable Mono-dispersed Nanoparticles Fabricated with LCA-Conjugates Possess Negative Charge and Desirable Size Distributions

Although previous AM micellar preparations were shown to have bioactivity at high concentrations, improved inhibition of oxLDL uptake was observed with AM NPs in serum-containing medium compared to micelles [19, 20]. NPs fabricated using FNP are different from micelles in that the core molecule serves as a nucleation point to fabricate kinetically trapped

particles that do not dissociate upon dissolution. [20] In the present study, novel AM NPs were generated via FNP, including 1cMLCA and alkylLCA as the shell and core components, respectively. Additional NP formulations with combinations of shell and core materials were also prepared to evaluate the potential impact of each component on physicochemical properties and biological outcomes. The previously demonstrated highly efficacious core (i.e., M12) and shell (i.e., 1cM) material were included in the evaluation for comparison (**Figure 2.2A**).

The physicochemical properties of NP formulations are shown in **Table 2.1.** The data demonstrates that shell composition influences particle size, while core chemistry does not have a significant influence on any physical attributes. NPs prepared with 1cM shells were found to have statistically indistinct hydrodynamic diameters, regardless of core identity. Likewise, NPs with 1cMLCA shells have similar sizes, independent of the core material. However, NPs prepared with 1cM shells have hydrodynamic diameters that are statistically larger than NPs made with 1cMLCA shells ($p \leq 0.05$). The discrepancy may be that NP sizes are attributed to the FNP process. This observation suggests that the core materials have similar rates of precipitation when the molecules contact the aqueous stream during FNP. However, the aggregation and packing behavior of the shell material around the precipitated cores appears to differ due to the addition of the LCA moiety. It is likely that the increased hydrophobicity of LCA increases the packing density of AMs around the core, therefore, leading to the decreased hydrodynamic diameters of NPs with 1cMLCA shells.

Table 2.1: Physicochemical properties of AM NPs indicating particle size, polydispersity index (PDI) and ζ potential determined by dynamic light scattering measurements. Formulation notation is denoted as Shell[Core].

Formulation	Hydrodynamic Diameter (nm)	PDI	ζ Potential (mV)
1cM[M12]	213 ± 4	0.11	-30
1cM[alkylLCA]	206 ± 16	0.09	-31
1cMLCA[M12]	176 ± 14	0.16	-33
1cMLCA[alkylLCA]	173 ± 2	0.11	-31

NPs with 1cM shells have particle sizes above 200 nm, which is the generally accepted upper limit for cellular uptake via endocytosis [33]. Interestingly, NPs with 1cMLCA shells have sizes below this threshold, making them more amenable to cellular internalization via endocytotic mechanisms. Previous data demonstrated a direct correlation between AM NP internalization by cells and an increase in oxLDL uptake inhibition efficacy [20, 23]. Further, all NPs have comparable negative ζ potentials, an attribute which appears crucial to NP efficacy. This result correlates with previous data, as NPs with a negative ζ potential are hypothesized to allow AM NPs to mimic oxLDL, resulting in competitive inhibition of oxLDL uptake via SRs [13, 29]. Notably, the addition of LCA does not significantly impact the ζ potential, a feature that was critical in the molecular design. Further, all NPs have low PDIs, indicating uniform NP size with no evidence of NP aggregation. This property is an asset to oxLDL uptake competitive inhibition and storage stability.

2.2.3 AM NPs Inhibit oxLDL Uptake in Human Macrophages

To measure oxLDL uptake inhibition, hMDMs were simultaneously treated with AM NPs and oxLDL or oxLDL alone (control), and internalization was quantified via flow cytometry and visualized via confocal microscopy (**Figure 2.7**). Cells were treated at $1x10^{-5}$ M concentration of the AMs, as the Uhrich group have previously demonstrated *in vitro* and *in vivo* cytocompatibility and high bioactivity at this concentration [20, 22]. Under all AM NP treatments, oxLDL uptake was reduced to < 30% of controls (**Figure 2.7B**). These data demonstrate that both shell materials are highly efficacious at reducing oxLDL internalization, including NPs with LCA-conjugation. This observation supports the hypothesis that the NPs mimic oxLDL, and thus competitively inhibit SRs, despite LCA conjugation, and they retain potent oxLDL uptake inhibition properties. The NPs with LCA's free carboxylate retain a negative ζ potential and have sizes amenable to endocytosis, which would give rise to potent oxLDL competitive inhibition. These observations are in agreement with previous findings for other formulations, in which NPs with net negative ζ

potentials close to zero exhibited poor oxLDL uptake reduction compared to NPs with higher magnitudes of negative ζ potential [23]. Therefore, with the criteria of a negative NP ζ potential and NP sizes below 200 nm, it is plausible that an array of naturally active ligands conjugated to 1cM would elicit desired biological effects.

While all shells were found to be active, these data further illustrate that shell chemistries based on the 1cM structure do not adversely influence the magnitude of oxLDL uptake inhibition (**Figure 2.7C**). Both the 1cM and 1cMLCA shells exhibit comparable degrees of oxLDL uptake inhibition. Interestingly, the NP core material influences the degree of oxLDL uptake, with alkylLCA cores exhibiting significantly more oxLDL uptake inhibition than M12 cores (**Figure 2.7C**). The stronger influence of the core material on the NP anti-atherogenic potential is consistent with previously reported data using mixed PS and M12 cores [23]. As such, it was hypothesized that oxLDL uptake is not only reduced via competitive interactions with SRs. Rather, it is likely that surface molecules from the NPs' shells exist in an equilibrium with the unimeric components. This equilibrium may be mediated by extracellular serum disruption or intracellular mechanisms, which lead to interactions between the core materials and biological targets. For example, 1cMLCA[alkylLCA] NPs may partly dissociate to free their respective amphiphilic unimers, thereby freeing them to interact with cellular receptors, such as TGR5, to elicit an enhanced reduction in oxLDL uptake (**Figure 2.7A**). Previous work has demonstrated the biodegradation of AM ester functionalities by serum esterases, which presumably leads to high local concentrations of free LCA [34]. The high local concentration of LCA is hypothesized to be partially responsible for increased oxLDL reduction for NPs with alkyl LCA cores, as TGR5 activation has a demonstrated effect on reducing oxLDL uptake [24].

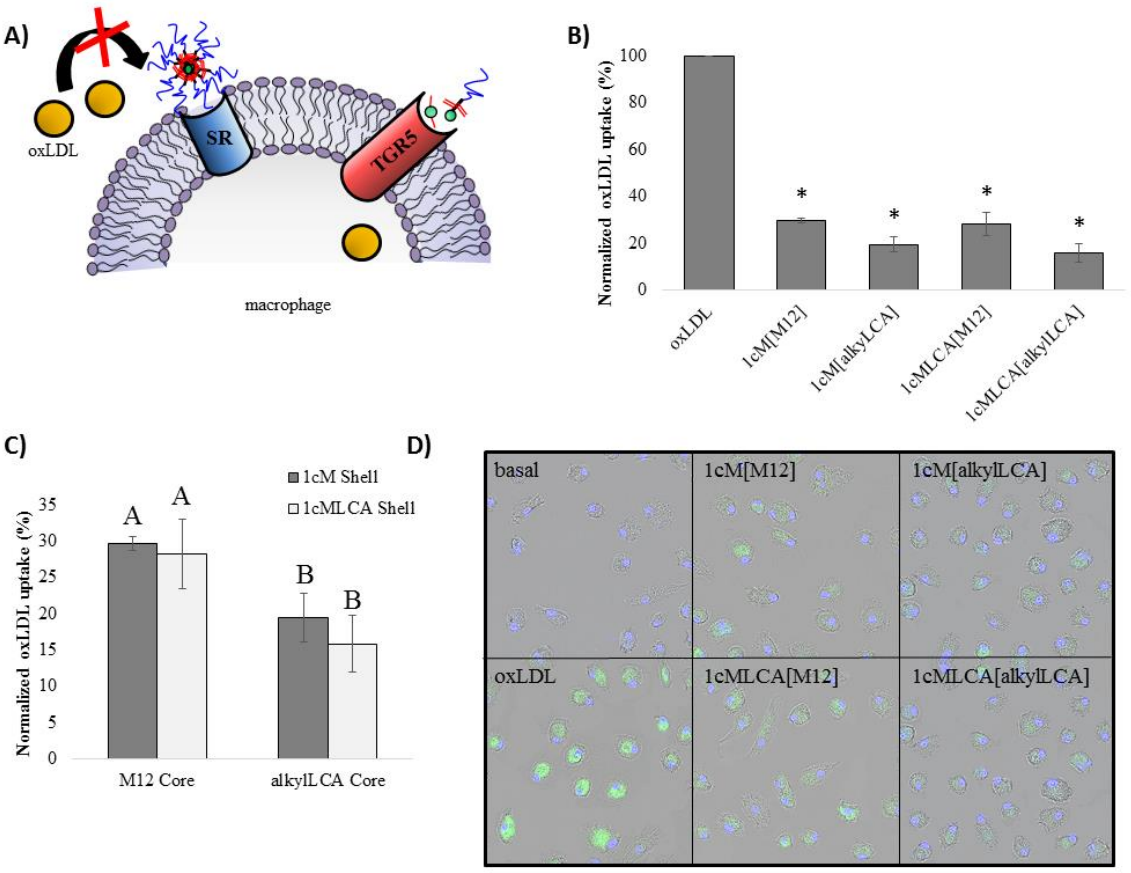

Figure 2.7: AM NPs reduce oxLDL uptake in macrophages (schematic, A). All NPs reduce oxLDL uptake in hMDMs compared to basal controls as measured via flow cytometry (B). Core chemistry has a significant impact on oxLDL uptake inhibition levels, but shell chemistry does not significantly alter efficacy (C). Respective confocal microscopy images (D) 24 h after treatment with AM NPs indicate cell morphology, cell nuclei (blue), and DiO labeled oxLDL (green) 40X magnification.

2.2.4 AM NP Composition Markedly Impacts Inflammatory Gene Transcription

As LCA-conjugation does not adversely affect oxLDL uptake inhibition activity, gene expression was used to evaluate the LCA-based NPs potential to decrease inflammation in macrophages. LCA-conjugates were strategically designed to interact with membrane bound

receptors, including TGR5, to mitigate the inflammatory response due to the atherosclerotic cascade, as well as from NP administration. TGR5 is a transmembrane protein expressed in macrophages that has a demonstrated role in the reduction of several inflammatory cytokines in the atherosclerotic cascade. Of interest, a decrease in the transcription and expression of IL-1β, IL-6, and IL-8 have been demonstrated upon treatment with bile acids or synthetic TGR5 agonists [28, 35, 36]. These genes are also upregulated in human macrophages following treatment with 1cM[M12] NPs, which limits this NP formulation's clinical applicability [21]. As such, qRT-PCR was utilized to evaluate the potential influence of NP composition on the inflammatory cytokine profile in human macrophages, including those genes known to mitigate and exacerbate the disease state.

The co-treatment of macrophages with AM NPs and oxLDL resulted in a significant impact on mRNA levels of inflammatory cytokines mediated by TGR5 and SRs involved in oxLDL uptake (**Figure 2.8**). Findings are consistent with previous studies, indicating that NPs containing an M12 core significantly upregulate mRNA expression of the pro-atherogenic cytokine IL-1β [21]. IL-1β is a pro-inflammatory cytokine secreted by activated monocytes and macrophages and is implicated in both the early and late stages of atherosclerosis [37, 38]. In the early stages of atherosclerosis, IL-1β increases adhesion molecule expression in endothelial cell membranes, while in later stages, it facilitates fibrous cap destabilization at plaque sites *in vivo*, ultimately leading to plaque rupture [37, 38]. As such, the increase in IL-1β transcription induced by 1cM[M12] NPs is undesirable, and treatment with these NPs would exacerbate atherogenesis. In this work, the increase in IL-1β observed after 1cM-based NP treatment was significantly lower with alkylLCA incorporation into the NPs cores as compared to those with M12 cores (**Figure 2.8B**). This effect was also observed for NPs with 1cMLCA shells. These data demonstrate that core modification can mitigate the limitations of previous AM NP formulations. It was hypothesized that LCA-incorporation in the shell would further decrease IL-1β due to TGR5 activation. Interestingly, it was observed that the

attenuation of IL-1β transcription with 1cMLCA shells was not as prominent, suggesting that inflammation resulting from NP treatment is multifactorial, and more largely influence by the hydrophobe component of NPs. As 1cMLCA-based NPs exhibit a minimal response to core identity, it is possible the overall NP hydrophobicity also contributes to IL-1β response.

1cM[M12] also results in upregulation of the pro-atherogenic cytokines IL-6 and IL-8 in macrophages, limiting its further development as a comprehensive therapeutic against atheroinflammation [21]. IL-6 has been implicated in recruitment of activated monocytes and their subsequent differentiation into macrophages, and an increase in IL-8 upregulates endothelial expression of adhesive molecules that promote activated monocyte/macrophage attachment [38]. Both of these steps occur in the early stages of atherosclerosis, and preventing or reducing their occurrence is crucial to halting the cascade's initiation and perpetuation. As such, the reduction in the secretion of these cytokines is needed to increase the therapeutic potential of AM NPs. Expression of IL-6 and IL-8 upon AM NP treatment reveal similar trends to those observed for IL-1β, with a decrease in transcription when treated with 1cM-based NP formulations with alkylLCA cores. Interestingly, no notable trend is observed for expression of IL-6 or IL-8 in macrophages treated with 1cMLCA NPs, further supporting the hypothesis that the level of overall AM NP hydrophobicity is critical in mitigating the inflammatory response in macrophages treated with NPs.

Additional inflammatory cytokines were evaluated including IL-10 and TNFα, as well as two SRs responsible for oxLDL internalization, CD36 and SRA. In all cases, NP formulations had minimal influences on these genes' mRNA expression. These data suggest that the AM NPs' molecular mechanism leading to inflammation reduction may occur via protein turnover rather than mRNA control of protein expression, or alternative mechanisms. Nonetheless, 1cM[alkylLCA] was identified as a lead NP formulation, as it demonstrates a large reduction in several

inflammatory cytokines, namely IL-1β, IL-6, and IL-8, induced via atherosclerosis and administration of previous AM NP formulations.

A)

	Inflammatory Cytokines					SRs	
	IL-1β	IL-6	IL-8	IL-10	TNFα	CD36	SRA1
basal	1	1	1	1	1	1	1
1cM[M12]	271	89	85	-2	3	-3	-2
1cM[alkylLCA]	41	39	43	-2	4	-3	-2
1cMLCA[M12]	232	63	58	-2	2	-3	-3
1cMLCA[alkylLCA]	153	51	95	-3	5	-3	-3

B)

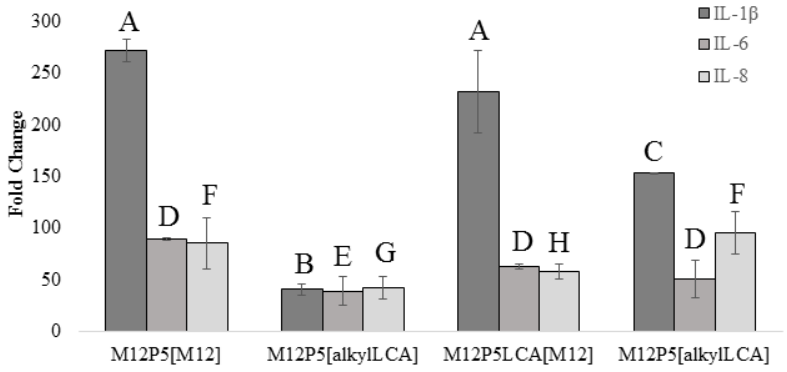

Figure 2.8: Fold change in mRNA levels of inflammatory cytokines and SRs in hMDMs as determined via rt-PCR 24 h after treatment with AM NPs (A). An increase or decrease in gene transcription are highlighted in green and red respectively. Transcription levels of three cytokines significantly affected by NP treatment (B). Different letters indicate statistical significance, whereas identical letters indicate no statistical difference.

2.3. Conclusion

LCA was modified and effectively incorporated into NPs to establish a new generation of NPs for the treatment of inflammation in atherosclerosis. The NPs were comprised of an LCA-containing shell, where the bile acid was conjugated to AMs previously shown to reduce oxLDL uptake in human macrophages, and an LCA-containing core, where LCA was hydrophobically modified to serve as a NP nucleation point. The appropriate size for cellular uptake and net negative

charge allow the NPs to mimic oxLDL and inhibit its uptake via competition with oxLDL in SR binding sites.

NPs with alkylLCA cores lowered the atherogenic potential of macrophages by significantly decreasing oxLDL uptake compared to NPs with M12 cores. However, shell identity did not have an impact on oxLDL uptake inhibition, indicating that the core is the active component. It is likely that AM NPs exist in equilibrium with monomeric components, and serum proteases partly degrade the hydrophobic cores. This equilibrium would result in interactions between the natural ligand, LCA, with TGR5, resulting in receptor activation and a decrease in oxLDL uptake. Both the core and shell components did, however, impact the gene transcription profile in macrophages treated with AM NPs. Treatment with 1cM[alkylLCA] NPs resulted in the lowest expression levels of inflammatory cytokines in macrophages treated with AM NPs to date.

Together, this information illustrates that modifying AM NP composition has a drastic impact on the inflammatory profile of human macrophage populations. The inflammatory cytokines evaluated in this study that were downregulated in the presence of the 1cM[alkylLCA] are, in part, regulated by TGR5 activation. It is therefore likely that this NP formulation activates TGR5, leading to a decrease in inflammation. As the overall hydrophobicity was observed to influence the inflammatory response, this formulation also appears to have the optimal balance of hydrophobicity imparted by alkyl chains and LCA moieties to not exacerbate inflammation while simultaneously reducing inflammatory cytokine expression involved in atherosclerosis.

These findings illustrate that a ligand can be successfully modified and delivered to macrophages to elicit a desired biological outcome without compromising the beneficial properties of previous AM NPs. As both a reduction in oxLDL uptake and inflammation are critical to reduce macrophage atherogenic potential, the results of these experiments demonstrate improvement upon previous AM generations with respect to inflammatory cytokine expression and provide insight to develop future AM NPs that exhibit desirable outcomes by influencing biological targets.

2.4. Experimental

2.4.1 Materials

All reagents and materials were purchased from Sigma-Aldrich (Milwaukee, WI) and were used as received unless noted otherwise. Hydrochloric acid (HCl, 1N) was purchased from Fisher Scientific (Fair Lawn, NJ), and silica from VWR (Radnor, PA). The confined impinging jet mixer was provided by Prof. Robert Prud'homme at Princeton University (Princeton, NJ). Cell culture assays used human buffy coats purchased from the New York Blood Center (New York, NY) or New Jersey Blood Center (East Orange, NJ), Ficoll-Paque premium 1.077 g/mL and Percoll 1.3 g/mL from GE Healthcare (Fairfield, CT), FEP Teflon cell culture bags from Cellgenix, RPMI-1640 from ATCC (Manassas, VA), macrophage colony stimulating factor (MCSF) from PeproTech (Rocky Hill, NJ), penicillin/streptomycin from Lonza (Basel, Switzerland), fetal bovine serum (FBS) from Life Technologies (Carlsbad, CA), human serum from MP Biomedical, unlabeled oxLDL from Biomedical Technologies Inc. (Ward Hill, MA), and 3,3'-dioctadecyloxacarbocyanine (DiO) labeled oxLDL from Kalen Biomedical (Montgomery Village, MD).

2.4.2 Characterization

Proton (^{1}H) and carbon (^{13}C) nuclear magnetic resonance (NMR) spectra were obtained from a Varian 400 MHz or 500 MHz spectrometer. Reaction products were dissolved in deuterated chloroform ($CDCl_3$) with trimethylsilane (TMS) as an internal reference. Fourier transform infrared (FT-IR) spectra were obtained by solvent-casting small molecules onto sodium chloride (NaCl) plates in dichloromethane (DCM) then recorded using a Thermo Scientific Nicolet iS10 spectrophotometer with an average of 32 scans per sample and processed using OMNIC software. Small molecule molecular weights were established using a ThermoQuest Finnigan (LCQ-DUO system equipped with a syringe pump, optional divert/inject valve, atmospheric pressure ionization

(API) source, and mass spectrometer (MS) detector) and spectra were processed using the Xcalibur data system. Compounds (10 µg/mL) were dissolved in methanol (MeOH) or DCM with 1% acetic acid or ammonia for positive or negative ion detection, respectively. Weight-averaged molecular weights (Mw) and polydispersity indices (PDI) of AMs were determined by gel permeation chromatography (GPC) using a Waters liquid chromatography (LC) system (Milford, MA), equipped with a 2414 refractive index detector, 1515 isocratic HPLC pump, 717plus autosampler, and Jordi divinylbenzene mixed-bed GPC column (7.8 x 300mm, Alltech Associates, Deerfield, IL). Samples (10 mg/mL) were prepared in DCM and filtered through a 0.45 µm polytetrafluoroethylene (PTFE) syringe filter prior to autoinjection. The eluent (DCM) was set at a flow rate of 1 mL/min, and IBM ThinkCentre computer with WaterBreeze version 3.20 software used to process data against a calibration curve generated with broad-range PEG standards (Waters Milford, MA).

2.4.3 Synthesis

Synthesis of 1cMLCA (**4**). According to a modified literature procedure, the carboxylic acid of LCA was selectively protected [39]. LCA (**1**, 1.0 eq.) was dissolved in 10 mL of anhydrous dimethylformamide (DMF) under nitrogen. Potassium carbonate (1.2 eq.) was added and the suspension allowed to stir for 30 min. Benzyl bromide (1.5 eq.) was then added and the reaction stirred for 12 h at room temperature. The reaction was diluted with diethyl ether (20 mL) and washed with sodium bicarbonate (3X, 15 mL). The crude product was dried over magnesium sulfate ($MgSO_4$), filtered, and concentrated *in vacuo*. **2** was then purified on silica gel via flash chromatography using a hexanes/ethyl acetate gradient (95:5 to 80:20).

1cM, synthesized as previously described [40], was dried by azeotropic distillation with toluene under reduced pressure 3X prior to use. 1cM (1.0 eq.) was then dissolved in 10 mL of DCM under nitrogen with **2** (2.0 eq.) and 4-(dimethylamino)pyridinium-4-toluene sulfonate (DPTS, 1.0 eq.) under nitrogen, followed by dropwise addition of N,N'-dicyclohexylcarbodiimide

(DCC, 1M, 2.0 eq.) as a coupling reagent. After 24 h, the reaction was cooled to 0 °C and the urea byproduct removed via filtration. The filtrate was washed 2X with 1N HCl and 1X with brine, followed by removal of solvent *in vacuo*. The product was precipitated in diethyl ether (50 mL), collected via centrifugation (3500 rpm, 5 min each) and washed a total of 5X to obtain **3**.

The benzyl group was removed via hydrogenolysis with palladium on carbon (Pd/C, 10% w/w) as the catalyst for 24 h in DCM (10 mL). The heterogeneous mixture was then filtered through Celite to remove Pd/C and the filtrate removed *in vacuo* to obtain **4**.

Benzyl lithocholate (**2**): Yield: 76% (white solid). ^{1}H-NMR (500 MHz, $CDCl_3$): δ 0.61 (s, 3H), 0.91 (s, 6H), 0.94-1.93 (br. m, 27H), 2.26 (m, 1H), 2.39 (m, 1H), 3.61 (m, 1H), 5.10 (s, 2H), 7.35 (m, 5H). ^{13}C-NMR (500 MHz, $CDCl_3$): δ 12.01, 18.23, 20.80, 23.36, 24.19, 26.40, 27.18, 28.16, 30.54, 30.96, 31.27, 34.56, 35.30, 35.34, 35.83, 36.45, 40.15, 40.41, 42.08, 42.71, 55.94, 56.47, 66.07, 71.85, 128.15, 128.21, 128.53, 136.12, 174.11. IR (cm^{-1}, thin film from chloroform $CHCl_3$): 3334.36 (OH, alcohol), 1736.88 (C=O, ester). ESI-MS m/z: 505.5 $[M+39]^{+}$.

1cM benzyl lithocholate (**3**): Yield: 78% (white solid) ^{1}H-NMR (500MHz, $CDCl_3$): δ 0.64 (s, 3H), 0.87 (m, 18H), 0.94-1.99 (br. m. 99H), 2.27 (m, 4H), δ 2.41 (m, 4H), 3.63 (m, ~425H), 4.27 (m, 2H), 4.30 (m, 2H), 4.72 (m, 1H), 5.18 (m, 4H), 5.70 (m, 2H), 7.35 (m, 5H). Mw= 5.6, PDI= 1.2.

1cMLCA (**4**): Yield: 81% (white solid) ^{1}H-NMR (500MHz, $CDCl_3$): δ 0.64 (s, 3H), 0.87 (m, 21H), 0.94-1.99 (br. m. 99H), 2.27 (m, 4H), 2.41 (m, 4H), 3.63 (m, ~425H), 4.27 (m, 2H), 4.30 (m, 2H), 4.72 (m, 1H), 5.18 (m, 2H), 5.70 (m, 2H). Mw= 5.6, PDI= 1.2.

Synthesis of LCA-based hydrophobe (**7**). **2** (1.0 eq.) and zinc chloride ($ZnCl_2$, 0.5 eq.) were dissolved in 10 mL of DCM under N_2, followed by addition of lauroyl chloride (3.0 eq.), then heated to reflux overnight with stirring. The crude product was then purified using silica gel via flash chromatography with hexanes/ethyl acetate (90:10) to yield **5**.

The benzyl protecting group was removed via hydrogenolysis as previously described, and the carboxylic acid of **6** was conjugated to dodecanol via carbodiimide coupling. Dodecanol (2.0 eq.) and dimethylaminopyridine (DMAP, 2.0 eq.) were completely dissolved in 10 mL anhydrous DCM under nitrogen. The coupling reagent 1-ethyl-3-(3-(dimethylamino)propyl) carbodiimide (EDCI, 2.5 eq.) was added and the reaction stirred overnight. The mixture was washed with 10 % potassium bisulfite (2X, 15 mL) and brine (1X, 15 mL) to remove the urea byproduct and DMAP. The crude product was purified on silica gel via flash chromatography with hexanes/ethyl acetate (80:20). The organic layer was then dried over $MgSO_4$, filtered, and concentrated *in vacuo* to obtain **7**.

Alkylated benzyl lithocholate (**5**)*:* Yield: 73% (white solid). ^{1}H-NMR (500 MHz, $CDCl_3$): δ 0.61 (s, 3H), 0.88 (t, 3H), 0.91(s, 6H), 0.94-1.93 (br. m, 44H), 2.26 (m, 3H), 2.39 (m, 1H), 4.72 (m, 1H), 5.10 (s, 2H), 7.35 (m, 5H). ^{13}C-NMR (500 MHz, $CDCl_3$): δ 12.01, 14.10, 18.24, 20.82, 22.67, 23.32, 24.16, 25.09, 26.32, 26.69, 27.02, 28.16, 29.12, 29.24, 29.32, 29.45, 29.59, 30.97, 31.28, 31.90, 32.27, 34.59, 34.78, 35.04, 35.31, 35.78, 40.12, 40.39, 41.90, 42.72, 56.00, 56.46, 66.07, 74.05, 128.15, 128.21, 128.52, 136.12, 173.43, 174.08. IR (cm^{-1}, thin film from chloroform $CHCl_3$): 1735.05 (C=O, ester).

Mono-alkylated lithocholic acid (**6**): Yield: quantitative (white solid) ^{1}H-NMR (500MHz, $CDCl_3$): δ 0.64 (s, 3H), 0.88 (t, 3H), 0.92 (s, 6H), 0.94-1.96 (br. m, 44H), 2.26 (m, 3H), 2.39 (m, 1H), 4.72 (m, 1H). ^{13}C-NMR (500 MHz, $CDCl_3$): δ 12.03, 14.10, 18.23, 20.82, 22.67, 23.32, 24.16, 25.09, 26.31, 26.68, 27.01, 28.16, 29.11, 29.24, 29.32, 29.45, 29.58, 29.59, 30.75, 30.82, 31.90, 32.29, 34.58, 34.78, 35.04, 35.30, 35.78, 40.13, 30.39, 41.89, 42.74, 55.97, 56.47, 74.06, 173.48, 179.36. IR (cm^{-1}, thin film from chloroform $CHCl_3$): 1732.86 (C=O, ester), 1703.15 (C=O, acid). ESI-MS m/z: 557.7 $[M-1]^-$.

Alkylated lithocholate (**7**): Yield: 86% (white solid) ^{1}H-NMR (500MHz, $CDCl_3$): δ 0.64 (s, 3H), 0.87 (t, 3H), 0.92-1.96 (br. m, 71H), 2.30 (m, 6H), 4.04 (t, 2H), 4.77 (m, 1H). ^{13}C-NMR (500

MHz, $CDCl_3$): δ 12.02, 14.10, 18.25, 20.82, 22.67, 23.32, 24.17, 25.09, 25.94, 26.34, 26.68, 27.02, 28.17, 28.65, 29.11, 29.24, 29.32, 29.34, 29.45, 29.52, 29.56, 29.58, 29.59, 29.62, 29.64, 31.05, 31.36, 31.91, 32.29, 34.59, 34.78, 35.04, 35.34, 35.79, 40.13, 40.39, 41.90, 42.73, 56.04, 56.47, 64.42, 74.05, 173.44, 174.42. IR (cm^{-1}, thin film from chloroform $CHCl_3$): 1737.47 (C=O, ester). ESI-MS m/z: 727.5 $[M+1]^+$

2.4.4 Nanoparticle Fabrication

NPs were fabricated via FNP as previously described [20]. Briefly, the AM (40 mg/mL) and hydrophobe (20 mg/mL) were separately dissolved in tetrahydrafuran (THF). A 1:1 v/v mixture of the AM:hydrophobe solution (0.5 mL) was filtered through a 0.2 μm PTFE filter, then rapidly mixed with phosphate buffered saline (PBS, 0.5 mL) in a confined impinging jet mixer, and subsequently added to 4.5 mL of PBS. NP suspensions were dialyzed using a 6-8 kDa ultrafiltration membrane cut-off 3X against sterile PBS (2 L) for organic solvent removal.

2.4.5 Nanoparticle Characterization

NP sizes and zeta (ζ) potential were measured by dynamic light scattering (DLS) using a Malvern-Zetasizer Nano Series (ZS90) in triplicate with a 90° scattering angle. NPs sizes and PDI were evaluated in PBS, and the Z-average was taken as the hydrodynamic diameter. Prior to analyzing ζ potential, NPs were dialyzed extensively against deionized water.

2.4.6 Isolation of Human Monocyte Derived Macrophages (hMDMs)

[Macrophage isolation was performed by Rebecca Chmielowski, Department of Chemical and Biochemical Engineering, Rutgers University, Piscataway, NJ and Qi Li, Department of Biomedical Engineering, Rutgers University, Piscataway, NJ]

Peripheral blood mononuclear cells (PBMCs) were isolated from human buffy coats by centrifugation through Ficoll-Paque (1.077 g/cm^3) density gradient [22]. Red blood cells were lysed with ammonium-chloride-potassium (ACK) buffer and cell debris, including platelets, were removed via centrifugation (300 x g, 10 min). PBMCs were washed with PBS and cultured in

RPMI 1640 supplemented with 10% fetal bovine serum (FBS) and 1% penicillin/streptomycin (complete medium). PBMCs were selected for monocytes as determined by flask adherence after 24 h at 37 °C and 5 % CO_2. Monocytes were cultured for 7 days in complete medium with 50 ng/mL macrophage colony stimulating factor (M-CSF) to differentiate monocytes into macrophages. hMDMs were re-plated, trypsinized, and plated at a density of 150,000 cells/mL and let rest for a minimum of 12 h prior to experimentation.

2.4.7 Oxidized Low-Density Lipoprotein (oxLDL) Uptake in Macrophages

[OxLDL uptake experiments in macrophages were performed by Qi Li, Department of Biomedical Engineering, Rutgers University, Piscataway, NJ]

hMDMs were plated in a 24 well plate at a density of 1.5 x 10^5 cells/mL and incubated with unlabeled oxLDL (4 µg/mL) and DiO labeled oxLDL (1 µg/mL) in the presence of NPs (10^{-5} M) in complete medium for 24 h. Treatments and controls were aspirated and replaced with ice-cold PBS containing 2 mM ethylenediaminetetraacetic acid (EDTA) and samples were placed on ice packs. Cells and EDTA were triturated to remove cells from plates, centrifuged (1000 rpm, 10 min), and fixed in 1% paraformaldehyde (150 µL). oxLDL uptake was quantified by fluorescence on a FACScalibur flow cytometer (Beckton Dickenson, Franklin Lakes, NJ) by collecting a minimum of 10,000 events/sample. Results were analyzed via FlowJo software (Tree Star Inc., Ashland, OR) and reported as the geometric mean fluorescence intensity (MFI). All experiments were performed in triplicate and data is presented as percent (%) oxLDL uptake as normalized to the basal control.

2.4.8 Gene Expression in Macrophages

Gene expression (GAPDH, ACTB, IL-1β, IL-6, IL-8, IL-10, TNFα, CD36, SR-A) in hMDMs was evaluated using quantitative reverse transcription polymerase chain reaction (qRT-PCR). RNA was extracted from hMDMs 24 h after co-treatment using an RNeasy Plus Mini Kit with Quiashredder columns according to supplier protocol. The concentration and purity of RNA

was quantified using a Nanodrop 2000c. RNA was reverse transcribed to cDNA using a High Capacity cDNA Kit and RapidCycler thermal cycler (Idaho Technology). RT-PCR was carried out using a Lightcycler 480 (Roche) with Fast SYBR Green Master Mix for 45 cycles. Fold-change was calculated using ΔΔCt method and normalized to housekeeping genes (actin-β and GAPDH). All forward and reverse primers were designed by Harvard Primer Bank or Primer-BLAST and synthesized by Integrated DNA Technology.

2.4.9 Confocal Microscopy of oxLDL Uptake in Macrophages

[Operation of confocal microscope and image processing were performed by Rebecca Chmielowski, Department of Chemical and Biochemical Engineering, Rutgers University, Piscataway, NJ]

Uptake of oxLDL was visualized using confocal microscopy. PBMCs were isolated from human buffy coats by Ficoll-Paque (1.077 g/cm^3) density gradient and Percoll (1.131 g/cm^3) density gradient. PBMCs were collected and washed with PBS-ETDA (1 mM) and plated into FEP Teflon-coated cell culture bags at a density of at least 5.0 x 10^7 monocytes per bag [41]. Monocytes were differentiated into M2 macrophages using recombinant human M-CSF (2.5 ng/mL) and incubated at 37°C in 5% carbon dioxide in complete medium for 7 d. After 7 d, culture bags were placed on ice for at least 1 h. The cell suspension was removed using a syringe, and cells were isolated by centrifugation (400 g, 10 min). The cells were re-plated at a density of 150,000 cells/mL for at least 12 h prior to treatment. After 24 h co-treatment, cells were washed with PBS (pH 7.4, 3X) and fixed with 4% PFA for 20 min. The PFA solution was removed and Hoescht (0.1 µg/mL) was added for 15 min. Cells were imaged using a Leica TCS SP8 confocal microscope with a 40X oil immersion objective.

2.4.10 Statistical Analysis

Statistical analyses were performed using Graph Pad Prism V7.01. Statistical significance was determined using a one-way ANOVA with Tukey's posthoc test for comparisons between multiple groups.

2.5 Appendix for Chapter 1

2.5.1. Nanoparticles Prepared with Lithocholic Acid-Based AMs and Polystyrene Cores

NPs with 1cM or 1cMLCA shells were also prepared with polystyrene (PS) cores as inert materials following the aforementioned methods. Physicochemical properties of NPs with PS cores were fully characterized and their effects on oxLDL uptake and gene transcription was evaluated. 1cM[PS] NPs had a hydrodynamic diameter larger than all other NPs (232 nm) and a comparable negative ζ potential (-31 mV). 1cMLCA[PS] NPs had both a comparable size and ζ potential to other 1cMLCA-based formulations (173 nm and -31 mV, respectively). Both formulations were effective in inhibiting oxLDL uptake, with comparable results to NPs with alkylLCA cores, being significantly better than 1cM[M12] and 1cMLCA[M12] formulations (**Figure 2.9 A and B**). Additionally, NPs with PS cores had intermediate effects on gene expression levels when compared to NPs with M12 cores and NPs with alkylLCA cores (**Figure 2.9C**). Expression of inflammatory cytokines was significantly reduced from 1cM[M12] and 1cMLCA[M12] formulations, demonstrating that the M12 component of NPs contributes to the observed inflammatory response. As with other formulations, inclusion of the PS core did not have a significant influence on SR expression. These results demonstrate that the NP core identity has an influence on physicochemical and biological properties.

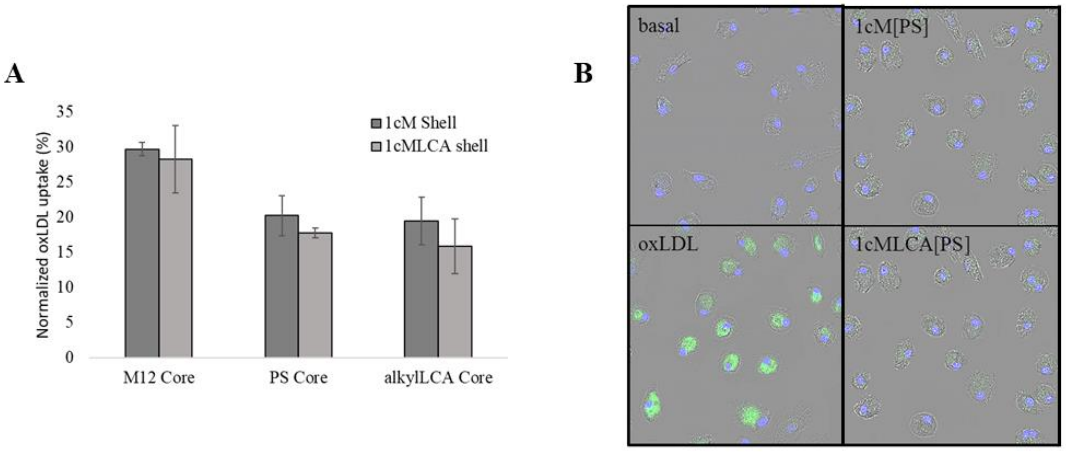

C

	Inflammatory Cytokines					SRs	
	IL-1β	IL-6	IL-8	IL-10	TNFα	CD36	SRA1
1cM[PS]	87	56	53	-2	4	-2	-2
1cMLCA[PS]	107	69	45	-2	3	-3	-3

Figure 2.9. Effect of NPs with PS cores on oxLDL uptake inhibition and gene expression in macrophages. oxLDL uptake was measured via flow cytometry (A) and visualized via confocal microscopy (B). Nuclei are labeled in blue and oxLDL labeled in green. NPs with PS cores were also evaluated for their ability to reduce inflammatory cytokine and SR gene expression (C). Numbers represent fold change from basal controls.

2.5.2. TGR5 Activation Assay for Lithocholic Acid-Based Nanoparticles

LCA-based NPs were designed to activate TGR5. According to their effect on inflammatory cytokines under the control of TGR5, results suggest that LCA-based AMs do, in fact, activate TGR5. To demonstrate this effect, a transfection-based assay with a luciferase reporter gene was attempted according to previous literature reports [36, 42]. In this assay, a TGR5 plasmid is co-transfected into cells with a CRE-Luc plasmid, and Renilla plasmid for transfection efficiency corrections. However, results from the experiment were largely inconclusive. It is possible that the NPs in solution interfere with luminescence from the Luciferase reporter gene, leading to inconsistent results.

2.6. Experimental

2.6.1. TGR5 Activation

HEK293 cells were cultured in Dulbecco's Modified Eagle's medium (DMEM) supplemented with 10% fetal bovine serum (FBS). Cells were plated in 24 well plates (1.25×10^5 cells/well) and incubated for 24 h at 37 °C and 5 % CO_2 (standard conditions) prior to experimentation. Media was removed and replaced with 500 μL of fresh media. Transfection complexes were prepared with Lipofectamine (1.5 μL), Reagent PLUS (0.5 μL), TGR5 plasmid (200 ng), CRE-Luc plasmid (300 ng), and Renilla plasmid (15 μL) in serum-free DMEM. Transfection complexes were incubated at room temperature for 30 min, followed by addition (100 μL) in wells containing plated HEK293 cells. Transfection complexes were incubated with cells for 24 h under standard conditions. Media was removed and replaced with treatment samples (i.e., AM NPs in DMEM) or controls (INT 777, 20 μM and media) followed by an additional 24 h incubation under standard conditions. Luciferase luminescence was evaluated using a cAMP-Glo Assay Kit (Promega, Madison, WI) following manufacturer protocol.

2.7 References

[1] Mozaffarian D, Benjamin EJ, Go AS, Arnett DK, Blaha MJ, Cushman M, et al. Heart Disease and Stroke Statistics—2015 Update: A Report From the American Heart Association. Circulation. 2015;131:e29-e322.

[2] Hansson GK, Libby P. The immune response in atherosclerosis: a double-edged sword. Nature Reviews Immunology. 2006;6:508-19.

[3] Kunjathoor VV, Febbraio M, Podrez EA, Moore KJ, Andersson L, Koehn S, et al. Scavenger Receptors Class A-I/II and CD36 Are the Principal Receptors Responsible for the Uptake of Modified Low Density Lipoprotein Leading to Lipid Loading in Macrophages. Journal of Biological Chemistry. 2002;277:49982-8.

[4] Moore Kathryn J, Tabas I. Macrophages in the Pathogenesis of Atherosclerosis. Cell. 2011;145:341-55.

[5] Iverson NM. Multifunctional polymers for inhibition of oxidized lipoprotein accumulation and inflammation in macrophage cells: Rutgers University-Graduate School-New Brunswick; 2010.

[6] Faig AM. Design, synthesis, and characterization of bioactive amphiphiles for therapeutic applications: Rutgers University-Graduate School-New Brunswick; 2015.

[7] Plourde NM. Structure-binding activity relations of amphiphilic polymers and macrophage scavenger receptors: implications for therapeutic inhibition of atherosclerosis: Rutgers University-Graduate School-New Brunswick; 2010.

[8] Istvan ES, Deisenhofer J. Structural mechanism for statin inhibition of HMG-CoA reductase. Science. 2001;292:1160-4.

[9] Libby P, Aikawa M. Stabilization of atherosclerotic plaques: New mechanisms and clinical targets. Nat Med. 2002;8:1257-62.

[10] Koh KK, Sakuma I, Quon MJ. Differential metabolic effects of distinct statins. Atherosclerosis. 2011;215:1-8.

[11] Golomb BA, Evans MA. Statin adverse effects : a review of the literature and evidence for a mitochondrial mechanism. American journal of cardiovascular drugs : drugs, devices, and other interventions. 2008;8:373-418.

[12] Iverson N, Sparks SM, Demirdirek B, Uhrich KE, Moghe PV. Controllable Inhibition of Cellular Uptake of Oxidized Low Density Lipoprotein: Structure-Function Relationships for Nanoscale Amphiphilic Polymers. Acta biomaterialia. 2010;6:3081-91.

[13] Chnari E, Nikitczuk JS, Uhrich KE, Moghe PV. Nanoscale anionic macromolecules can inhibit cellular uptake of differentially oxidized LDL. Biomacromolecules. 2006;7:597-603.

[14] Chnari E, Nikitczuk JS, Wang J, Uhrich KE, Moghe PV. Engineered polymeric nanoparticles for receptor-targeted blockage of oxidized low density lipoprotein uptake and atherogenesis in macrophages. Biomacromolecules. 2006;7:1796-805.

[15] Faig A, Petersen LK, Moghe PV, Uhrich KE. Impact of Hydrophobic Chain Composition on Amphiphilic Macromolecule Antiatherogenic Bioactivity. Biomacromolecules. 2014;15:3328-37.

[16] Hehir S, Plourde NM, Gu L, Poree DE, Welsh WJ, Moghe PV, et al. Carbohydrate Composition of Amphiphilic Macromolecules Influences Physicochemical Properties and Binding to Atherogenic Scavenger Receptor A. Acta biomaterialia. 2012;8:3956-62.

[17] Abdelhamid DS, Zhang Y, Lewis DR, Moghe PV, Welsh WJ, Uhrich KE. Tartaric acid-based amphiphilic macromolecules with ether linkages exhibit enhanced repression of oxidized low density lipoprotein uptake. Biomaterials. 2015;53:32-9.

[18] Iverson N, Plourde NM, Sparks SM, Wang J, Patel E, Shah P, et al. Dual Use of Amphiphilic Macromolecules As Cholesterol Efflux Triggers and Inhibitors of Macrophage Athero-inflammation. Biomaterials. 2011;32:8319-27.

[19] Chan JW, Lewis DR, Petersen LK, Moghe PV, Uhrich KE. Amphiphilic macromolecule nanoassemblies suppress smooth muscle cell proliferation and platelet adhesion. Biomaterials. 2016;84:219-29.

[20] York AW, Zablocki KR, Lewis DR, Gu L, Uhrich KE, Prud'homme RK, et al. Kinetically Assembled Nanoparticles of Bioactive Macromolecules Exhibit Enhanced Stability and Cell-Targeted Biological Efficacy. Advanced materials (Deerfield Beach, Fla). 2012;24:733-9.

[21] Lewis DR, Petersen LK, York AW, Ahuja S, Chae H, Joseph L, et al. Nanotherapeutics for Inhibition of Atherogenesis and Modulation of Inflammation in Atherosclerotic Plaques. Cardiovascular Research. 2015.

[22] Lewis DR, Petersen LK, York AW, Zablocki KR, Joseph LB, Kholodovych V, et al. Sugar-based amphiphilic nanoparticles arrest atherosclerosis in vivo. Proceedings of the National Academy of Sciences. 2015;112:2693-8.

[23] Petersen LK, York AW, Lewis DR, Ahuja S, Uhrich KE, Prud'homme RK, et al. Amphiphilic Nanoparticles Repress Macrophage Atherogenesis: Novel Core/Shell Designs for Scavenger Receptor Targeting and Down-Regulation. Molecular Pharmaceutics. 2014;11:2815-24.

[24] Pols TW, Nomura M, Harach T, Sasso GL, Oosterveer MH, Thomas C, et al. TGR5 activation inhibits atherosclerosis by reducing macrophage inflammation and lipid loading. Cell metabolism. 2011;14:747-57.

[25] Kida T, Tsubosaka Y, Hori M, Ozaki H, Murata T. Bile acid receptor TGR5 agonism induces NO production and reduces monocyte adhesion in vascular endothelial cells. Arteriosclerosis, thrombosis, and vascular biology. 2013;33:1663-9.

[26] Högenauer K, Arista L, Schmiedeberg N, Werner G, Jaksche H, Bouhelal R, et al. G-Protein-Coupled Bile Acid Receptor 1 (GPBAR1, TGR5) Agonists Reduce the Production of Proinflammatory Cytokines and Stabilize the Alternative Macrophage Phenotype. Journal of medicinal chemistry. 2014;57:10343-54.

[27] Pols TWH, Noriega LG, Nomura M, Auwerx J, Schoonjans K. The bile acid membrane receptor TGR5 as an emerging target in metabolism and inflammation. Journal of Hepatology. 2011;54:1263-72.

[28] Kawamata Y, Fujii R, Hosoya M, Harada M, Yoshida H, Miwa M, et al. A G protein-coupled receptor responsive to bile acids. The Journal of biological chemistry. 2003;278:9435-40.

[29] Levitan I, Volkov S, Subbaiah PV. Oxidized LDL: Diversity, Patterns of Recognition, and Pathophysiology. Antioxidants & Redox Signaling. 2010;13:39-75.

[30] Johnson BK, Prud'homme RK. Chemical processing and micromixing in confined impinging jets. AIChE Journal. 2003;49:2264-82.

[31] Johnson BK, Prud, #39, homme RK. Flash NanoPrecipitation of Organic Actives and Block Copolymers using a Confined Impinging Jets Mixer. Australian Journal of Chemistry. 2003;56:1021-4.

[32] Ansell SM, Johnstone SA, Tardi PG, Lo L, Xie S, Shu Y, et al. Modulating the Therapeutic Activity of Nanoparticle Delivered Paclitaxel by Manipulating the Hydrophobicity of Prodrug Conjugates. Journal of Medicinal Chemistry. 2008;51:3288-96.

[33] Win KY, Feng S-S. Effects of particle size and surface coating on cellular uptake of polymeric nanoparticles for oral delivery of anticancer drugs. Biomaterials. 2005;26:2713-22.

[34] Zhang Y, Li Q, Welsh WJ, Moghe PV, Uhrich KE. Micellar and structural stability of nanoscale amphiphilic polymers: Implications for anti-atherosclerotic bioactivity. Biomaterials. 2016;84:230-40.

[35] Perino A, Pols TWH, Nomura M, Stein S, Pellicciari R, Schoonjans K. TGR5 reduces macrophage migration through mTOR-induced C/EBPβ differential translation. The Journal of Clinical Investigation. 2014;124:5424-36.

[36] Keitel V, Donner M, Winandy S, Kubitz R, Häussinger D. Expression and function of the bile acid receptor TGR5 in Kupffer cells. Biochemical and biophysical research communications. 2008;372:78-84.

[37] Arango Duque G, Descoteaux A. Macrophage Cytokines: Involvement in Immunity and Infectious Diseases. Frontiers in Immunology. 2014;5:491.

[38] von der Thusen JH, Kuiper J, van Berkel TJ, Biessen EA. Interleukins in atherosclerosis: molecular pathways and therapeutic potential. Pharmacol Rev. 2003;55:133-66.

[39] Jurček O, Bonakdarzadeh P, Kalenius E, Linnanto JM, Groessl M, Knochenmuss R, et al. Superchiral Pd3L6 Coordination Complex and Its Reversible Structural Conversion into Pd3L3Cl6 Metallocycles. Angewandte Chemie International Edition. 2015;54:15462-7.

[40] Tian L, Yam L, Zhou N, Tat H, Uhrich KE. Amphiphilic Scorpion-like Macromolecules: Design, Synthesis, and Characterization. Macromolecules. 2004;37:538-43.

[41] Menck K, Behme D, Pantke M, Reiling N, Binder C, Pukrop T, et al. Isolation of human monocytes by double gradient centrifugation and their differentiation to macrophages in teflon-coated cell culture bags. Journal of visualized experiments : JoVE. 2014:e51554.

[42] Li G, Lin W, Araya JJ, Chen T, Timmermann BN, Guo GL. A tea catechin, epigallocatechin-3-gallate, is a unique modulator of the farnesoid X receptor. Toxicology and Applied Pharmacology. 2012;258:268-74.

3. CHAPTER 2: AMPHIPHILIC MACROMOLECULES' DEGREE OF UNSATURATION AND BACKBONE ORIENTATION INFLUENCE LOCAL LIPID PROPERTIES IN LIPOSOMES

[This work is in preparation for publication under the title: "Degree of unsaturation and backbone orientation of amphiphilic macromolecules influence local lipid properties in large unilamellar vesicles." Bin Zhang, Bernice Lee, Meenakshi Dutt, and Kathryn E. Uhrich are co-authors for this work.]

3.1 Introduction

Liposomes are spherical bilayers of lipid molecules (**Figure 3.1**) that have been widely researched for delivery applications [1]. They are highly attractive delivery vehicles due to their biological compatibility, ability to encapsulate both hydrophilic and hydrophobic drugs, and ability to reduce drug-associated toxicity (**Figure 3.1**) [2-4]. Together, these effects widen the safety and solubility profiles of deliverable drugs. As such, liposome use has enabled the clinical application of drugs that would otherwise be insoluble or have detrimental side effects. Since their invention, liposome-based delivery vehicles have been translated to the clinic for treatment of breast cancer, ovarian cancer, severe fungal infections, and various other applications [5]·[6]. Most notably, the cytotoxic chemotherapeutic agent doxorubicin was the first liposomal formulation approved for treatment of AIDS-related Kaposi's sarcoma and ovarian cancer when formulated with hydrogenated soy phosphatidylcholine (HSPC), cholesterol, and poly(ethylene glycol) (PEG) as a liposomal suspension known as Doxil® [5, 7].

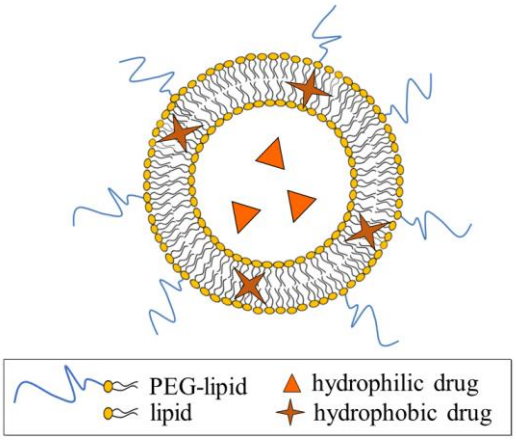

Figure 3.1 Schematic representation of a liposome stabilized with PEG-lipids. Liposome is depicted encapsulating hydrophilic drugs in the aqueous interior and hydrophobic drugs in the lipid bilayer.

Despite several clinical successes, liposomal delivery systems may still suffer from poor drug retention and associated toxicity issues, short circulation times, and limited stability [1, 8]. To address these shortcomings, complicated formulations incorporating a variety of stabilizing molecules, targeting agents, and triggered release additives are often employed [6, 9-11]. PEG has become a ubiquitous additive to provide a stabilizing hydration shell that also shields the vesicles from mononuclear phagocyte system (MPS) uptake, thereby extending circulation times [4, 8, 9]. Methods utilized to impart liposomes with this "stealth shield" include grafting PEG to the surface of liposomes or incorporating PEG in the form of PEGylated lipids (e.g., distearoylphosphatidylcholine- (DSPC-) PEG) at low percentages [12-15]. Although PEG-lipids are the most commonly used stabilization agent, recent research has focused on the development of non-phospholipid alternatives to combat high costs associated with lipid synthesis and extraction methods, enzymatic susceptibility, and poor storage stability [12, 16-19]. For example, Heyes et al. have designed diacylglycerol alternatives to PEG-lipids that show improved chemical, and thus liposomal, stability [16].

In addition to using excipients to promote colloidal stability, the liposomal physicochemical properties can be altered during vesicle preparation to control drug encapsulation and release rates. For example, the lipid hydrocarbon tail length will largely control liposome phase behavior and drug retention. Longer lipid tail lengths form liposomes in the gel phase that demonstrate improved drug retention compared to lipids with shorter tails [20-22]. Encapsulation and release properties of liposomes may also be influenced by vesicle lamellarity. Multilamellar vesicles generally encapsulate a greater quantity of hydrophobic drugs and release hydrophilic drugs at slower release rates relative to unilamellar vesicles [23]. However, multilamellar vesicles suffer from poor uniformity and are commonly processed further to obtain the higher reproducibility associated with unilamellar vesicles [24]. As such, alternative approaches to achieve extended, sustained therapeutic doses are needed. Current mechanisms include formulating liposomes with polymers or hydrogels, such as Polaxamer 407, which forms an *in situ* gel shown to prolong the analgesic effect of ibuprofen compared to liposomal controls [25-27]. DepoFoam®, an FDA-approved technology, is a unique formulation of multivesicular liposomes that assemble into a honeycomb-like architecture and result in increased stability and sustained release duration that can be tuned for delivery time scales up to thirty days [28-30].

An alternative to changing liposome preparation methods is to design an additive that can stabilize liposomes and have the structural versatility to control drug release. It has previously been demonstrated that amphiphilic macromolecules (AMs), designed by the Uhrich group, extend the stabilizing effect of cholesterol on dipalmitoylphosphatidylcholine (DPPC)-based liposomes [31]. Herein, we expand upon the AM design to generate molecules to serve as the sole liposome stabilizing agent (i.e., removing cholesterol from the formulation) as well as influence drug release rates. Two series of AMs were developed with different backbone architectures that allow AM hydrophobic domains to intercalate differently into DSPC bilayers (**Figure 3.2**). A glycerol-based backbone was chosen to mimic commonly used PEG-lipids' architecture such that the AMs'

hydrophobic domains align parallel with lipid tails. For the second series, a tartaric-acid based backbone was used with the hypothesis that the hydrophobic domains will not be parallel with DSPC tails. This design would potentially provide the advantage of lipid tails tangling with the hydrophobic domains of AMs, resulting in increased AM retention and extended liposome stability. In each series, the number of double bonds in the hydrophobic domain was varied from zero to two, resulting in differences in fluidity. We hypothesized that increased fluidity would alter local membrane characteristics and impact hydrophilic drug release rates. To test these hypotheses, two series of AMs were synthesized and formulated with DSPC lipids at various incorporation percentages. Liposomes were evaluated for stability under physiological and storage conditions, and the impact of the hydrophobic domain characteristics were evaluated via release monitoring of a hydrophilic dye. In addition, computational modeling of AMs in DSPC lipid membranes was performed to provide mechanistic insights into the structural behavior.

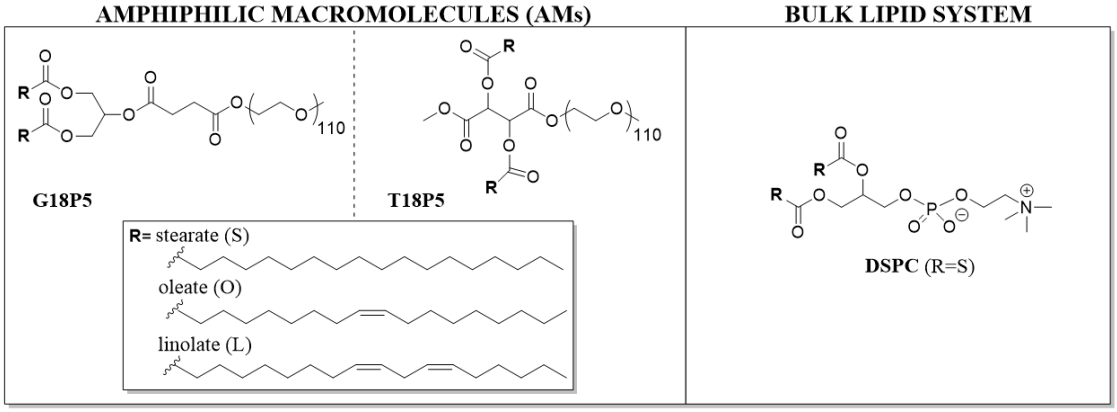

Figure 3.2: Chemical structures of AMs and bulk lipid system. AM series based on a glycerol backbone (G18P5) or tartrate backbone (T18P5) with fatty acid-based arms (stearate, oleate, or linoleate) on the left, and DSPC lipid on the right used as the bulk lipid for liposome formulation.

3.2 Results and Discussion

Two series of AMs were designed to partition into DSPC liposomes to promote liposomal stability and control drug release rates. Within each series, the fluidity of AMs was altered by

increasing the number of double bonds in the AM hydrophobic domain to promote local membrane disruptions, thus facilitating a controlled rate of hydrophilic drug release. In this work, the successful synthesis and characterization of AMs, their influence on liposome stability characteristics and model hydrophilic drug release profiles are presented, and MD simulation results are utilized to provide a mechanistic insight into the liposomal characteristics.

3.2.1 Unsaturated AMs Successfully Synthesized

Syntheses of glycerol-based AMs (i.e., G18P5 series) were carried out following the scheme depicted in **Figure 3.3A**. Synthesis was initiated by protecting the primary glycerol hydroxyls to allow for PEG-conjugation to the secondary alcohol. Evidence of TBDMS protection was evident through the appearance and relative integrations of the methyl groups at 0 ppm and 0.84 ppm in the ^{1}H-NMR spectrum (**Figure 3.4**), and characteristic Si-CH_3 peaks in the FT-IR spectrum at 1257 cm^{-1}. Ring-opening of succinic anhydride was then carried out using TEA as a proton acceptor to generate the same PEG-ester linkage as the T-series of AMs. Peaks representative of conjugated succinate protons at 2.58 and 2.62 ppm in the ^{1}H-NMR spectrum were utilized to confirm successful synthesis. PEG was then conjugated using DCC/DPTS, and the TBDMS protecting groups were removed using TBAF as a source of fluoride ions under acidic conditions to assure the esters would not be cleaved. Successful PEG conjugation and TBDMS deprotection were confirmed via the appearance and relative integration of the PEG peak at 3.60 ppm and the disappearance of TBDMS peaks in the ^{1}H-NMR spectra, respectively. The hydrophobic arms were added using standard carbodiimide coupling conditions to result in the final products G18P5-S, G18P5-O, and G18P5-L. The ^{1}H-NMR spectra of final products contain peaks consistent with those expected for successful fatty acid conjugation.

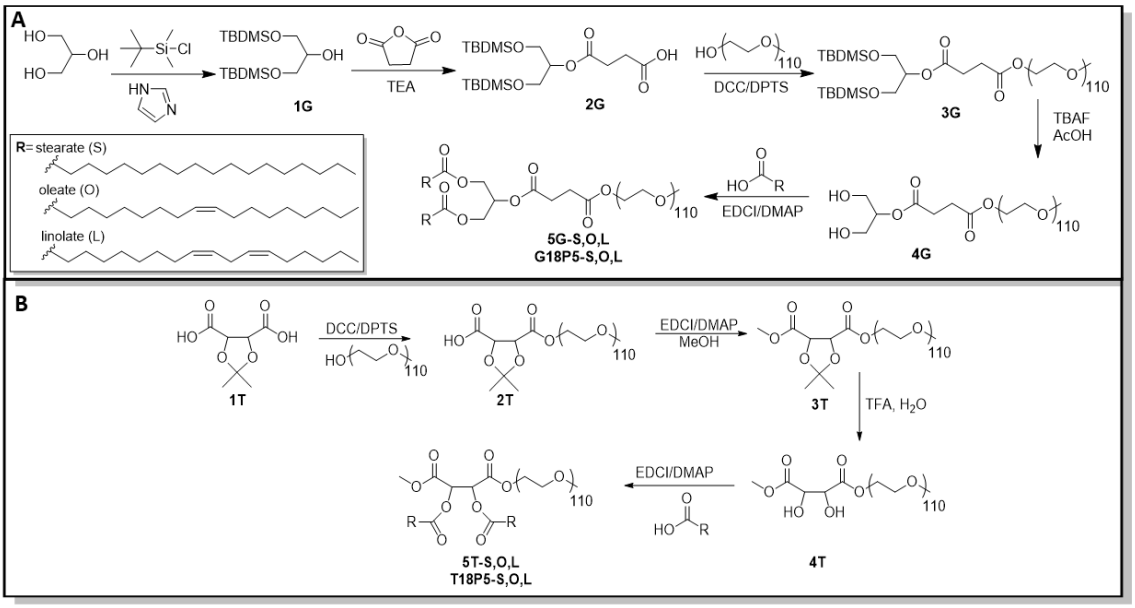

Figure 3.3: Synthetic schemes used for synthesis of AMs. Synthesis of G18P5 (A) and T18P5 (B) series of AMs are outlined.

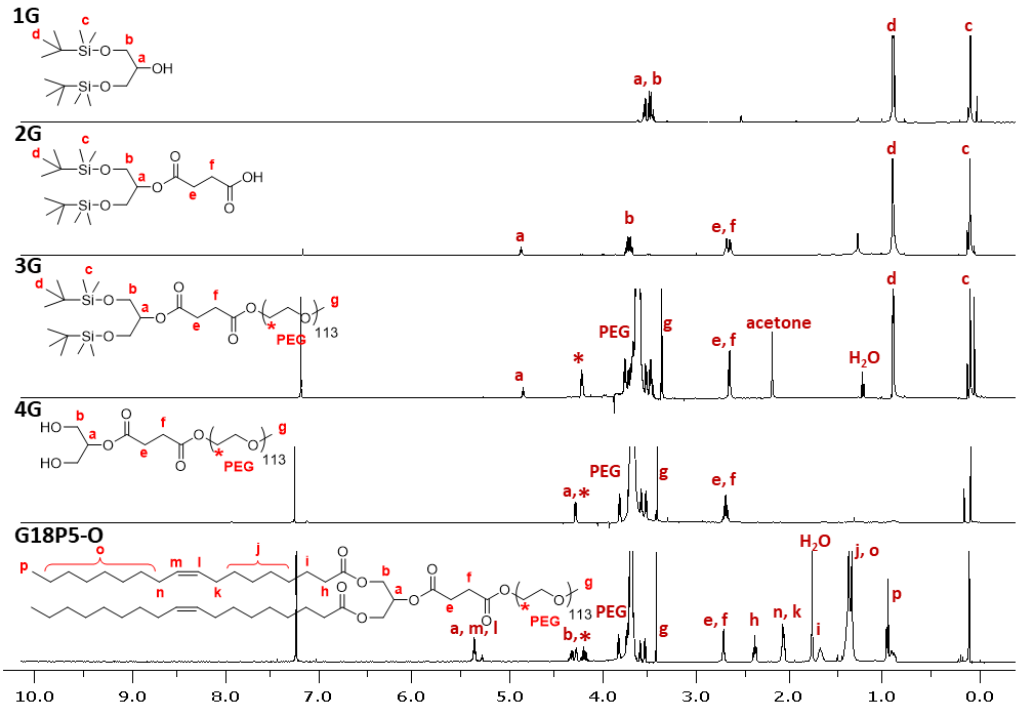

Figure 3.4: Sequential NMR spectra in the synthesis of G18P5 series using G18P5-O as an example

The tartrate-based AM (i.e., T18P5 series) syntheses were carried out in a similar manner (**Figure 3.3B**). Previous attempts to prepare the hydrophobic domain followed by PEG-conjugation, as is used for shorter arm lengths (i.e., (<16 carbons), proved unsuccessful due to steric bulk [32]. As such, an alternative approach was utilized starting from dimethyl-2,3-O-isopropylidene-*L*-tartrate. The starting material was first conjugated to PEG via DCC/DPTS coupling and confirmed via relative ^{1}H-NMR proton integrations of the PEG peak at 3.60 ppm and the tartrate methine peaks at 4.71 ppm as shown in **Figure 3.5**. The terminal acid functionality was protected with a methyl group to assure a net neutral charge and remain consistent with the glycerol-based AM series and confirmed via the appearance of a methyl peak in the ^{1}H-NMR spectrum at 3.81 ppm. The isopropylidene group was removed using TFA and a small amount of water as a catalyst in chloroform to generate the PEGylated methyl tartrate, as evidenced by the disappearance of isopropylidene methyl groups and the shift of tartrate methines to 3.49 ppm. Fatty acids were

conjugated and characterized as previously described using EDC/DMAP coupling to generate the final products, T18P5-S, T18P5-O, and T18P5-L.

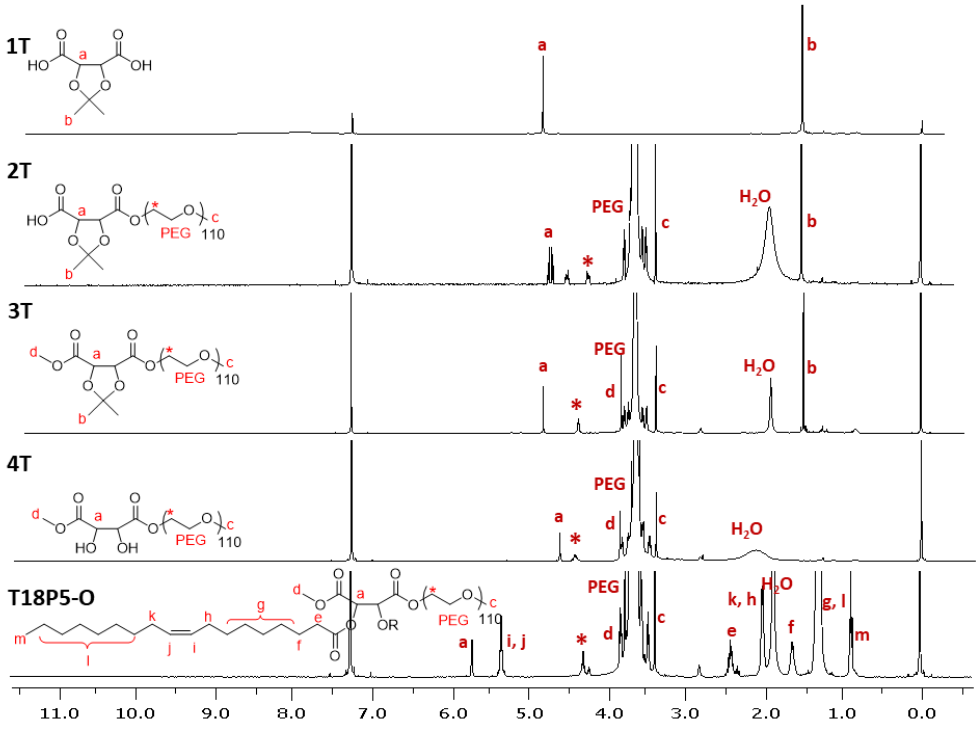

Figure 3.5: Sequential NMR spectra in the synthesis of T18P5 series using T18P5-O as an example

3.2.2 AMs Stabilize Formation of Large Unilamellar Vesicles

The two series of AMs were designed to understand the roles of chemical structure on liposome characteristics. DSPC lipids are capable of forming vesicles upon addition of a variety of compounds, such as cholesterol or PEG-lipids, but quickly aggregate in the absence of such stabilizing agents [5, 33]. While cholesterol is commonly used as an effective stabilizing agent, PEG-lipids provide the additional advantage of extending circulation time [34]. LUVs were generated via the thin-film hydration and extrusion method incorporating each AM at 2, 4, and 6 mol%. Higher concentrations of AM were not evaluated as analogous PEG-lipids have been shown to form mixed micellar structures in addition to liposomes at concentrations greater than 7 mol% [14, 35]. All eighteen formulations resulted in vesicles, whereas DSPC lipids alone did not result

in any stable vesicles as observed by DLS. TEM with negative staining further confirmed the unilamellar and spherical architecture of vesicles as shown in **Figure 3.6**.

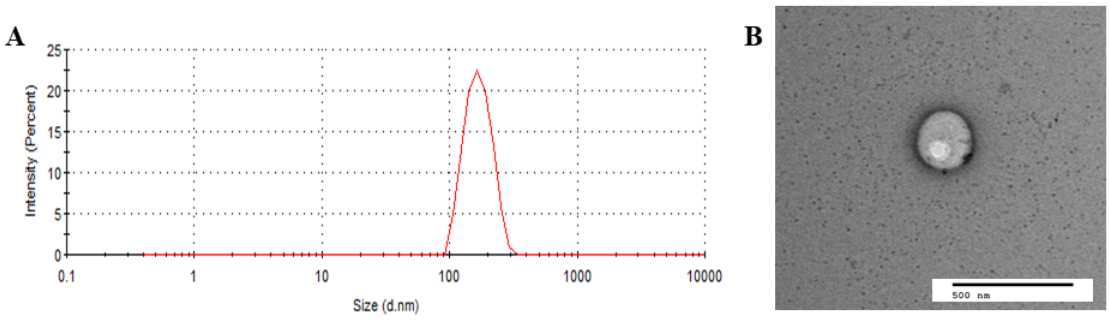

Figure 3.6: Size of DSPC LUVs with G18P5-S incorporated at 6 mol%. Size distribution as measured by DLS (A) indicates a narrow monodistribution. TEM image (B) of DSPC liposomes with G18P5-S at 6 mol% incorporation shows ~200 nm diameter vesicles with single negatively stained bilayer.

The hydrodynamic diameters of LUVs with stearate- and oleate-based AMs were approximately 170 nm at room temperature and approximately 130 nm at physiological temperature. The consistency in size is anticipated, as the method of extrusion used for LUV preparation results in liposomes with diameters approximately the size of the membrane pores [36]. LUVs incorporating T18P5-L AMs deviated from this trend, resulting in vesicles with hydrodynamic diameters about 50-80 nm larger. This deviation served as an early indicator of the weaker stabilizing effect of T18P5-L on DSPC liposomes compared to the G18P5-L series, which resulted in diameters consistent with the remaining formulations.

3.2.3 Extent of LUV Stabilization is Dependent on Hydrophobic Domain Characteristics

As AMs exhibit an amphiphilic nature similar to PEG-lipids, they are capable of partitioning into DSPC bilayers to promote steric stabilization [31]. The PEG portion of AMs

provides a hydration shell around vesicle bilayers that prevents aggregation of neighboring LUVs. LUVs incorporating AMs at varying ratios were monitored for stability under storage conditions (RT, 25 °C) and physiological temperature (37 °C) using DLS. Drastic size increases of liposomes to the micromolar range or multimodal peak distributions were interpreted as indications of liposome aggregation and instability. Incorporation of each AM demonstrates an improvement in liposome formation and stability at incorporation ratios as low as 2 mol% (**Figure 3.7**). All AMs with stearate and oleate arms stabilized LUVs at as low as 2 mol% incorporation for the time frames evaluated. No significant size increases in liposome particles was observed for a four-week time frame at room temperature or at an elevated temperature for seven days for AMs with stearate and oleate arms (**Figure 3.7**). As DSPC lipids are unable to form stable liposomes without any additives, the stability imparted by the incorporation of AMs at low percentages demonstrates their ability to promote stabilization at varying temperatures.

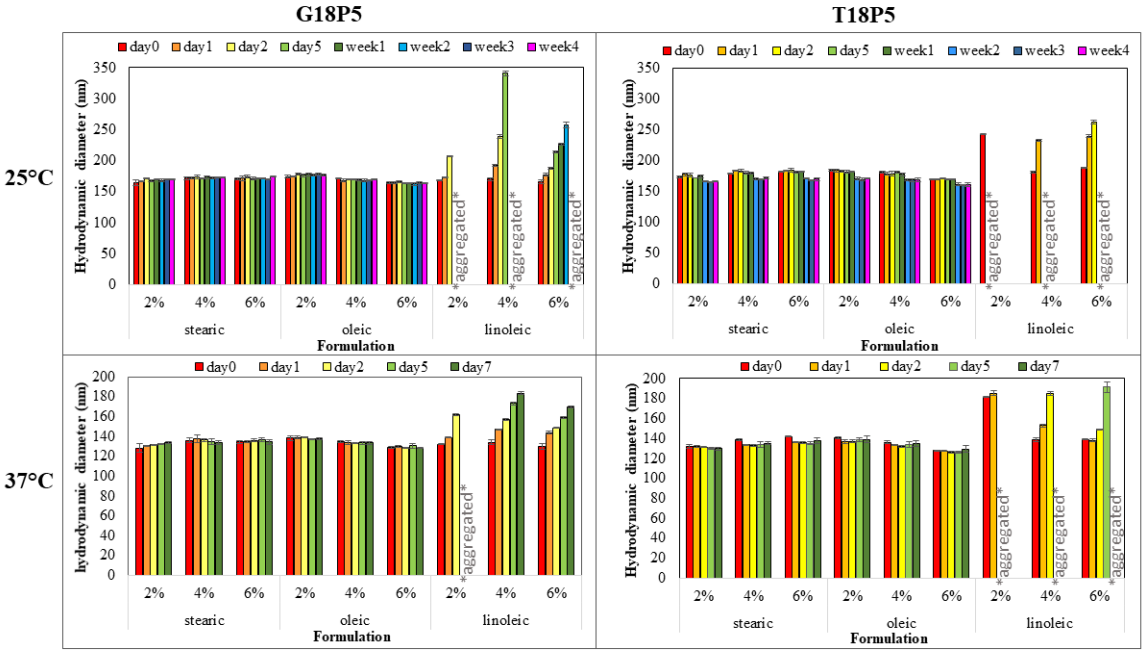

Figure 3.7: Stability characterization of all liposome formulations with G- and T- series of AMs incorporated at 2, 4 or 6 mol% as measured by DLS at room and physiological temperatures

However, formulations containing AMs with linoleate tails were not stable against aggregation over extended time periods at either temperature as shown in **Figure 3.8**, suggesting that two double bonds in the hydrophobic domain results in poor mixing with saturated DSPC lipids. This observation is consistent with literature, where an increase in unsaturation results in decreased liposome stability [13, 37]. In these results, the AM backbone also had a significant impact on liposome stability. G18P5-L exhibited a stronger stabilizing effect on DSPC LUVs compared to T18P5-L at all mol% incorporations, indicating that the glycerol backbone is more compatible with the lipid system. At room temperature, LUVs with 6 mol% G18P5-L were relatively stable against aggregation for two weeks, with only a minimal increase in liposome size. In contrast, LUV's with 6 mol% T18P5-L only formed stable liposomes for two days. A similar effect was observed at an elevated temperature, where G18P5-L stabilized liposomes at 4 and 6 mol% for a full week without any indications of aggregation. However, T18P5-L incorporation at 6 mol% showed evidence of particle instability after five days. These data suggest that the similar architecture between the hydrophobic domains of glycerol-based AMs and DSPC contributes to LUV stabilization.

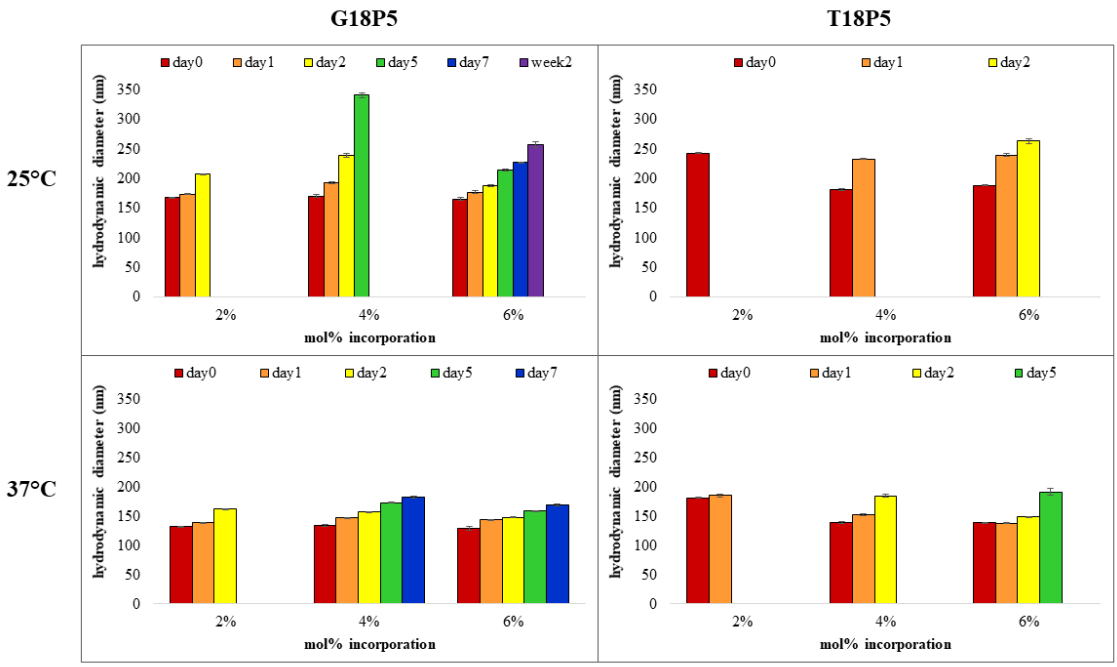

Figure 3.8: Stability of LUVs containing linoleic-based AMs as assessed by DLS measurements. Graphs are shown at varying mol percent incorporations at room temperature (top panels) and physiological temperature (bottom panels) exhibit dependency on backbone architecture. Glycerol-based AMs (left) show improved stabilization at both temperatures, resulting in LUV for longer time frames that analogous tartrate-based AMs (right).

Computational modeling of AMs incorporated into DSPC bilayers was used as a tool to better understand the AMs' influence on particle stability. **Figure 3.9** shows AM conformations in DSPC bilayers. These snapshots indicate that the arms of AMs with no double bonds in the hydrophobic domain are ordered and well packed in the DSPC bilayer. This result is anticipated, as both the AMs and DSPC have stearate-based hydrocarbon chains. Disorder in the bilayer becomes evident for AMs with higher degrees of unsaturation, and the excluded volume resulting from the AM arms increases with the number of double bonds, affecting the packing and conformation of neighboring lipids. It is possible that the disorder induced by AMs disrupts the packing of the nearby lipids, thereby, inducing a local fluid phase. Consequently, bilayer stability

would decrease with increasing AM unsaturation, which is experimentally observed once the AM hydrophobic domains contain two double bonds. It should also be noted that in the computational results, the tartrate backbone does not appear to disturb this alignment, and the hydrophobic arms are well aligned with DSPC hydrophobic domains, which would result in stabilization of liposomes, as observed.

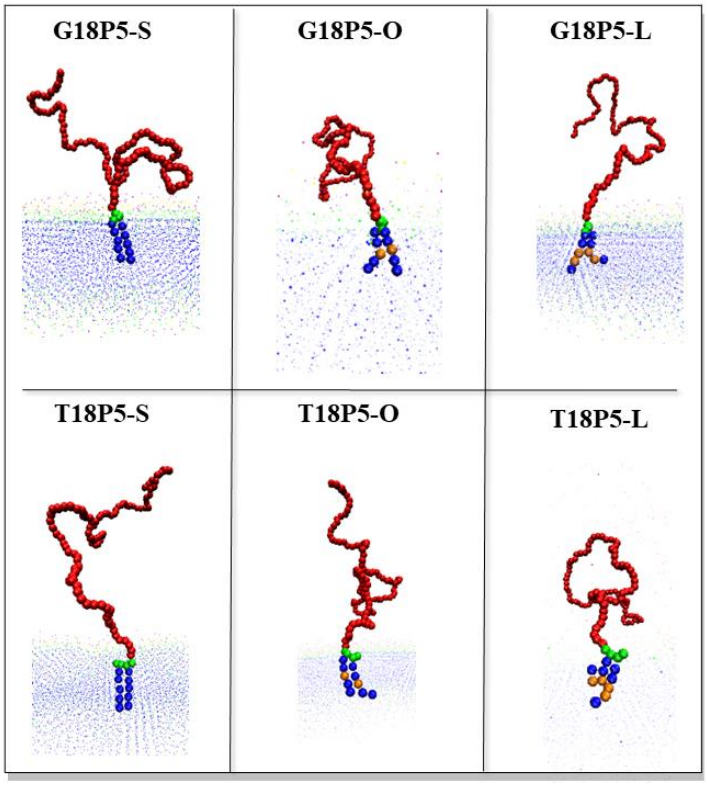

Figure 3.9: MD snapshots of AMs incorporated in DSPC bilayers indicating hydrophobic domain disorder for AMs with unsaturated arms. DSPC molecules are minimized for clarity. The color designations for AMs are as follows: red-PEG, green-backbone, blue-saturated carbon domains, orange- unsaturated regions.

3.2.4 AMs Stabilize Liposomes at Higher Incorporation Ratios

Stability trends are also strongly dependent on the mol% incorporation of AMs for both linoleate series. Formulations with lower incorporation ratios aggregate on a faster time scale under

both temperature conditions, indicating that the PEG shell also contributes to liposome stability. For example, LUVs with 6 mol% incorporation of G18P5-L were stable against aggregation for two weeks at room temperature compared to two days at 2 mol% incorporation (**Figure 3.8**).

MD simulations provided additional insight into the effect of PEG on LUV stabilization. The results show an increase in the PEG corona thickness with increasing AM concentrations. As PEG chains are known to provide a hydration shell that prevents the liposomes from aggregating, a higher density of AMs increases the barrier to aggregation, thereby improving stability [12, 13]. As shown in **Figure 3.10**, higher AM concentrations induce the PEG chains to adopt brush-like conformations, enabling the individual PEG chains to maximize their conformational entropy as the area per AM reduces. Consequently, the PEG corona is thicker with increasing AM concentration. Brush-like conformations of the PEG chains at high PEG grafting densities are more likely to shield the bilayer surface from neighboring liposomes and prevent their aggregation [14]. For AM molecules with larger spaces between themselves (i.e., low concentration of AM molecules), the PEG chains adopt mushroom-like conformations, which are much more likely to expose the bilayer surface to approaching liposomes, thereby resulting in aggregation [38]. These results agree with experimental observations that demonstrate liposomes with higher AM concentrations have a lower tendency to aggregate. Hence, the PEG corona from AMs effectively increases liposome colloidal stability.

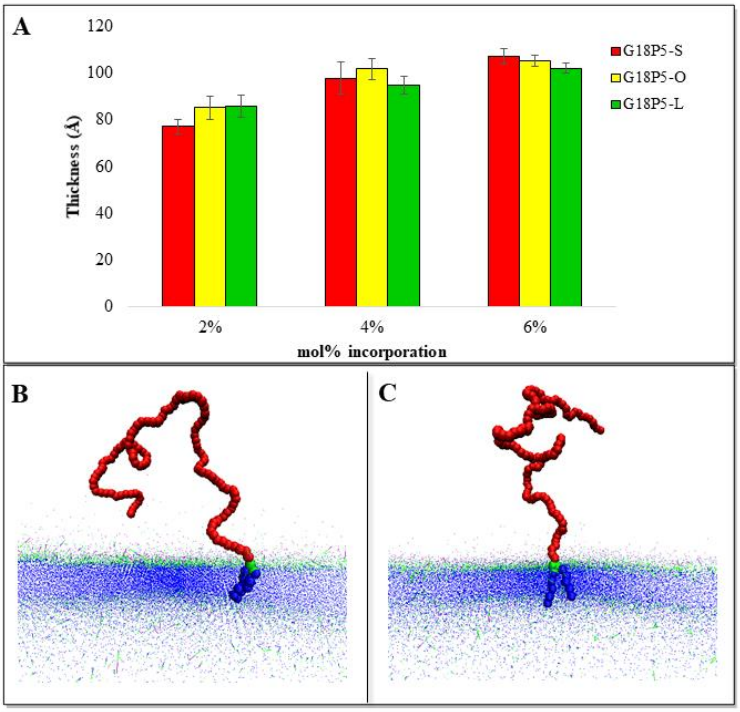

Figure 3.10: Influence of AM mol % incorporation on PEG features. The PEG shell around LUVs influences stability by becoming thicker at higher AM incorporation ratios and promoting steric stabilization (A). At 2 mol%, the PEG domain adopts a mushroom-like conformation (B), and at 6 mol%, PEG forms a brush-like conformation (C), leading to differences in PEG corona thickness, and thus, stabilization properties at different AM incorporation percentages.

Computational calculations further indicate that the PEG bead density is higher closer to the bilayer and steeply decreases further away from the center of the bilayer at 2 mol% incorporation of AMs. Additionally, the PEG beads are more uniformly distributed in the corona and remain nonzero at further distances from the bilayer for 4 mol% and 6 mol% AM incorporation (**Figure 3.11**). With higher AM grafting density, the lateral volume available to each PEG chain will be smaller. When the PEG is in a mushroom conformation, the lower layers of the corona will be dense, whereas brush conformations will result in a more uniform PEG density in each layer. As shown through the computational modeling and confirmed via experiment, the more uniformly

distributed PEG corona at high AM concentrations endows liposomes with greater stability, thereby preventing aggregation.

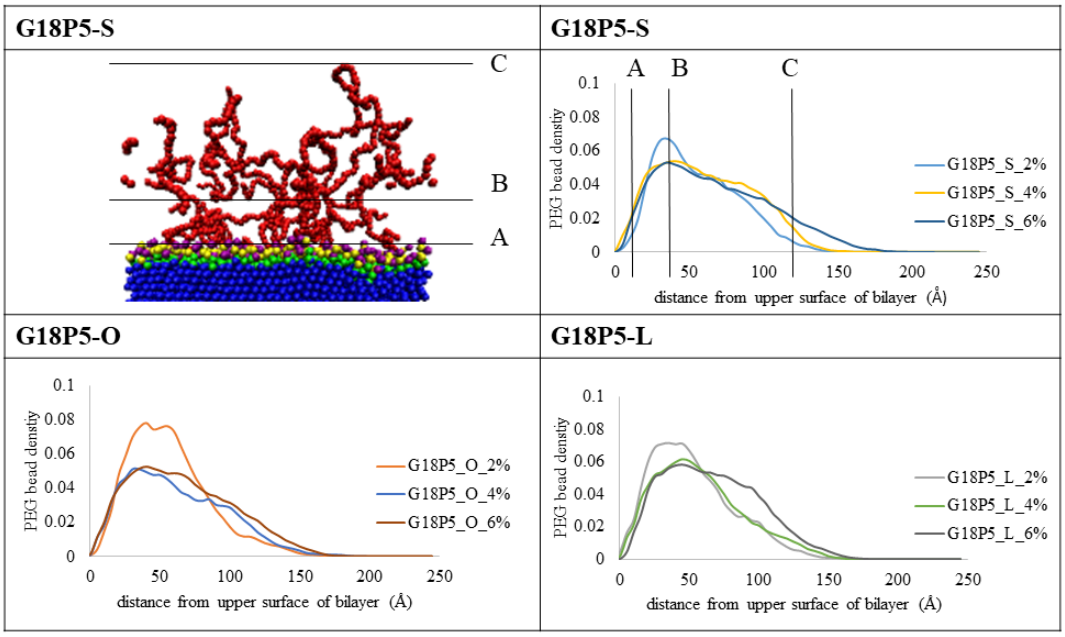

Figure 3.11: Computational PEG bead density measurements indicating PEG tail distribution with respect to distance from the DSPC bilayer for liposomes stabilized with glycerol-based AMs. Molecular dynamics snapshot with A, B, and C indicating locations of interest in graphs (top left). Corresponding locations are indicated in top right graph.

3.2.5 Degree of AM Unsaturation Influences Hydrophilic Dye Release

Typically, controlling the release rate of encapsulated cargo from liposomes has primarily been achieved through changing the bulk lipid system or formulating liposomes with hydrogel systems. In this work, AMs also influenced membrane fluidity, thus controlling the release rate from LUVs. The membrane properties of DSPC liposomes were therefore evaluated by monitoring hydrophilic dye release, sulforhodamine B (SRB), from LUVs incorporating each AM. Only the highest mol% incorporation ratio was assessed for each formulation, as linoleate-based AMs showed the strongest stabilizing effect at this percentage.

As shown in **Figure 3.12**, pre-formed LUVs were loaded with SRB via a pH gradient and SRB release was monitored over one week at physiological temperature. After one week, the samples were treated to recover the SRB remaining within the LUVs. Similar general trends were observed for both the G- and T-series of AMs incorporated in DSPC liposomes. Stearate-based AMs resulted in the slowest release, followed by oleate-based AMs, and linoleate-based AMs had the quickest release. The identity of the AM backbone did not have as significant of an effect on SRB release. AMs with stearate arms had minimal release for both series, and AMs with oleate arms had comparable release for T18P5-O and G18P5-O, releasing 16% and 23% of the SRB over seven days, respectively. However, AMs with linoleate tails differed between the two series. T18P5-L incorporated into DSPC LUVs resulted in 48% SRB release, slightly more than G18P5-L, which released 33% over the measured time period. The results indicate that both the backbone orientation and the degree of unsaturation in AM hydrophobic arms influence membrane permeability.

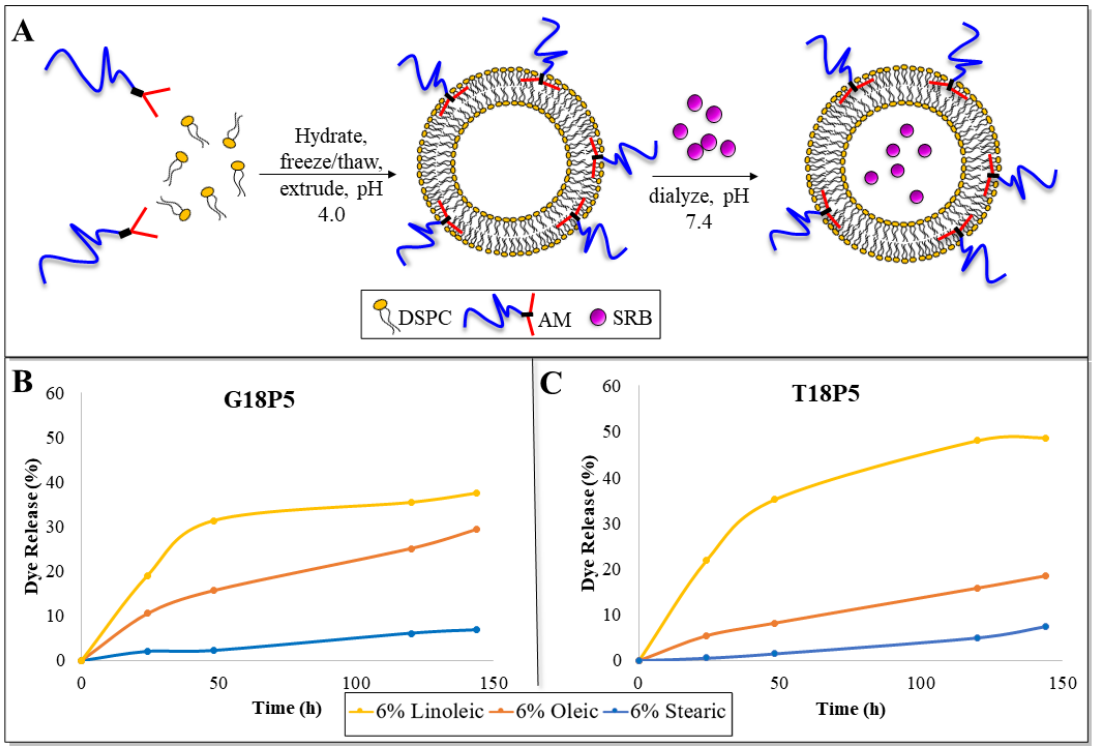

Figure 3.12: SRB dye release rates from DSPC liposomes with AMs incorporated at 6 mol% directly correlates to the degree of unsaturation in AM hydrophobic domains. Schematic depicting formation of LUVs and encapsulation of dye using a pH gradient (A). Release curves of G18P5 (B) and T18P5 (C) series of AMs.

These experimental observations are corroborated by the previously outlined computational modeling results. The membrane disturbances resulting from AM incorporation cause a local decrease in the order of the surrounding lipids. The changes in lipid behavior will impact membrane permeability and dye release rates. AMs with stearate arms do not result in a significant amount of dye release, likely because the AM arms are well aligned with DSPC tails, allowing the local lipid system to remain in the gel-phase. However, as the degree of AM unsaturation increases, the hydrophilic dye is released at a quicker rate, indicating that the membrane is more fluid. The MD simulations show that the oleate-based AM arms are more poorly aligned with DSPC arms, resulting in more lipid disruption, and linoleate-based AMs have the most

significant disruption in lipid behavior. These trends follow those found experimentally for hydrophilic dye release, suggesting that AMs influence local membrane fluidity, and thus permeability to hydrophilic cargo.

3.3 Conclusion

AMs were strategically designed to serve as the sole stabilizing agent for DSPC liposomes while concurrently imparting the liposomal delivery system with controlled release capability by tuning the number of double bonds in the hydrophobic domain. All AMs successfully stabilized DSPC liposomes at low incorporation percentages, and AMs with stearate and oleate arms showed no aggregation over extended time periods. Linoleate-based AMs have a weaker stabilizing effect due to poor hydrophobic domain compatibility, but reveal that the PEG shell density has a significant impact against aggregation protection. The degree of unsaturation in AM hydrophobic domains additionally controls the release rate of hydrophilic cargo from the vesicle interior. MD simulations reveal that AM unsaturated domains occupy larger areas than their saturated analogues, thus disrupting the packing and behavior of neighboring lipids. This results in a local increase in membrane fluidity and permeabilizes the lipid interior to allow hydrophilic cargo to leak out. The AMs synthesized in this work reveal critical phenomena to design agents that can serve the dual purpose of stabilizing delivery systems and controlling release of encapsulated cargo.

3.4 Experimental

3.4.1 Materials

3.4.1.1 Chemicals

All reagents were purchased from Sigma-Aldrich (St. Louis, MO) and used as received unless otherwise noted. DSPC was purchased from Avanti Polar Lipids (Birmingham, AL). Uranyl acetate was purchased from Electron Microscopy Sciences (Hatfield, PA), and carbon coated grids

were purchased from Ted Pella (Redding, CA). Polytetrafluoroethylene (PTFE) syringe filters were purchased from Fisher Scientific (Fair Lawn, NJ).

3.4.1.2. Computational tools

Large-scale Atomic/Molecular Massively Parallel Simulator (LAMMPS) package was used for computation experiments. All the computational characterization was performed using inhouse Visual C++ 6.0 analysis routines.

3.4.2. Characterization

Proton (^{1}H) and carbon (^{13}C) nuclear magnetic resonance (NMR) spectra were obtained on a Varian spectrometer (400 MHz or 500 MHz). Products and intermediates were dissolved in deuterated chloroform ($CDCl_3$) with trimethylsilane (TMS) as an internal reference or deuterated dimethyl sulfoxide (DMSO-d_6). Fourier transform infrared (FT-IR) spectra were obtained on a Thermo Scientific Nicolet iS10 spectrophotometer by solvent-casting small molecules onto sodium chloride (NaCl) plates from dichloromethane (DCM) solutions. An average of 32 scans per sample were recorded and processed using OMNIC software. Small molecule molecular weights were determined with a ThermoQuest Finnigan LCQ-DUO system equipped with a syringe pump, optional divert/inject valve, atmospheric pressure ionization (API) source, and mass spectrometer (MS) detector. All spectra were processed using the Xcalibur data system. Compounds (10 µg/mL) were dissolved in methanol (MeOH) or DCM with 1% acetic acid or ammonia for positive or negative ion detection, respectively. Weight-averaged molecular weights (Mw) and polydispersity indices (PDI) of AMs were determined by gel permeation chromatography (GPC) on a Waters liquid chromatography (LC) system (Milford, MA), with a 2414 refractive index detector, 1515 isocratic HPLC pump, 717plus autosampler, and Jordi divinylbenzene mixed-bed GPC column (7.8 x 300mm, Alltech Associates, Deerfield, IL). Samples (10 mg/mL) were prepared in DCM and filtered through a 0.45 µm PTFE syringe filter. The eluent (DCM) was set at 1 mL/min, and IBM

ThinkCentre computer with WaterBreeze version 3.20 software used to process data as compared to a calibration curve generated with broad-range PEG standards (Waters Milford, MA).

3.4.3. Synthesis

3.4.3.1. G series of AMs

AMs based on a glycerol backbone were synthesized following the **Figure 3.3A**. The primary alcohols of glycerol were selectively protected with tert-butyl dimethylsilyl chloride (TBDMS-Cl) as described elsewhere [39]. **1G** (1.0 eq., 2.6 mmol) was dissolved in 10 mL anhydrous DCM under nitrogen, followed by addition of succinic anhydride (1.5 eq., 3.8 mmol) and triethylamine (TEA, 4.00 eq. 10.4 mmol). The reaction was stirred overnight, washed with 1 N HCl (2X, 15 mL) and brine (1X, 15 mL). The organic layer was dried over magnesium sulfate ($MgSO_4$), filtered, and concentrated *in vacuo* to obtain pure **2G**.

2G (2.0 eq., 0.28 mmol) and 4-(dimethylamino) pyridinium-4-toluene sulfonate (DPTS, 1.1 eq., 0.16 mmol) were dissolved in 5.0 mL of anhydrous DCM under nitrogen. This solution was added to methoxy-terminated PEG (mPEG-OH, 1.0 eq., 0.14 mmol) dissolved in 5.0 mL of anhydrous DCM, followed by addition of N,N'-dicyclohexylcarbodiimide (DCC, 1 M, 2.0 eq., 0.28 mmol). After 24 h, the urea byproduct was removed via filtration, the filtrate washed 2X with 1 N hydrochloric acid (HCl) and 1X with brine, and the solvent removed *in vacuo*. Crude **3G** was dissolved in minimal DCM, precipitated in diethyl ether (15 mL), and collected via centrifugation (3500 rpm, 5 min each) with a total of 5 washes to obtain pure **3G**.

TBDMS protecting groups were removed following a published procedure [40]. Tetrabutylammonium fluoride (TBAF, 1 M, 8.0 eq., 0.82 mmol) was added to a solution of **3G** (1.0 eq., 0.10 mmol) in 10.0 mL of anhydrous tetrahydrofuran (THF) with 1 % acetic acid (AcOH). After 24 h, solvent was removed *in vacuo*, the residue resuspended in DCM, and washed with sodium bicarbonate (2X, 10 mL), deionized water (1X, 10 mL), and brine (1X, 10 mL). The organic

layer was dried over $MgSO_4$, and after concentrating, **4G** was purified via precipitation in diethyl ether as described for **3G**.

Alkyl acid arms were conjugated to free alcohols of **4G** via carbodiimide coupling. Conjugation to oleic acid is given as an example. Oleic acid (2.2 eq., 0.21 mmol) and dimethylaminopyridine (DMAP, 2.2 eq., 0.21 mmol) were dissolved in 10 mL anhydrous DCM under nitrogen. **4G** (1.0 eq., 0.10 mmol) and N-(3-dimethylaminopropyl)-N-ethylcarbodiimide hydrochloride (EDCI, 2.5 eq., 2.4 mmol) were added, and the reaction stirred overnight. The mixture was washed with 10 % potassium bisulfite (2X, 15 mL), and brine (1X, 15 mL) to remove the urea byproduct and DMAP. **5G** was purified as described for PEGylated compounds.

1,3-di-TBDMS glycerol (**1G**): Yield: 82% (clear oil) ^{1}H-NMR (500 MHz, $(CD_3)_2SO$): δ 0.00 (s, 12H), 0.84 (s, 18H), 3.40-3.52 (m, 5H). ^{13}C-NMR (500 MHz, $(CD_3)_2SO$): δ -0.01, 23.25, 31.17, 69.22, 77.61 IR (cm^{-1}, thin film): 1257 (Si-CH_3), 3474 (-OH). ESI-MS m/z: 321.8 $[M+1]^+$

1,3-di-TBDMS glycerol succinate (**2G**): Yield: 82% (light yellow solid) ^{1}H-NMR (500 MHz, $CDCl_3$): δ 0.00 (s, 12H), 0.83 (s, 18H), 2.58-2.62 (dd, 4H), 3.66-3.70 (m, 3H), 4.84 (q, 1H). ^{13}C-NMR (500 MHz, $CDCl_3$) δ -5.47, 18.45, 25.79, 28.83, 29.02, 75.37, 171.65, 177.15 -IR (cm^{-1}, thin film from $CHCl_3$): 1255 (Si-CH_3), 1716 (C=O, acid), 1742 (C=O, ester). ESI-MS m/z: 421.2 $[M+1]^+$

1,3-di-TBDMS glycerol PEG succinate (**3G**): Yield: 78% (white solid) ^{1}H-NMR (500 MHz, $CDCl_3$): δ 0.02 (s, 12H), 0.84 (s, 18H), 2.60 (m, 4H), 3.41-3.76 (m, ~450H), 4.19 (t, 2H), 4.84 (q, 1H). Mw= 5.1 kDa, PDI= 1.1

Glycerol PEG succinate (**4G**): Yield: 91% (white solid) ^{1}H-NMR (500 MHz, $CDCl_3$): δ 2.60 (m, 4H), 3.41-3.76 (m, ~450H), 4.23 (m, 3H). Mw= 5.0 kDa, PDI= 1.1

G18P5-S (**5G-S, G18P5-S**): Yield: 78% (white solid) ^{1}H-NMR (500 MHz, $CDCl_3$): δ 0.88 (t, 6H), 1.27 (m, 52H), 1.61 (m, 4H), 2.30 (t, 4H), 2.65 m (4H), 3.38-3.87 (m, ~450H), 4.25 (m, 6H), 5.26 (m, 1H). Mw= 6.4 kDa, PDI= 1.0

G18P5-O (**5G-O, G18P5-O**): Yield: 74% (white solid) ^{1}H-NMR (500 MHz, $CDCl_3$): δ 0.86 (t, 6H), 1.27 (m, 40H), 1.59 (m, 4H), 1.99 (m, 8H), 2.29 (q, 4H), 2.63 (m, 4H), 3.46-3.80 (m, ~450H), 4.14 (m, 2H), 4.23 (m, 2H), 4.27 (m, 2H), 5.25 (m, 1H), 5.32 (m, 4H) Mw= 6.7 kDa , PDI= 1.2

G18P5-L (**5G-L, G18P5-L**): Yield: 81% (white waxy solid) ^{1}H-NMR (500 MHz, $CDCl_3$): δ 0.88 (t, 6H), 1.29 (m, 28H), 1.58 (m, 4H), 2.03 (8H), 2.64 (4H), 2.75 (4H), 3.36-3.77 (m, ~450 H), 4.14 (2H), 4.23 (m, 2H), 4.28 (m, 2H), 5.25 (m, 1H), 5.33 (m, 6H) Mw= 6.5 kDa, PDI= 1.2

3.4.3.2. T series of AMs

AMs based on a tartrate backbone were synthesized according to **Figure 3.3B.** 2,3-O-isopropylidene tartrate, **1T** was conjugated to mPEG-OH via carbodiimide coupling. Briefly, a solution of **1T** (2.0 eq., 0.28 mmol) and DPTS (1.1 eq., 0.16 mmol) in 5.0 mL of anhydrous DCM was added to a solution of mPEG-OH (1.0 eq., 0.14 mmol) in 5.0 mL of anhydrous DCM. DCC (1 M, 2.0 eq., 0.28 mmol) was added and the reaction stirred for 24 h under nitrogen. The urea byproduct was removed via filtration, and the filtrate washed with 1 N HCl (2X, 10 mL) and brine (1X, 10 mL) and dried over $MgSO_4$. Following concentration on a rotary evaporator, crude **2T** was precipitated in diethyl ether (15 mL) and collected via centrifugation (3500 rpm, 5 min each). The product was washed (5X, 15 mL) with diethyl ether to obtain pure **2T**.

The free acid was methyl-protected using carbodiimide coupling. To a solution of **2T** (1.0 eq., 0.090 mmol) in 5 mL DCM, DMAP (2.5 eq., 0.24 mmol) was added and allowed to stir for 10 min. Methanol (2.5 eq., 0.24 mmol) and EDCI (2.5 eq. 0.24 mmol) were added sequentially to the reaction flask and allowed to stir overnight. The crude mixture was washed with 10% potassium

bisulfite (2X, 10 mL) and brine (1X, 10 mL), dried over $MgSO_4$, and concentrated *in vacuo*. **3T** was precipitated in diethyl ether (15 mL) and isolated via centrifugation (4500 rpm, 5 min). The product was washed with diethyl ether (3X, 15 mL) to remove impurities.

The acetonide protecting group was removed from **3T** with trifluoroacetic acid (TFA) using water as a catalyst. **3T** (0.010 mmol) was dissolved in a solution of TFA (25%, 2.5 mL), chloroform (74%, 7.4 mL), and water (1%, 0.1 mL) and stirred for 4 h at room temperature. The reaction was concentrated *in vacuo* to remove TFA and chloroform and resuspended in DCM (5 mL). The crude product was washed with deionized water (1X, 5 mL), and brine (1X, 5 mL), dried over $MgSO_4$, and the product concentrated in *vacuo*. **4T** was precipitated in diethyl ether (15 mL) and centrifuged (4500 rpm, 5 min) to obtain pure **4T**.

Alkyl acid arms were conjugated to free alcohols of **4T** via carbodiimide coupling. Oleic acid conjugation to **4T** is given as an example. Oleic acid (2.2 eq., 0.090 mmol) and DMAP (2.2 eq., 0.090 mmol) were dissolved in 5 mL anhydrous DCM under nitrogen. **4T** (1.0 eq., 0.040 mmol) and EDCI (4.2 eq., 0.16 mmol) were added, and the reaction stirred overnight at room temperature. The mixture was washed with 10 % potassium bisulfite (2X, 15 mL) and brine (1X, 15 mL), dried over $MgSO_4$, and concentrated *in vacuo*. **5T** was purified as previously described earlier for PEGylated compounds.

2,3-O-isopropylidene tartrate PEG (**2T**) Yield: 77% (white solid) ^{1}H-NMR (500 MHz, $CDCl_3$): δ 1.51 (s, 6H), 3.33-3.79 (m, ~450H), 4.24 (m, 1H), 4.49 (m, 1H), 4.71 (dd, 2H). Mw= 5.2 kDa, PDI= 1.0

1-methylester-2,3-O-isopropylidene tartrate PEG (**3T**) Yield: 71% (white solid) ^{1}H-NMR (500 MHz, $CDCl_3$): δ 1.48 (s, 6H), 3.33-3.79 (m, ~450H), 3.81 (s, 3H), 4.35 (m, 2H), 4.80 (s, 2H). Mw= 5.0 kDa, PDI= 1.0

1-methylester-tartrate PEG (**4T**) Yield: 89% (white solid) ^{1}H-NMR (500 MHz, $CDCl_3$): δ 3.38-3.79 (m, ~450H), 3.83 (s, 3H), 4.37 (dm, 2H), 4.75 (s, 2H). Mw= 4.9 kDa, PDI= 1.1

T18P5-S (**5T-S**): Yield: 75% (white solid) ^{1}H-NMR (500 MHz, $CDCl_3$): δ 0.88 (t, 6H), 1.23 (m, 56H), 1.60 (m, 4H), 2.38 (m, 4H), 3.42-3.80 (m, ~450H), 3.73 (s, 3H), 4.27 (m, 2H), 5.68 (m, 2H). Mw= 6.2 kDa, PDI= 1.1

T18P5-O (**5T-O**): Yield: 73% (white solid) ^{1}H-NMR (500 MHz, $CDCl_3$): δ 0.86 (t, 6H), 1.25 (m, 56H), 1.71 (m, 4H), 2.38 (m, 4H), 3.42-3.80 (m, ~450H), 3.73 (s, 3H), 4.27 (m, 2H), 5.68 (m, 2H). Mw= 6.6 kDa, PDI= 1.1

T18P5-L (**5T-L**): Yield: 73% (white solid) ^{1}H-NMR (500 MHz, $CDCl_3$): δ 0.86 (t, 6H), 1.25 (m, 56H), 1.71 (m, 4H), 2.38 (m, 4H), 3.42-3.80 (m, ~450H), 3.73 (s, 3H), 4.27 (m, 2H), 5.68 (m, 2H). Mw= 6.1 kDa, PDI= 1.1

3.4.4. Liposome Preparation

Large unilamellar vesicles (LUVs) were prepared via the thin film hydration and extrusion method. Briefly, DSPC (25 mg/mL) and AM solutions in chloroform (28.5 mg/mL) were mixed in 20 mL scintillation vials at the desired concentration (2, 4, 6 mol% AM or PEG-lipid) and concentrated in *vacuo*. Thin films were further dried in a vacuum dessicator overnight, followed by hydration in HEPES buffer (10 mM, pH 7.4) or sodium citrate buffer (200 mM, pH 4.0) for 1 h at 65 °C with gentle agitation. Hydrated films were subjected to five freeze-thaw cycles by heating at 65 °C in a water bath and freezing in dry ice at -78 °C for 15 min each. Multilamellar vesicle sizes were first decreased by extrusion 5 times through a 200 nm polycarbonate membrane prior to generating LUVs by extrusion 11 times through a 100 nm polycarbonate membrane at 65 °C with an Avanti Mini-Extruder.

3.4.5. Liposome Physicochemical Characterization

LUV sizes and zeta (ζ) potential were characterized via dynamic light scattering (DLS) on a Malvern-Zetasizer Nano Series (ZS90) with a 90° scattering angle. Hydrodynamic diameter and PDI were evaluated in HEPES buffer by measuring the Z-average in triplicate. Samples were extensively dialyzed against deionized water prior to ζ potential measurements.

LUVs were visualized via transmission electron microscopy (TEM) with contrast. The liposome suspension (10 µL, 0.1 mg/mL) was placed on a carbon film-coated copper grid and allowed to absorb for 30 s before the excess solution was wicked away. Uranyl acetate solution (10 µL, 1.0 %) was applied and absorbed for 30 s before wicking away excess solution with filter paper. The grid was then air dried overnight in a desiccator. Images were obtained on a JEOL 1200EX electron microscope (JEOL USA) with a AMT-XR41 digital camera.

3.4.6. Liposome Stability Characterization

The colloidal stabilities of LUV formulations were assessed via dynamic light scattering (DLS). Samples were prepared at 10 mg DSPC/mL at the desired AM or PEG-lipid concentration in HEPES buffer. The hydrodynamic diameter was monitored at predetermined time points under storage conditions (room temperature, 4 weeks) and physiological conditions (37 °C, gentle agitation, 7 days).

3.4.7. Hydrophilic Dye Release

Hydrophilic dye release was evaluated via fluorimetry by monitoring release of sulforhodamine B (SRB). SRB was encapsulated using a pH gradient by first generating LUVs (10 mg DSPC/mL) in sodium citrate buffer [41]. LUVs were dialyzed overnight into HEPES buffer then incubated with an equal volume of SRB in HEPES buffer (35 mg/mL) at 65 °C for 1 h with gentle agitation. Unencapsulated SRB was removed via size exclusion chromatography packed with Sephadex G50 Fine resin (2 g/mL liposome suspension) using HEPES buffer as the eluent.

Dye release was monitored via fluorescence spectroscopy at 37 °C on a RF-5301PC spectrofluorimeter (Shimadzu Scientific Instruments, Columbia, MD). At predetermined time points, 80 µL aliquots of LUV suspensions were withdrawn and diluted with 820 µL of HEPES buffer. Fluorescence emission spectra were obtained from 530-630 nm with an excitation wavelength of 565 nm, and the fluorescence at 581 nm was recorded in triplicate. At end of experiment, 20 µL of 5% Triton X was added to samples to fully release dye from the LUV suspensions. Data shown (**Figure 3.12**) is cumulative percentage over the specific time period shown, as the remaining SRB is recovered later.

3.4.8. Coarse-Grained Modeling

[Course-grained modeling and molecular dynamics simulations were performed by Bin Zhang, Department of Chemical Engineering, Rutgers University, Piscataway, NJ]

Molecular Dynamics (MD) simulation technique was used to assess the DSPC/AM system using the open source community-based MD simulation package Large-scale Atomic/Molecular Massively Parallel Simulator (LAMMPS) [42]. An implicit solvent Coarse-Grained (CG) model was used to increase the resolution of spatiotemporal scales. Dry MARTINI CG implicit solvent model, adopting a mapping of 4 heavy atoms to one CG bead, was used to model DSPC and AMs.

All molecules were modeled by mapping distinct bead types that represent different levels of polarity and hydrogen bond capacities. Non-bonded interactions between the different bead types, including van der Waals and electrostatic interactions, were modeled by the 12-6 Lennard-Jones (LJ) potential and Coulombic forces, respectively. For LJ potentials applied to all beads, with the exception of PEG beads, the LJ potential is shifted to 0 from 0.9 to 1.2 nm, with an inner cut-off of 9 Å and an outer cut-off of 12 Å. The beads are differentiated into four main types: polar (P), nonpolar (N), apolar (C) and charged (Q). Each type was further divided into subtypes using letters to define the hydrogen-bonding capabilities (d for donor, a for acceptor, da for both, and 0 for

neither) or Roman numerals indicating the degree of polarity (I indicating low polarity to V indicating high polarity).

DSPC was represented by fourteen CG beads, including one positively charged hydrophilic bead (Q0), one negatively charged hydrophilic bead (Qa), two nonpolar beads (Na) and ten hydrophobic beads (C1), as defined by **Table 3.1**. Stearate hydrophobic arms were coarse-grained into four nonpolar head beads (Na) and ten tail beads (C1). Oleate arms were coarse-grained into four nonpolar head beads (Na), eight tail beads (C1), and two unsaturated tail beads (C3). Linoleate arms were coarse-grained into four nonpolar head beads (Na), six tail beads (C1), and four unsaturated tail beads (C3). The PEG chain model was based upon earlier studies, and PEG components were coarse-grained into 110 beads (SNda) [43-45]. Each coarse-grained PEG bead has a mass of 45 amu (compared to 72 amu for all other beads). Non-bonded pair interactions between PEG and all other bead types was captured by the repulsive Weeks-Chandler-Anderson (WCA) potential. The PEG chain model has been validated by comparison of the radius of gyration with earlier studies [46, 47]. **Table 3.1** summarizes the LJ pair potentials for the different types of potentials.

Table 3.1: Tabulated parameters for nonbonded (Lennard-Jones) potentials for each bead type

	interaction potential	
LJ	**σ (nm)**	**ε (kJ/mol)**
Qa-Qa	0.60	2.0
Qa-Na	0.47	0.5
Qa-C1	0.62	2.0
Qa-C3	0.47	0.5
Qa-Snda	0.47	0.5
Qa-Qo	0.60	2.0
Na-Na	0.47	2.3
Na-C1	0.47	2.7
Na-C3	0.47	2.7
Na-Snda	0.47	2.7
Na-Qo	0.47	0.5
C1-C1	0.47	4.5
C1-C3	0.47	4.5
C1-Snda	0.47	2.7
C1-Qo	0.62	2.0
C3-C3	0.47	4.5
C3-Snda	0.47	2.7
C3-Qo	0.47	0.5
SNda-SNda	0.43	2.0
SNda-Qo	0.47	0.5
Qo-Qo	0.60	2.0

All molecules are represented by bead-spring models, as shown in **Figure 3.13**. The bond potential between two consecutively bonded beads is captured by the harmonic potential, and the three-body angle potential is captured by the cosine harmonic potential [44]. The dihedral potential is given by the following equation:

$$V_{dihedral}(\varphi) = \Sigma K_{\varphi,i}(1 + \cos(n_i\varphi - \varphi_i))$$

where n_i and φ_i are the multiplicities and offsets, respectively, of the 4 individual dihedral terms, and K_φ is the dihedral constant [46].

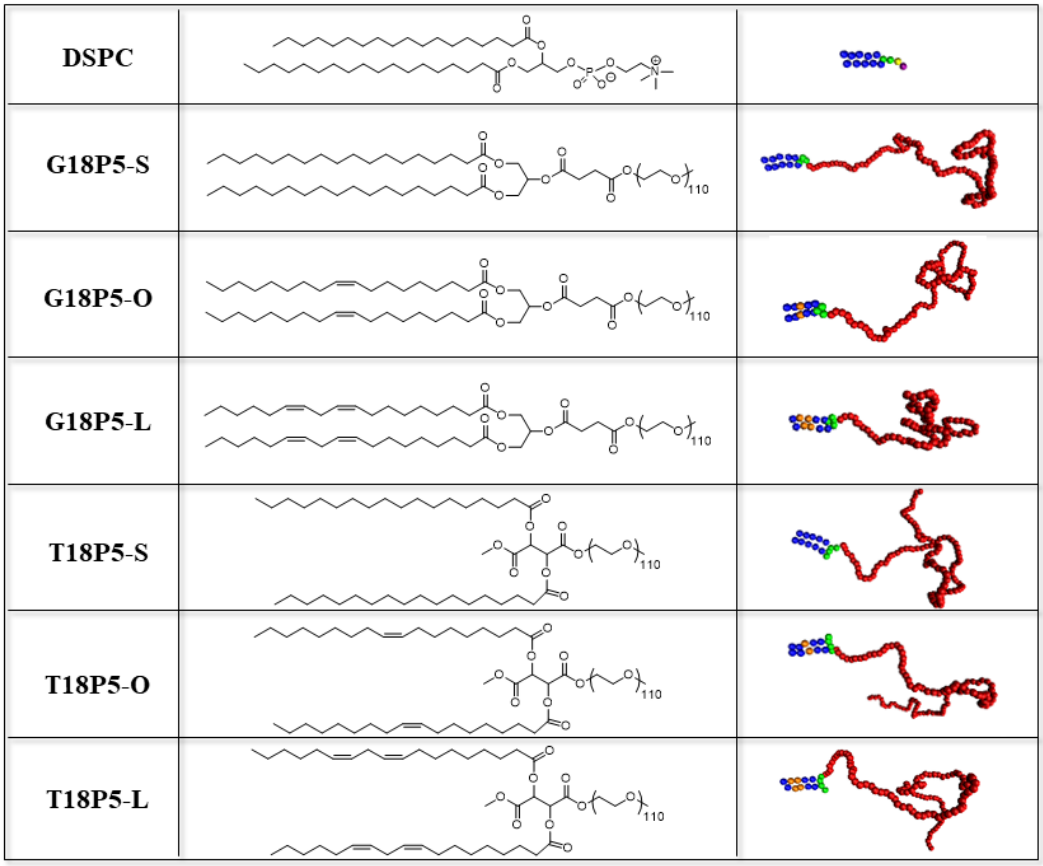

Figure 3.13: Chemical structures and corresponding CG bead-spring model snapshots of DSPC and AMs. Bead colors are as follows: red- PEG, green-AM backbone, blue- saturated hydrocarbon, orange- unsaturated hydrocarbon, yellow- phosphate, purple- quaternary amine

Prior to running simulations, a preassembled DSPC bilayer with 984 lipid molecules and one type of AM embedded in the bilayer at a fixed concentration (2 mol%, 4 mol% or 6 mol%) was generated. The bilayer was placed in a 15.7 nm x 15.7 nm x 80 nm simulation box with three-dimensional periodic boundary conditions. The system was initially run in the canonical ensemble (310 K, 1 Bar) for at least 50 ns to obtain a tensionless bilayer. The system was run for at least an additional 50 ns using the canonical ensemble with a constant volume to reach equilibrium. After the equilibration phase, the system was run for a further 6 ns to perform the desired measurements.

3.4.9. PEG measurements

[PEG measurements were performed by Bin Zhang, Department of Chemical Engineering, Rutgers University, Piscataway, NJ]

The thickness of each PEG chain was calculated by determining the difference between the maximum and minimum values of the z-coordinate of the beads encompassing each chain. The thickness of the PEG corona was then calculated by averaging the thickness of all PEG chains in a single monolayer.

The upper half of simulation box was divided into 160 5 Å thick slabs in the z axis to understand the changes in PEG density with increasing distance from the bilayer. The probability of PEG beads in each slab was calculated over 6 ns, and the results were normalized by the total number of PEG beads in the upper half of the simulation box for each series and concentration of AM.

3.5 Appendix for Chapter 2

3.5.1. Introduction

Previous generations of AMs have been incorporated into cationic liposomes comprised of 1,2-dioleoyl-sn-glycero-3-phosphoethanolamine (DOPE) and 1,2-dioleoyl-3-

trimethylammonium-propane (DOTAP) at varying weight percentages (**Figure 3.14**). Interestingly, the lipid complexes were preferentially internalized by cancer cells compared to human fibroblasts [48]. As such, liposome formulations with DOPE and DOTAP combined with unsaturated AMs may be a promising vehicle for delivery to cancerous tumor cells, where sustained delivery would provide additional benefits over previous formulations. As such, AMs with varying degrees of unsaturation were formulated with into cationic liposomes, and the resulting formulation stability and cytotoxicity were evaluated.

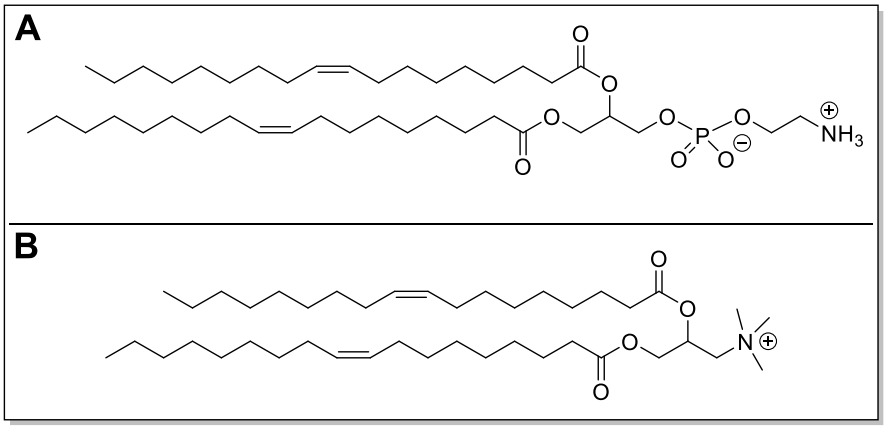

Figure 3.14: Chemical structures of bulk DOPE/DOTAP lipid system. (A) cationic lipid DOTAP, and (B) neutral helper lipid DOPE

3.5.2. Results and Discussion

Stability of cationic liposomes were evaluated at physiological conditions. Incorporation of AMs increased liposome sizes due to increased diameter of the exterior PEG shell (**Figure 3.15A**). Incorporation at 2 mol% yielded similar sizes regardless of unsaturation. Higher mol % incorporation resulted in liposome sizes dependent on unsaturation, with higher degrees of unsaturation correlating to smaller sizes. These results are consistent with melting temperatures, and thus fluidity, of fatty acids that were incorporated in AM structures. All formulations also demonstrated pH size dependence (**Figure 3.15B**), being larger at acidic pH due to an increase in

protonated amine content and increased electrostatic repulsion. Formulations containing AMs demonstrated larger size increases upon exposure to acidic pH as compared to DOPE/DOTAP alone. These data indicate that the incorporation of AMs promotes destabilization at acidic pH which is common at tumor sites and in the intracellular fluid of endosomes, and has the potential to enhance tumor delivery and endosomal escape properties [49, 50].

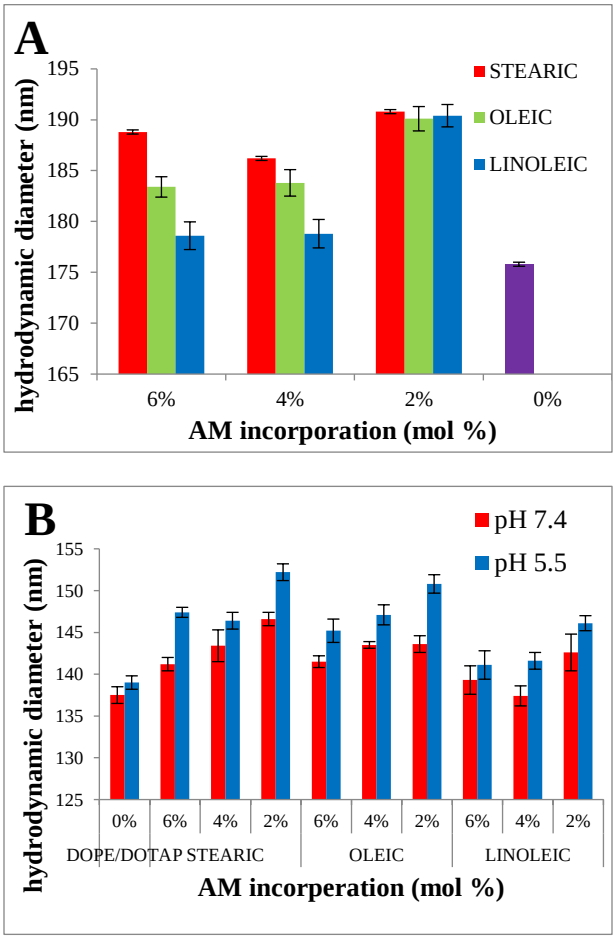

Figure 3.15: Influence of AMs on DOPE/DOTAP size characteristics as measured by DLS. AM identity (A) and pH dependent (B) sizes of liposomal formulations at 37 °C immediately after preparation. Error bars indicate standard deviation of technical triplicate

None of the treatments were toxic at the tested concentrations, including DOPE/DOTAP control (**Figure 3.16**). AM incorporation did not influence cell viability at concentrations tested.

Results demonstrate the quantity of AMs added to liposome preparations does not adversely affect cell viability, and lipid concentrations up to 10^{-5} M can be utilized for future *in vitro* experiments.

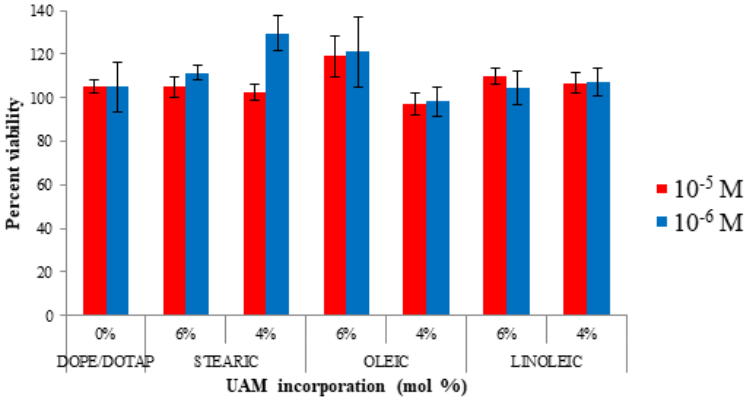

Figure 3.16: Cell viability upon treatment with AM-DOPE/DOTAP liposomes. Error bars represent standard deviation of technical quadruplicate

3.5.3. Experimental

3.5.3.1. LUV preparation

AM-DOPE/DOTAP lipid formulations were prepared following a previously reported procedure with modification [51]. Briefly, DOPE and DOTAP were co-dissolved in chloroform at a 1/1 (w/w) ratio with AM incorporation at 0, 2, 4, and 6 mol %. Chloroform was removed *in vacuo* and resulting films were rehydrated in (3-(N-morpholino)propanesulfonic acid) (MOPS) buffer, pH 7.4 or 2-(N-morpholino)ethanesulfonic acid (MES) buffer, pH 5.5 at room temperature for 24 h. Suspensions were extruded 21 times through a 100 nm pore size filter to generate unilamellar AM-DOPE/DOTAP liposomes.

3.5.3.2. Stability Characterization

Samples were diluted to 10^{-4} M prior to the start of experiments. Samples in pH 7.4 buffer were incubated at 25 °C to assess storage stability for one week, and 37 °C at pH 7.4 and pH 5.5 for 72 h to mimic circulation and endosomal conditions respectively. Sizes of AM-DOPE/DOTAP liposomes were monitored using dynamic light scattering (DLS), at 0, 1, 3 and 7 days for storage conditions and 0, 24, 48, and 72 h for biological conditions. Measurements were made in triplicate with 20 measurements per analysis.

3.5.3.3. Cytotoxicity of AM-DOPE/DOTAP Liposomes

AMs' impact on cell viability was assessed in 3T3 mouse embryonic fibroblast cells. Cells were plated in a 96 well microtiter plate at a density of 5,000 cells/well in Dulbecco's Modified Eagle Medium (DMEM) supplemented with 10% FBS and 1% penicillin/streptomycin. Cell viability was assessed using an MTS assay following suggested manufacturer protocol [52]. Cells were treated with AM-DOPE/DOTAP liposomes, 4 or 6 mol% at 10^{-5} and 10^{-6} M in quadruplicate, for 24 h. 2 mol% samples were not tested, as they demonstrated significant instability in previous experiments. Results were normalized to buffer treated controls.

3.6. References

[1] Sercombe L, Veerati T, Moheimani F, Wu SY, Sood AK, Hua S. Advances and Challenges of Liposome Assisted Drug Delivery. Frontiers in Pharmacology. 2015;6:286.

[2] Mishra J, Dey A, Singh N, Somvanshi R, Singh S. Evaluation of toxicity & therapeutic efficacy of a new liposomal formulation of amphotericin B in a mouse model. The Indian Journal of Medical Research. 2013;137:767-76.

[3] Gershkovich P, Wasan KM, Barta CA. A review of the application of lipid-based systems in systemic, dermal/ transdermal, and ocular drug delivery. Critical reviews in therapeutic drug carrier systems. 2008;25:545-84.

[4] Feeney OM, Williams HD, Pouton CW, Porter CJ. 'Stealth' lipid-based formulations: poly(ethylene glycol)-mediated digestion inhibition improves oral bioavailability of a model poorly water soluble drug. Journal of controlled release : official journal of the Controlled Release Society. 2014;192:219-27.

[5] Chang H-I, Yeh M-K. Clinical development of liposome-based drugs: formulation, characterization, and therapeutic efficacy. International Journal of Nanomedicine. 2012;7:49-60.

[6] Kraft JC, Freeling JP, Wang Z, Ho RJY. Emerging Research and Clinical Development Trends of Liposome and Lipid Nanoparticle Drug Delivery Systems. Journal of Pharmaceutical Sciences. 2014;103:29-52.

[7] Gabizon A, Shmeeda H, Barenholz Y. Pharmacokinetics of Pegylated Liposomal Doxorubicin. Clinical Pharmacokinetics. 2003;42:419-36.

[8] Moghimi SM, Szebeni J. Stealth liposomes and long circulating nanoparticles: critical issues in pharmacokinetics, opsonization and protein-binding properties. Progress in Lipid Research. 2003;42:463-78.

[9] Zhao XB, Muthusamy N, Byrd JC, Lee RJ. Cholesterol as a bilayer anchor for PEGylation and targeting ligand in folate-receptor-targeted liposomes. Journal of Pharmaceutical Sciences. 2007;96:2424-35.

[10] Needham D, Anyarambhatla G, Kong G, Dewhirst MW. A new temperature-sensitive liposome for use with mild hyperthermia: characterization and testing in a human tumor xenograft model. Cancer research. 2000;60:1197-201.

[11] Karanth H, Murthy RS. pH-sensitive liposomes--principle and application in cancer therapy. The Journal of pharmacy and pharmacology. 2007;59:469-83.

[12] Nag OK, Awasthi V. Surface Engineering of Liposomes for Stealth Behavior. Pharmaceutics. 2013;5:542-69.

[13] Immordino ML, Dosio F, Cattel L. Stealth liposomes: review of the basic science, rationale, and clinical applications, existing and potential. International Journal of Nanomedicine. 2006;1:297-315.

[14] Sriwongsitanont S, Ueno M. Physicochemical properties of PEG-grafted liposomes. Chemical & pharmaceutical bulletin. 2002;50:1238-44.

[15] Allen C, Dos Santos N, Gallagher R, Chiu G, Shu Y, Li W, et al. Controlling the physical behavior and biological performance of liposome formulations through use of surface grafted poly (ethylene glycol). Bioscience reports. 2002;22:225-50.

[16] Heyes J, Hall K, Tailor V, Lenz R, MacLachlan I. Synthesis and characterization of novel poly(ethylene glycol)-lipid conjugates suitable for use in drug delivery. Journal of Controlled Release. 2006;112:280-90.

[17] Nag OK, Yadav VR, Hedrick A, Awasthi V. Post-modification of preformed liposomes with novel non-phospholipid poly(ethylene glycol)-conjugated hexadecylcarbamoylmethyl hexadecanoic acid for enhanced circulation persistence in vivo. International journal of pharmaceutics. 2013;446:119-29.

[18] Sevanian A, Wratten ML, McLeod LL, Kim E. Lipid peroxidation and phospholipase A2 activity in liposomes composed of unsaturated phospholipids: a structural basis for enzyme activation. Biochimica et Biophysica Acta (BBA) - Lipids and Lipid Metabolism. 1988;961:316-27.

[19] Momekova D, Momekov G, Rangelov S, Storm G, Lambov N. Physicochemical and biopharmaceutical characterization of dipalmitoyl phosphatidylcholine liposomes sterically stabilized by copolymers bearing short blocks of lipid-mimetic units. Soft Matter. 2010;6:591-601.

[20] Senior J, Gregoriadis G. Is half-life of circulating liposomes determined by changes in their permeability? FEBS Letters. 1982;145:109-14.

[21] McElhaney RN. The use of differential scanning calorimetry and differential thermal analysis in studies of model and biological membranes. Chemistry and physics of lipids. 1982;30:229-59.

[22] Li J, Wang X, Zhang T, Wang C, Huang Z, Luo X, et al. A review on phospholipids and their main applications in drug delivery systems. Asian Journal of Pharmaceutical Sciences. 2015;10:81-98.

[23] Betageri GV, Parsons DL. Drug encapsulation and release from multilamellar and unilamellar liposomes. International Journal of Pharmaceutics. 1992;81:235-41.

[24] Deepthi V, Kavitha A. Liposomal drug delivery system-A review. Rguhs J Pharm Sci. 2014;4:47-56.

[25] Paavola A, Kilpelainen I, Yliruusi J, Rosenberg P. Controlled release injectable liposomal gel of ibuprofen for epidural analgesia. Int J Pharm. 2000;199:85-93.

[26] Glavas-Dodov M, Goracinova K, Mladenovska K, Fredro-Kumbaradzi E. Release profile of lidocaine HCl from topical liposomal gel formulation. International Journal of Pharmaceutics. 2002;242:381-4.

[27] Mourtas S, Fotopoulou S, Duraj S, Sfika V, Tsakiroglou C, Antimisiaris SG. Liposomal drugs dispersed in hydrogels: Effect of liposome, drug and gel properties on drug release kinetics. Colloids and Surfaces B: Biointerfaces. 2007;55:212-21.

[28] Angst MS, Drover DR. Pharmacology of drugs formulated with DepoFoam: a sustained release drug delivery system for parenteral administration using multivesicular liposome technology. Clin Pharmacokinet. 2006;45:1153-76.

[29] Chahar P, Cummings KC. Liposomal bupivacaine: a review of a new bupivacaine formulation. Journal of Pain Research. 2012;5:257-64.

[30] Mantripragada S. A lipid based depot (DepoFoam® technology) for sustained release drug delivery. Progress in Lipid Research. 2002;41:392-406.

[31] Tao L, Faig A, Uhrich KE. Liposomal stabilization using a sugar-based, PEGylated amphiphilic macromolecule. Journal of Colloid and Interface Science. 2014;431:112-6.

[32] Tian L, Yam L, Zhou N, Tat H, Uhrich KE. Amphiphilic Scorpion-like Macromolecules: Design, Synthesis, and Characterization. Macromolecules. 2004;37:538-43.

[33] Anderson M, Omri A. The effect of different lipid components on the in vitro stability and release kinetics of liposome formulations. Drug delivery. 2004;11:33-9.

[34] Blume G, Cevc G. Molecular mechanism of the lipid vesicle longevity in vivo. Biochimica et biophysica acta. 1993;1146:157-68.

[35] Johnsson M, Edwards K. Liposomes, Disks, and Spherical Micelles: Aggregate Structure in Mixtures of Gel Phase Phosphatidylcholines and Poly(Ethylene Glycol)-Phospholipids. Biophysical Journal. 2003;85:3839-47.

[36] Olson F, Hunt CA, Szoka FC, Vail WJ, Papahadjopoulos D. Preparation of liposomes of defined size distribution by extrusion through polycarbonate membranes. Biochimica et Biophysica Acta (BBA) - Biomembranes. 1979;557:9-23.

[37] Garbès Putzel G, Schick M. Phenomenological Model and Phase Behavior of Saturated and Unsaturated Lipids and Cholesterol. Biophysical Journal. 2008;95:4756-62.

[38] Marsh D, Bartucci R, Sportelli L. Lipid membranes with grafted polymers: physicochemical aspects. Biochimica et Biophysica Acta (BBA) - Biomembranes. 2003;1615:33-59.

[39] Casida JE, Gulevich AG, Sarpong R, Bunnelle EM. S-Arachidonoyl-2-thioglycerol synthesis and use for fluorimetric and colorimetric assays of monoacylglycerol lipase. Bioorganic & medicinal chemistry. 2010;18:1942-7.

[40] Danishefsky SJ, McClure KF, Randolph JT, Ruggeri RB. A strategy for the solid-phase synthesis of oligosaccharides. Science (New York, NY). 1993;260:1307-9.

[41] Sur S, Fries AC, Kinzler KW, Zhou S, Vogelstein B. Remote loading of preencapsulated drugs into stealth liposomes. Proceedings of the National Academy of Sciences. 2014;111:2283-8.

[42] Plimpton S. Fast Parallel Algorithms for Short-Range Molecular Dynamics. Journal of Computational Physics. 1995;117:1-19.

[43] Arnarez C, Uusitalo JJ, Masman MF, Ingólfsson HI, de Jong DH, Melo MN, et al. Dry Martini, a Coarse-Grained Force Field for Lipid Membrane Simulations with Implicit Solvent. Journal of Chemical Theory and Computation. 2015;11:260-75.

[44] Wang S, Larson RG. A Coarse-Grained Implicit Solvent Model for Poly(ethylene oxide), CnEm Surfactants, and Hydrophobically End-Capped Poly(ethylene oxide) and Its Application to Micelle Self-Assembly and Phase Behavior. Macromolecules. 2015;48:7709-18.

[45] Guo Y, Pogodin S, Baulin VA. General model of phospholipid bilayers in fluid phase within the single chain mean field theory. The Journal of chemical physics. 2014;140:174903.

[46] Lee H, de Vries AH, Marrink S-J, Pastor RW. A Coarse-Grained Model for Polyethylene Oxide and Polyethylene Glycol: Conformation and Hydrodynamics. The Journal of Physical Chemistry B. 2009;113:13186-94.

[47] Devanand K, Selser JC. Asymptotic behavior and long-range interactions in aqueous solutions of poly(ethylene oxide). Macromolecules. 1991;24:5943-7.

[48] Harmon AM, Lash MH, Sparks SM, Uhrich KE. Preferential cellular uptake of amphiphilic macromolecule–lipid complexes with enhanced stability and biocompatibility. Journal of Controlled Release. 2011;153:233-9.

[49] Stubbs M, McSheehy PM, Griffiths JR, Bashford CL. Causes and consequences of tumour acidity and implications for treatment. Molecular medicine today. 2000;6:15-9.

[50] Mellman I, Fuchs R, Helenius A. Acidification of the endocytic and exocytic pathways. Annual review of biochemistry. 1986;55:663-700.

[51] Tang Y, Li Y-B, Wang B, Lin R-Y, van Dongen M, Zurcher DM, et al. Efficient in vitro siRNA delivery and Intramuscular Gene Silencing using PEG-modified PAMAM Dendrimers. Molecular Pharmaceutics. 2012;9:1812-21.

[52] Stojdl DF, Lichty B, Knowles S, Marius R, Atkins H, Sonenberg N, et al. Exploiting tumor-specific defects in the interferon pathway with a previously unknown oncolytic virus. Nature medicine. 2000;6:821-5.

4. CHAPTER 3: CATIONIC AMPHIPHILES AS ANTIMICROBIAL PEPTIDE MIMICS: FLEXIBILITY AND ARCHITECTURE INFLUENCE MEMBRANE ACTIVITY AND SPECIFICITY AGAINST BACTERIA

[This work is in preparation for publication under the title "Flexibility and architecture of cationic amphiphiles designed to mimic antimicrobial peptides influence membrane activity and specificity against Gram-positive and Gram-negative bacteria." Richard Weeks, Yeseo Han, Michael Chikindas, and Kathryn E. Uhrich are co-authors for this work.]

4.1 Introduction

The overuse of antibiotics has resulted in a rapid rise in antibiotic resistance and emergence of multidrug resistant bacteria, sparking significant global health concerns [1, 2]. While ongoing efforts are being taken to promote antimicrobial stewardship and slow the progression of resistant bacteria strains, the scientific community has also initiated a movement to understand innate immune responses to bacterial infections and develop alternatives to traditional antibiotics [1-4].

Antimicrobial peptides (AMPs) are naturally existing membrane active molecules that have gained significant attention as alternatives to traditional antibiotics [4, 5]. While the primary sequences and length of AMPs vary greatly, the vast majority contain a net cationic charge and adopt amphipathic secondary structures segregating hydrophobic and charged residues in the presence of lipid bilayers [5, 6]. Although additional molecular targets exist, most AMPs initially interact with the negatively charged components of bacterial cell membranes (e.g., phosphatidylglycerol, lipopolysaccharides, and teichoic acids) and hydrophobic residue insertion leads to membrane integrity disruption and cell death [5, 7-9]. Their unique membrane targeting mechanism results in lower resistance rates as compared to traditional antibiotics that target specific biological pathways (e.g., DNA or cell wall synthesis) or inhibit enzymatic activity or metabolic activity [1, 9-12]. However, several shortcomings limit AMPs applicability as viable antimicrobial

therapeutics. AMPs are associated with high production costs due to multiple low yielding peptide coupling reactions or expression systems, the resulting peptide bonds are susceptible to native proteases, and they commonly elicit undesirable toxicity to mammalian cells [11, 13, 14]. To address these limitations, several groups have evaluated the antibacterial potential of non-peptide derived AMP mimics. For example, peptidomimics developed with non-natural amino acid structures aid in protease susceptibility, arylamide oligomers designed de novo have been synthesized from inexpensive monomers, and Jennings et al. designed simple quaternary ammonium amphiphiles via cost effective syntheses that additionally overcome obstacles associated with polymer and oligomer folding [6, 15-18].

This work builds upon these efforts by designing small molecule cationic amphiphiles (CAms) with high potency against Gram-positive and Gram-negative bacteria [19, 20]. CAms were designed from inexpensive starting materials and possess similar physicochemical features to AMPs, namely cationic charge and amphiphilicity, while additionally being resistant to protease activity. CAm structures are based on a linear sugar backbone that serves as both a spacer to two cationic moieties as well as the branch point for two hydrophobic domains derived from fatty acids or analogous aliphatic alcohols (**Figure 4.1**). Comparable to the key features that impart AMPs with antimicrobial efficacy, CAms have net cationic charges and structural flexibility required to fold into facially amphipathic structures that may lend to selective activity against bacterial membranes.

Herein, the design, synthesis, and subsequent antimicrobial characterization of CAms with strategic structural variations (**Figure 4.1**) is reported to better understand the chemical features that contribute to antimicrobial efficacy and specificity. Molecular flexibility has been shown to strongly influence antimicrobial activity and global amphiphilicity in a variety of molecular architectures, including AMPs, small molecule amphiphiles, and polymers [21-24]. In particular, Palermo et al designed methacrylate copolymers with varying cationic linker lengths to the polymer

backbone. In doing so, they found that shorter linker lengths had desirable selectivity profiles for bacterial cells over mammalian cells, but longer cationic linker lengths resulted in polymers with non-selective membrane activity [21]. As such, two series of CAms were designed to evaluate the influence of flexibility in our molecular platform. The conformational flexibility of cationic moieties was imparted in CAm structures through step-wise increases in cationic linker lengths (i.e., two, four, or six methylene units) extending from the sugar backbone. One series of CAms with charge flexibility was designed with ester-linked hydrophobic domains and the other with added hydrophobic flexibility imparted by ether linkages to examine the combinatorial effects of overall molecular flexibility.

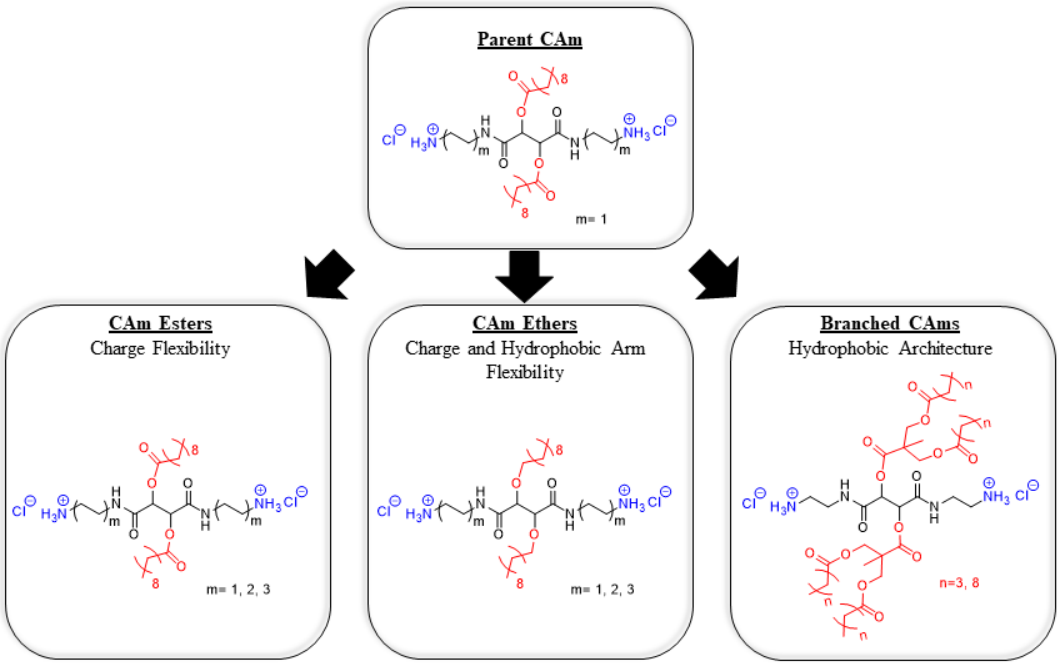

Figure 4.1: Chemical structures of three CAm series indicating nomenclature (bold underlined text) and structural variations. All CAm structures are based on Parent CAm (top) with strategic chemical changes. Charge flexibility is varied by increasing the linker length between cationic charges and the sugar backbone (left). Charge and hydrophobic arm flexibility are altered though increasing charged end-group linker lengths in addition to ether-linkages for hydrophobic arms

(center). Branched hydrophobic architecture was generated by using dendritic branch points for hydrophobic domains.

A third series of CAms was designed to probe the effect of hydrophobic domain architecture on antimicrobial efficacy and selectivity. Several studies, including those performed in the Uhrich group, have identified hydrocarbon chains lengths that elicit desirable antimicrobial selectivity profiles, frequently of intermediate lengths [19, 20, 25, 26]. However, studies evaluating the contribution of a hydrophobic architecture are needed. Lind et al. demonstrated that increased branching density and charge flexibility resulted in improved bacterial potency and specificity in antimicrobial dendrimers [27]. Similarly, Chen et. al found that higher generation dendrimers exhibited more potent antibacterial efficacy, suggesting that a branched architecture may influence membrane activity [26]. As such, CAms were additionally designed with branched hydrophobic domain architectures and varying hydrophobic chain length to assess the relative contributions of hydrophobic domain branching, hydrophilic-lipophilic balance (HLB), and alkyl chain length.

Upon successful synthesis, all compounds were screened for antimicrobial efficacy in representative Gram-positive and Gram-negative bacteria, as well as for hemolytic activity in human-derived red blood cells. In vitro membrane specificity experiments were then carried out for selected compounds, demonstrating enhanced activity against bacterial membrane mimics compared to mammalian cell membrane mimics. Together, these experiments identify several key features of CAms that contribute to antimicrobial potency and specificity.

4.2. Results and Discussion

Three series of CAms were designed to examine the influence of varying chemical characteristics on antimicrobial activity and membrane selectivity. Within each series, small changes in molecular structure were made to precisely identify their influences on the aforementioned properties via in vitro experiments.

4.2.1. Synthesis and Characterization

CAm ethers (***3***) with charged end-group flexibility were synthesized in a total of four reactions (**Figure 4.2**) from readily available and inexpensive starting materials [20]. Ether linkages were generated by alkylation of di-*tert*-butyl tartrate and quantitative deprotection of *t*-butyl groups to yield T10 ether in high yield as previously described [28]. End group conformational flexibility was achieved via carbodiimide coupling reactions of mono-Boc protected diamines with T10 ether to synthesize ***2***. The linker lengths between amines and the tartramide backbone were either two, four, or six methylene units in length, as correlations with antimicrobial efficacy and specificity have been previously identified in this range [21, 23]. Boc groups were then removed with HCl in dioxane to generate the final products (***3***) as chloride salts in quantitative yields.

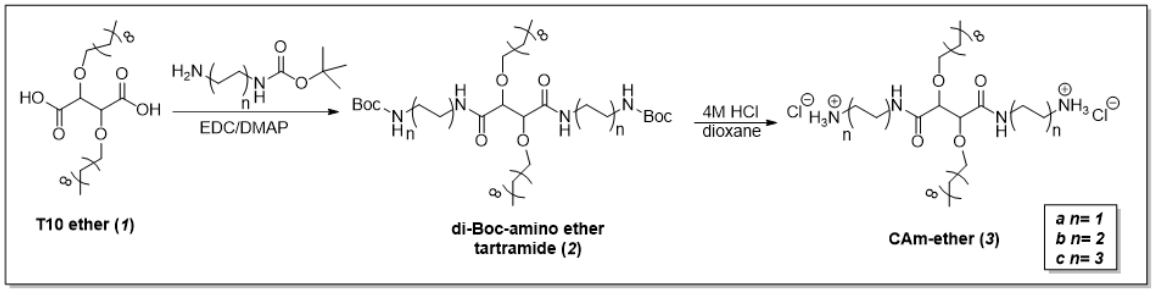

Figure 4.2. Synthetic approach used to generate CAm-ethers in two reaction steps from T10-ether.

CAm esters (***6***) with charged end-group flexibility were synthesized via an analogous approach (**Figure 4.3.)** [19]. Di-Boc-amino tartramides (***4***) were first synthesized by conjugating mono-Boc protected diamines with varying linker lengths to dimethyl tartrate via an aminolysis reaction. The intermediates were then acylated via carbodiimide coupling to generate ***5***, and the final products (***6***) generated via deprotection under acidic conditions as described earlier. This synthetic approach generates the final products in a three-step reaction sequence, each step generating high yields of products with facile isolation procedures.

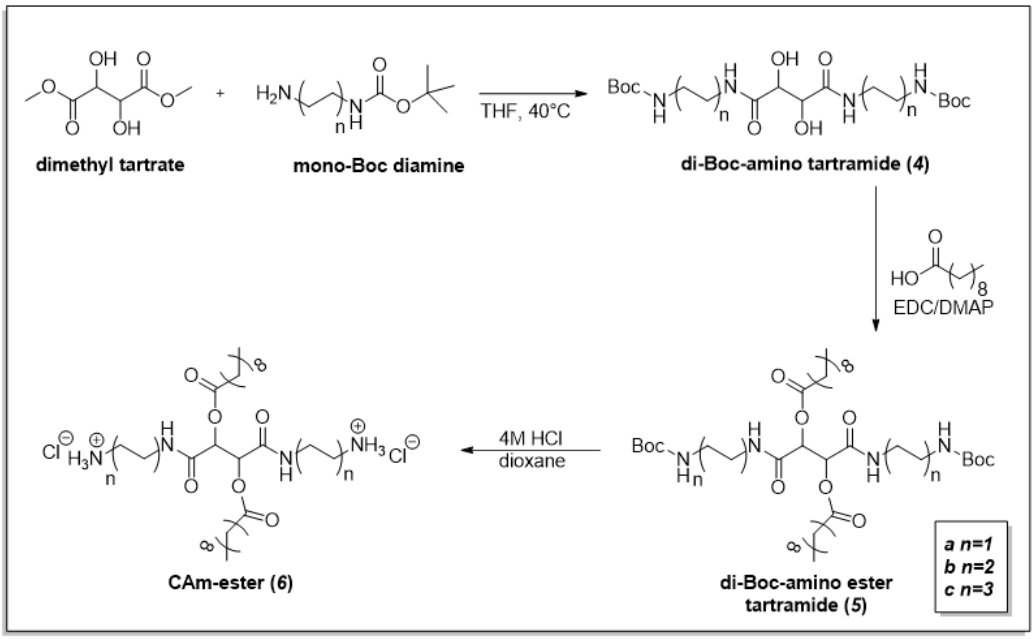

Figure 4.3. Synthetic approach used to generate CAm-esters in three reaction steps from readily available starting materials.

Branched CAms resulted from a novel synthetic approach (**Figure 4.4.**). To generate these amphiphiles, bis-MPA was utilized as a dendritic branch point for hydrophobic domains to generate ***7***. Alkyl chlorides with five or ten total carbons were used to maintain analogous HLB with CAm esters or equivalent hydrophobic chain lengths, respectively. ***7*** was conjugated to dibenzyl tartrate via carbodiimide coupling, and the benzyl groups removed via hydrogenolysis in quantitative yields. *N*-Boc-1,2-ethylenediamine was successfully conjugated to the backbone following modified literature precedence to yield ***10*** in high yield using HOBt as the catalyst and DCC as the coupling reagent [29]. Lastly, 4 M HCl in dioxane was used to deprotect Boc groups producing the branched CAms (***11***) in quantitative yields.

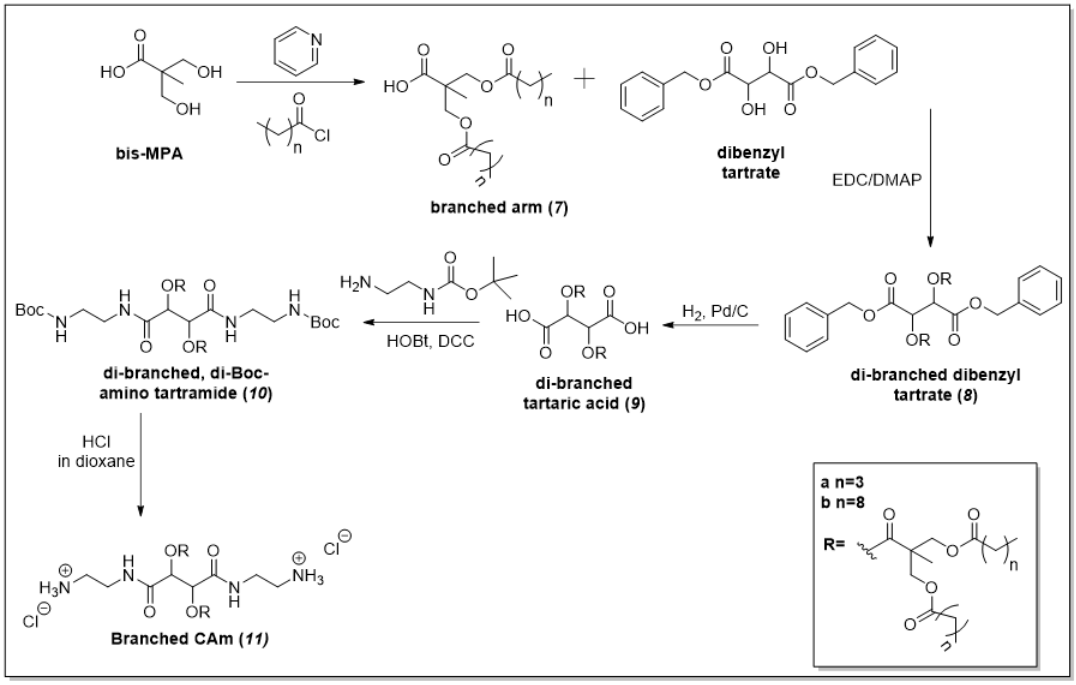

Figure 4.4. Synthetic approach used to generate branched CAms.

The syntheses used in the generation of each CAm series demonstrate improvement upon AMP synthetic protocols. In general, AMPs require a minimum of seven residues to fold into an amphipathic secondary structure [14]. To generate synthetic AMPs of this length using traditional peptide synthesis, addition of each Fmoc-protected amino acid and its subsequent deprotection is required, resulting in at least double the number of reactions steps as are amino acid residues [30-32]. In contrast, both series of CAms can be generated in five or less reactions with high product yields, significantly reducing production costs. Additionally, tartrates, fatty acids, and alkyl alcohols are inexpensive, readily available, and can be found on the list of Generally Recognized as Safe (GRAS) ingredients or are approved by the Food and Drug Administration for direct addition to food products for human consumption [33, 34]. As such, low or negligible toxicity is anticipated from degradation products.

4.2.2. Antimicrobial Activity

CAms were evaluated for antimicrobial efficacy against representative Gram-positive (i.e., *Listeria* monocytogenes) and Gram-negative (*i.e., Escherichia coli*) bacteria. Assays were carried out using the micro-broth dilution method, and the lowest concentration of CAm that resulted in no bacteria growth after 24 h was taken as the MIC. The overwhelming majority of tested CAms resulted in MICs in relevant therapeutic ranges (< 50 μg/mL) against both Gram-positive and Gram-negative bacteria (**Table 4.1**). As Gram-negative bacteria have an additional outer membrane structure (**Figure 4.5**), they are notoriously more difficult to permeabilize and eradicate [35]. This trend is reflected in our experiments, as MICs are lower against *L. monocytogenes* compared to *E. coli*. However, most CAms have MICs against Gram-negative bacteria between 15-25 μg/mL, which is comparable to or better than what is commonly reported in literature [21, 25, 27, 36, 37]. Interestingly, the 5C branched CAm (***11a***) exhibited a 2X lower MIC against *E. coli* as compared to *L. monocytogenes*, and was the lowest MIC against *E. coli* of all CAms that were evaluated. However, the corresponding 10C branched CAm (***11b***) exhibited no effect on either bacterium at the highest concentrations tested (250 μg/mL). This data reveals two critical findings regarding CAm chemical structure and activity; branched architecture better permeabilizes Gram-negative bacteria membranes than linear alkyl chains, and the relative HLB of CAms is more crucial to activity than hydrophobic arm length.

Table 4.1: Selectivity properties of CAms for Gram-positive (G+) and Gram-negative (G-) bacteria as compared to hemolytic potential in human red blood cells. Selectivity indices (SI) represent the ratio of minimum inhibitory concentration (MIC) to the concentration required to lyse 50% of red blood cells (HC50)

CAm	MIC (μg/mL)		HC50 (μg/mL)	SI (G+) (μg/mL)	SI (G-) (μg/mL)
	L. monocytogenes – (G+)	*E. coli* – (G-)			
2C-ether (3a)	5.3	21.2	18	3.4	0.8
4C-ether (3b)	4.9	19.4	23	4.7	1.2
6C-ether (3c)	6.7	35.7	13	1.9	0.4
2C-ester (6a)	3.8	20.3	50	13.1	2.5
4C-ester (6b)	3.5	18.6	53	15.1	2.8
6C-ester (6c)	4.3	68.7	28	6.5	0.4
5C-branched (11a)	31.3	15.6	98	3.1	6.2
10C-branched (11b)	>250	>250	56	<0.2	<0.2

Conformational flexibility of the cationic end-group, however, had a less pronounced influence on antimicrobial efficacy. CAms with different cationic linker lengths (i.e., ***3a-3c*** and ***6a-6c***) all had MICs < 7 μg/mL against Gram-positive bacteria (**Table 4.1**), revealing no trend that correlates activity with charge flexibility. Conversely, when the effect of cationic spacer length was evaluated in Gram-negative bacteria, MICs were similar for two (i.e., ***3a***, ***6a***) or four carbon spacers (i.e., ***6a***, ***6b***), but were 2- to 3-fold higher for CAms with six carbon spacers (i.e., ***3c***, ***6c***). This data suggests that increased charge flexibility reduces antimicrobial efficacy. It is possible that the increased flexibility of ***3c*** and ***6c*** results in electrostatic repulsion between charges, preventing simultaneous interaction with the negatively charged components of bacterial membranes. Additionally, the added effect of hydrophobic domain flexibility imparted by ether-linkages only had an influence on activity for CAms with six carbon linkers against Gram-negative bacteria. This intriguing observation may indicate that CAms membrane disrupting mechanism is

governed primarily by electrostatic interactions at shorter charged end-group linker lengths. At longer linker lengths, hydrophobic interactions may dominate and are enhanced by hydrophobic domain flexibility.

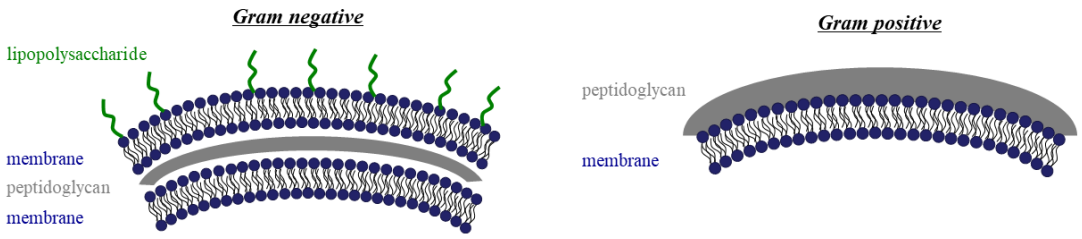

Figure 4.5: Cartoon depicting basic membrane structure of Gram-negative and Gram-positive bacteria. Gram-negative bacteria have a double membrane structure and additional lipopolysaccharide layer compared to Gram-positive bacteria. This figure was adapted from a previous Rutgers thesis [38].

4.2.3. Cytocompatibility

While it is crucial that antimicrobials exhibit efficacy at low concentrations, it is also important that they demonstrate specificity for bacteria over mammalian cell membranes. This specificity is largely accomplished through the initial electrostatic interaction between cationic moieties and the negatively charged components of the bacterial cell membranes [5, 7]. However, many AMPs and antimicrobials suffer from toxicity, which has also been correlated with high levels of hydrophobicity [39, 40]. As such, CAms hemolytic activity was evaluated in human red blood cells at different concentrations. Overall, a global trend was evident demonstrating comparably lower hemolysis for CAm esters compared to CAm ethers. These results indicate that hydrophobic arm flexibility contributes to membrane specificity, with more rigid hydrophobe conformations favoring interactions with bacterial membranes. In both series, CAms with four methylene units between the backbone and charged end group (***3b***, ***6b***) were slightly less hemolytic than CAms with longer or shorter cationic linker lengths. These results are consistent with those

obtained by Palermo et. al. demonstrating an increase in hemolytic activity in methacrylate based-copolymers with six carbon linkers between cationic moieties and the polymer backbone [21]. Interestingly, branched CAms had the lowest hemolytic activity evaluated in this study, indicating that they have lower potential to interact with mammalian cell membranes. Consistent with trends in literature, the 10C branched CAm (***11b***) had comparatively higher hemolytic activity than the 5C branched CAm (***11a***) due to increased hydrophobicity [39].

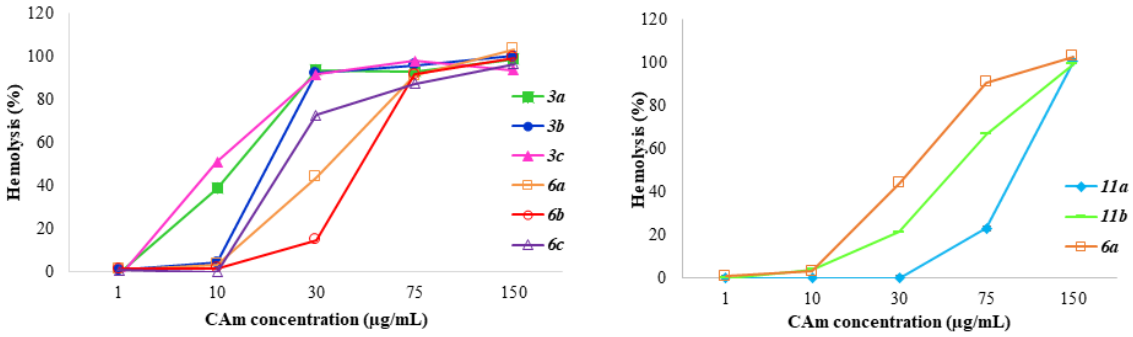

Figure 4.6. Hemolytic activity of CAms. CAm ethers and CAm esters hemolytic potential (left). CAm ethers have filled markers and CAm esters have open markers. Hemolytic activity of branched CAms is shown on the right in addition to hemolytic activity of analogous CAm ether for comparison.

As red blood cells do not have many of the cellular components and metabolic activity of normal mammalian cells, we also evaluated the CAms cytocompatibility in model mammalian cell cultures. All CAms with ester-linkages, including CAms with extended cationic linker lengths and those with branched hydrophobic domains, displayed high levels of cytocompatibility (**Figure 4.7**). As all tested concentrations resulted in 90% or greater viability, there was no observable trends correlating cationic conformational flexibility or branching architecture with cytocompatibility. However, ether-linked CAms with charged end-group flexibility revealed that longer cationic linker lengths (i.e., four or six carbons) are more cytocompatible compared to analogs with shorter

linker lengths (i.e., two carbons). Interestingly, this result is the opposite trend to antimicrobial efficacy, suggesting that restricting charge flexibility may contribute to bacterial cell selectivity.

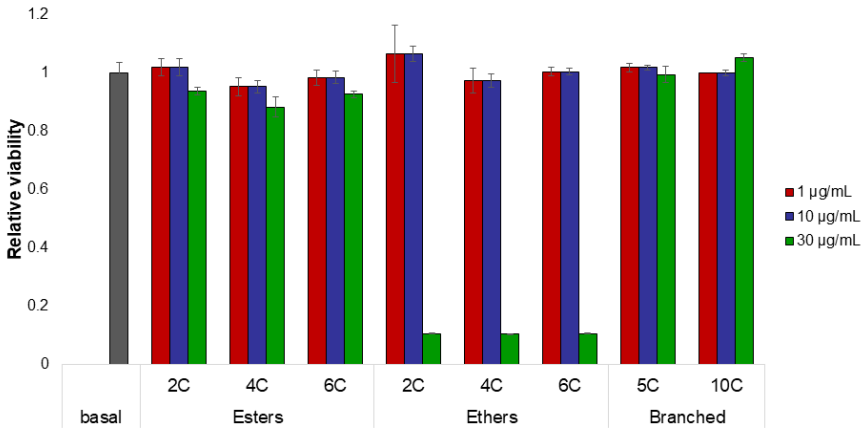

Figure 4.7. Cytocompatibility of CAms evaluated against mammalian fibroblasts

4.2.4. Selectivity

Structural features leading to CAms selectivity was evaluated by comparing their activity against bacteria to their effects on red blood cells. The selectivity index (SI) of CAms was calculated to evaluate their propensity to interact with bacterial membranes over human cells (**Table 4.1.**). SIs higher than 1.0 indicate specificity towards bacterial cell membranes, with higher specificity correlating with higher SI magnitudes. The majority of CAms had SI values greater than 1.0, with ***6a*** and ***6b*** exhibiting the highest selectivity for Gram-positive bacteria and ***11a*** having the highest activity against Gram-negative bacteria.

To corroborate these results, we performed *in vitro* experiments with LUVs mimicking the lipid contents of bacterial cells and mammalian cells. The LUVs were loaded with a self-quenching dye, calcein, and exposed to increasing CAm concentrations. Upon loss of membrane integrity, dye was released, and an increase in fluorescence was taken as an indication of membrane rupture. Calcein leakage experiments were performed for CAm ethers and esters with cationic groups two

methylene units from the backbone (i.e., ***3a*** and ***6a***). These two CAms were chosen as they have high potency against bacteria, sufficient selectivity, and the *N*-Boc-ethylenediamine is the least expensive linker, and thus the least costly CAm to synthesize for translational purposes. Results for ***3a*** are shown in **Figure 4.8.** and confirm membrane activity and specificity. Concentrations ≥ 100 μg/mL resulted in membrane lysis for bacterial membrane mimics (i.e., DOPC/DOPG), but the highest concentration evaluated, 500 μg/mL, showed < 5% lysis of membranes mimicking mammalian cells (DOPC), demonstrating specificity. The total amount of membrane lysis induced by CAms at the end of experiments clearly indicate that ***3a*** has a greater affinity for negatively charged membranes.

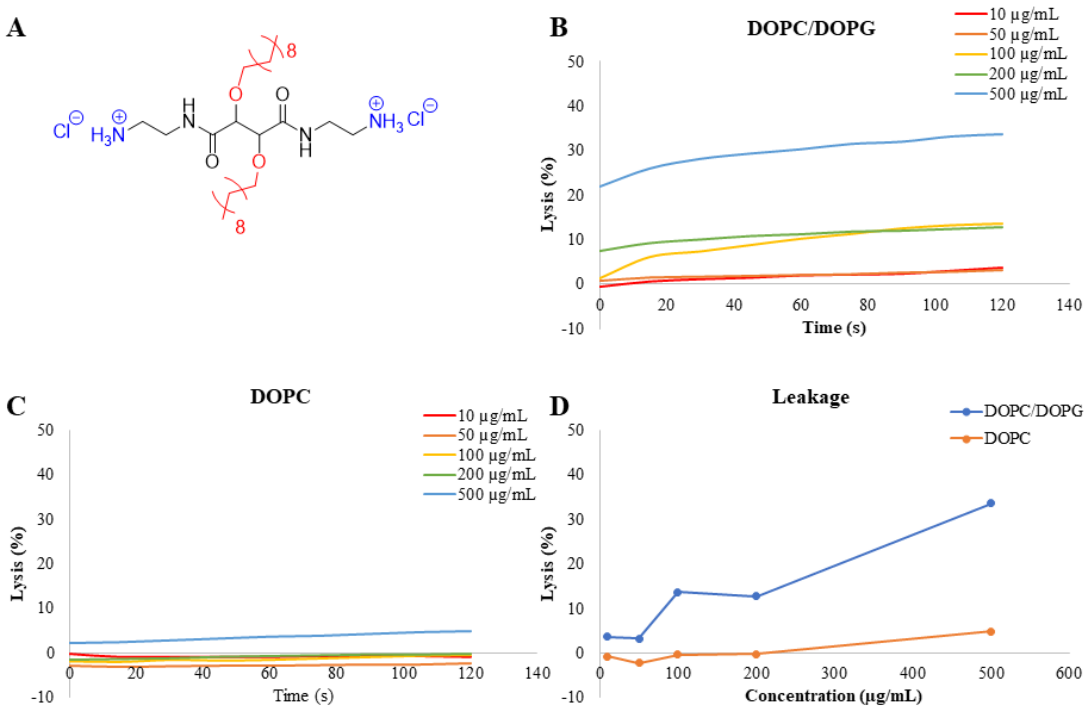

Figure 4.8. Calcein leakage experiments of CAm ethers. Leakage of dye from experiments performed with ***3a*** (A) and negatively charged membranes (B) mimicking bacterial cells and neutral membranes (C) mimicking mammalian host cell membranes indicate membrane specificity. Comparison of total dye leakage at the end of the experiment for each membrane type (D) shows influence of CAm concentration.

Similar results were obtained for ***6a*** and are shown in **Figure 4.9.** Concentrations as low at 50 µg/mL resulted in 15 % lysis of negatively charged membranes, and a direct relationship was observed between CAm concentration and total lysis. However, the highest concentration of CAm tested resulted in only 7 % lysis of zwitterionic membranes. As with ***3a*** no mammalian mimic LUV disruption was observed for concentrations below 500 µg/mL.

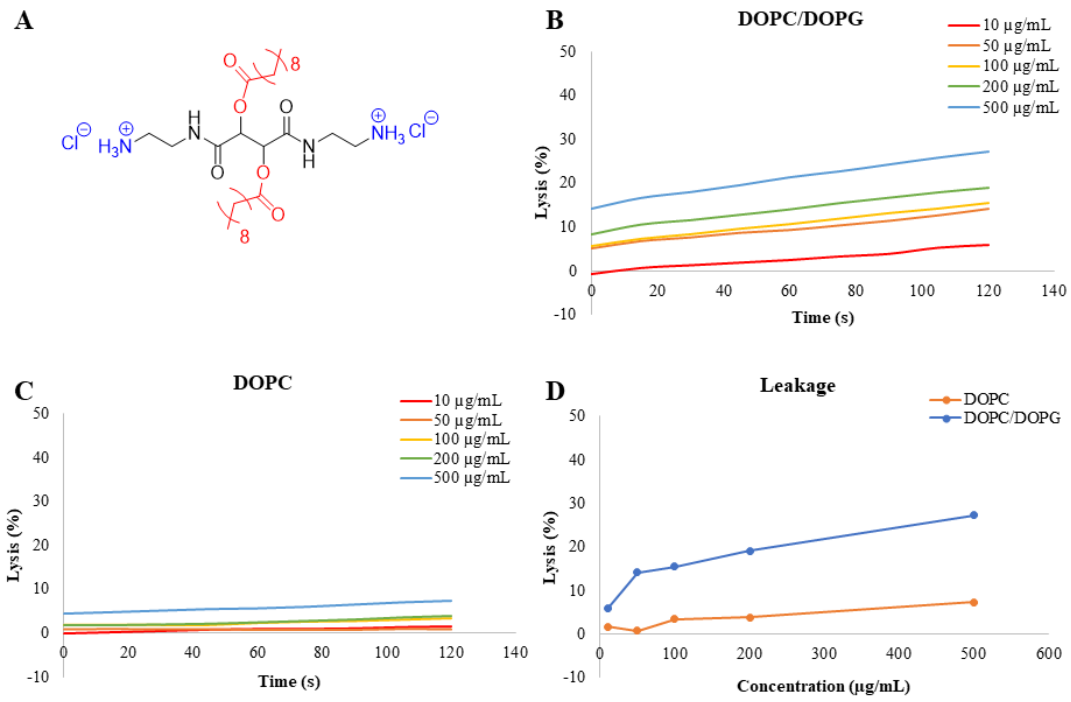

Figure 4.9. Calcein leakage experiments for CAm-esters. Results from experiments performed with ***6a*** (A) and negatively charged membranes (B) mimicking bacterial cells and neutral membranes (C) mimicking mammalian host cell membranes indicate membrane specificity. Comparison of total dye leakage at the end of the experiment for each membrane type (D) shows influence of CAm concentration.

4.3. Conclusion

Three series of CAms were synthesized and their membrane activity was evaluated to understand the impact of select chemical features, namely flexibility and hydrophobic architecture, on antimicrobial efficacy and selectivity. Generation of CAms was achieved via high yielding synthetic approaches that require fewer reactions than traditional peptide syntheses, resulting in larger quantities of product for lower financial investments. Several key features of CAms were identified that have significant influences on antimicrobial activity. CAm esters had the highest

activity against bacteria with the most desirable compatibility profiles. In particular, CAm esters with restricted charge flexibility (i.e., shorter linker lengths) were most potent against both Gram-positive and Gram-negative bacteria, and branched hydrophobic architecture had the most detrimental effect against Gram-negative bacteria. Together, these data highlight the potential for CAms as membrane active agents with specificity against bacteria to combat the surge of antibiotic resistance.

4.4. Experimental

4.4.1. Materials

All reagents were purchased from Sigma-Aldrich (St. Louis, MO) and used as received unless stated otherwise. Di-tert-butyl tartrate, *N*-Boc-ethylene diamine, *N*-Boc-1,4-diaminobutane, *N*-Boc-1,6-diaminohexane were purchased from TCI (Portland, OR). Whole blood was purchased from New Jersey Blood Center (East Orange, NJ). Lipids and polycarbonate membranes were purchased from Avanti Polar Lipids (Birmingham, AL).

4.4.2. Chemical characterization

Proton (^{1}H) and carbon (^{13}C) nuclear magnetic resonance (NMR) spectra were obtained using a Varian 500 MHz spectrometer. Samples were dissolved in deuterated chloroform ($CDCl_3$) with trimethylsilane (TMS) as an internal reference, or deuterated methanol (CD_3OD). Fourier transform infrared (FT-IR) spectra were obtained by solvent-casting small molecules onto sodium chloride (NaCl) plates from dichloromethane (DCM) solutions, and 32 scans were averaged and processed using OMNIC software on a Thermo Scientific Nicolet iS10 spectrophotometer. Molecular weights of CAms and intermediates were determined using a ThermoQuest Finnigan (LCQ-DUO system equipped with a syringe pump, optional divert/inject valve, atmospheric pressure ionization (API) source, and mass spectrometer (MS) detector). Samples were dissolved in methanol (10 μg/mL) and spectra were processed using Xcalibur.

4.4.3. Synthesis

4.4.3.1. CAm-Ethers with Extended Cationic Linkers (3)

Di-Boc-amino ether tartramide (***2***)- T10 ether (***1***) was prepared as previously described [28]. Mono-Boc protected diamines with various linker lengths (i.e., *N*-Boc-ethylenediamine, *N*-Boc-1,4-diaminobutane, *N*-Boc-1,6-diaminohexane) were conjugated to ***1*** via carbodiimide coupling following modified published procedures [19, 20]. Synthesis of ***2a*** is previously reported [20]. Synthesis of ***2c*** is presented as an example. T10 ether (0.27 mmol, 0.12 g) and 4-(dimethylamino)pyridine (DMAP, 0.70 mmol, 0.09g) were dissolved in anhydrous dichloromethane (DCM, 5 mL) under nitrogen and stirred for 10 minutes. *N*-Boc-1,6-diaminohexane (0.70 mmol, 0.15 mL) and N-(3-dimethylaminopropyl)-N′-ethylcarbodiimide hydrochloride (EDCI, 0.70 mmol, 0.13 g) were sequentially added to the reaction flask and stirred overnight at room temperature. The reaction mixture was washed with 10% potassium bisulfate ($KHSO_4$, 2X, 10 mL) and brine (1X, 10 mL). The organic layer was dried over magnesium sulfate ($MgSO_4$), filtered, and concentrated *in vacuo* to yield pure ***2c***.

2b: Yield: 93% (white solid) ^{1}H-NMR (500 MHz, $CDCl_3$): δ 0.87 (t, 6H), 1.24 (m, 28H), 1.42 (s, 18H), 1.52 (m, 8H), 1.67 (m, 4H), 3.12 (m, 4H), 3.31 (m, 4H), 3.47 (m, 4H), 4.24 (s, 2H), 4.55 (br, 2H), 6.69 (br, 2H). ^{13}C-NMR (500 MHz, $CDCl_3$): δ 14.09, 22.65, 26.01, 26.39, 26.57, 28.40, 29.29, 29.37, 29.54, 29.59, 29.69, 31.86, 39.03, 73.37, 81.08, 165.96, 169.85. ESI-MS *m/z*: $[M+23]^+$

2c: Yield: 86% (white solid) ^{1}H-NMR (500 MHz, $CDCl_3$): δ 0.87 (t, 6H), 1.24 (m, 28H), 1.33 (m, 4H), 1.43 (s, 18H), 1.52 (m, 8H), 1.71 (m, 4H), 3.09 (m, 4H), 3.27 (m, 4H), 3.47 (m, 4H), 4.25 (s, 2H), 4.50 (br, 2H), 6.71 (br, 2H). ^{13}C-NMR (500 MHz, $CDCl_3$): δ 14.06, 23.12, 25.98, 26.13, 26.32, 26.53, 27.99, 29.22, 29.41, 29.51, 29.54, 29.63, 32.00, 39.03, 73.33, 81.09, 166.87, 169.91. ESI-MS *m/z*: 793.5 $[M+23]^+$

CAm ether (***3***)- Boc protecting groups were removed under acidic conditions following literature precedence [19, 41]. Briefly, ***2*** was dissolved in hydrochloric acid in dioxane (4 M HCl, 10 mL) and cooled to 0 °C on ice. The reaction was stirred for 1 h on ice, then allowed to warm to room temperature and proceed overnight. Volatiles were removed *in vacuo,* and ***3*** was reconstituted in a minimum amount of methanol (< 4 mL), precipitated in hexanes (15 mL), and isolated by centrifugation (3500 rpm, 5 min) using a Hettich EBA 12 Centrifuge (Beverly, MA).

3a: Yield: quantitative (tan waxy solid) ^{1}H-NMR (500 MHz, CD_3OD): δ 0.89 (t, 6H), 1.29 (m, 28H), 1.56 (m, 4H), 1.63 (m, 4H), 1.69 (m, 4H), 2.96 (m, 4H), 3.19 (m, 4H), 3.30 (m, 8H), 3.59 (m, 2H), 4.08 (s, 2H). ^{13}C-NMR (500 MHz, CD_3OD): δ 13.03, 22.31, 24.41, 25.71, 26.09, 29.38, 29.34, 29.25, 29.20, 29.06, 31.65, 37.97, 38.89, 72.41, 81.23, 171.18. ESI-MS *m/z*: 286.3 $[(M+2)/2]^+$

3b*:* Yield: quantitative (off-white waxy solid) ^{1}H-NMR (500 MHz, CD_3OD): δ 0.89 (t, 6H), 1.29 (m, 28H), 1.41 (m, 8H), 1.55 (m, 8H), 1.65 (m, 4H), 2.91 (m, 4H), 3.17 (m, 4H), 3.30 (m, 8H), 3.65 (m, 2H), 4.08 (s, 2H). ^{13}C-NMR (500 MHz, CD_3OD): δ 13.03, 22.32, 25.98, 25.74, 25.60, 27.08, 29.37, 29.32, 29.24, 29.18, 29.07, 28.96, 31.64, 38.60, 39.23, 72.45, 81.05, 170.97. ESI-MS *m/z*: 314.4 $[(M+2)/2]^+$

4.4.3.2. CAm Esters with Extended Cationic Linkers (6)

Di-Boc-amino tartramide ***(4)***- Tartaric acid was subjected to an aminolysis reaction with mono-Boc protected diamines with various linker lengths (i.e., *N*-Boc-ethylenediamine, *N*-Boc-1,4-diaminobutane, *N*-Boc-1,6-diaminohexane) following methods described in previously reported procedures [19, 20]. Synthesis of ***4a-6a*** has previously been reported [20]. Reactions will be described using *N*-Boc-1,6-diaminohexane as an example. Briefly, dimethyl tartrate (0.56 mmol, 0.1 g) was dissolved in 3.0 mL tetrahydrofuran (THF) and heated to 40 °C. *N*-Boc-1,6-diaminohexane (1.57 mmol, 0.35 mL) was added, and the reaction stirred overnight at 40 °C.

Volatiles were removed *in vacuo* and ***4c*** precipitated in diethyl ether (15 mL) and isolated via filtration.

4b: Yield: 91% (white solid) ^{1}H-NMR (500 MHz, DMSO): δ 1.41 (s, 18), 1.51 (m, 8H), 3.10 (m, 4H), 3.28 (m, 4H), 4.31 (s, 2H), 4.75 (br, 2H), 7.15 (br, 2H). ^{13}C-NMR (500 MHz, DMSO): δ 28.93, 39.17, 39.20, 40.03, 73.71, 79.14, 156.12, 172.21. ESI-MS *m/z*: 513.4 $[M+23]^{+}$

4c: Yield: 79% (white solid) ^{1}H-NMR (500 MHz, DMSO): δ 1.32 (s, 8H), 1.44 (m, 30H), 1.61 (m, 4H), 3.09 (m, 4H), 3.25 (m, 4H), 4.26 (s, 2H), 4.60 (br, 2H), 5.37 (br, 2H), 7.10 (br, 2H). ^{13}C-NMR (500 MHz, DMSO): δ 26.42, 26.54, 28.93, 39.15, 39.24, 40.00, 73.72, 79.14, 156.07, 172.28. ESI-MS *m/z*: 569.4 $[M+23]^{+}$

Di-Boc-amino ester tartramide ***(5)- 4c*** was acylated by dissolving decanoic acid (0.46 mmol, 0.08 g) and DMAP (0.46 mmol, 0.06 g) in anhydrous DCM, followed by addition of the ***4c*** (0.12 mmol, 0.08 g) and EDC (0.46 mmol, 0.09 g). The reaction was stirred overnight under nitrogen and washed as described earlier for synthesis of ***2***.

5b: (white solid) ^{1}H-NMR (500 MHz, $CDCl_3$): δ 0.86 (t, 6H), 1.25 (m, 24H), 1.42 (s, 18H), 1.49 (m, 4H), 1.61 (m, 4H), 2.38 (t, 4H), 3.10 (m, 4H), 3.25 (m, 4H), 4.68 (br, 2H), 5.56 (s, 2H), 6.40 (br, 2H) ^{13}C-NMR (500 MHz, $CDCl_3$): δ 14.03, 22.63, 24.73, 25.79, 26.44, 27.33, 28.36, 29.01, 29.24, 29.41, 31.80, 33.87, 36.85, 39.14, 40.01, 72.12, 79.14, 156.06, 166.31, 172.27. ESI-MS *m/z*: 822.2 $[M+23]^{+}$

5c: (off-white solid) ^{1}H-NMR (500 MHz, $CDCl_3$): δ 0.86 (t, 6H), 1.30 (m, 24H), 1.25 (m, 8H), 1.43 (s, 18H), 1.62 (m, 8H), 2.38 (t, 4H), 3.09 (m, 4H), 3.22 (m, 4H), 4.55 (br, 2H), 5.57 (s, 2H), 6.22 (br, 2H). ^{13}C-NMR (500 MHz, $CDCl_3$): δ 14.07, 22.63, 24.78, 26.04, 26.11, 28.43, 29.06, 29.19, 29.26, 29.40, 29.93, 31.80, 33.89, 39.19, 40.23, 72.13, 79.81, 157.21, 166.24, 172.30. ESI-MS *m/z*: 855.1 $[M+1]^{+}$

CAm ester ***(6)***- Boc groups were removed as previously described using 4 M HCl in dioxane. Products were isolated via precipitation in cold diethyl ether (15 mL) followed by centrifugation as previously described to isolate the products.

6b: Yield: quantitative (off-white waxy solid) ^{1}H-NMR (500 MHz, CD_3OD): δ 0.89 (t, 6H), 1.29 (m, 24H), 1.59 (m, 12H), 2.46 (4H), 2.94 (t, 4H), 3.23 (m, 4H), 5.54 (s, 2H). ^{13}C-NMR (500 MHz, CD_3OD): δ 13.03, 22.31, 24.33, 24.40, 25.82, 28.75, 29.01, 29.05, 29.18, 31.63, 33.20, 38.17, 38.89, 72.28, 167.50, 172.63. ESI-MS *m/z*: 300.2 $[(M+2)/2]^+$

6c: Yield: quantitative (yellowish waxy solid) ^{1}H-NMR (500 MHz, CD_3OD): δ 0.89 (t, 6H), 1.30 (m, 32H), 1.51 (t, 4H), 1.65 (m, 8H), 2.46 (m, 4H), 2.91 (t, 4H), 3.19 (m, 4H), 5.54 (s, 2H). ^{13}C-NMR (500 MHz, CD_3OD): δ 13.03, 22.31, 24.41, 25.50, 25.74, 27.01, 28.66, 28.76, 29.01, 29.05, 29.18, 31.62, 33.19, 38.75, 39.20, 72.27, 167.35, 172.51. ESI-MS *m/z*: 328.4 $[(M+2)/2]^+$

4.4.3.3. Branched CAms (*11*)

Branched arm ***(7)***- Branched arms were synthesized by acylating 2,2-bis(hydroxymethyl)propionic acid (bis-MPA) following modified literature procedures [29]. Synthesis of ***11b*** will be provided as an example. Bis-MPA (7.4 mmol, 1.0 g) was dissolved in a solution of dimethylformamide (DMF, 2.0 mL) and pyridine (0.2 mL) under nitrogen. Valeroyl chloride (18.6 mmol, 2.24 mL) was added, and the reaction stirred overnight at room temperature. Chloroform (5.0 mL) and HCl (1 N, 5.0 mL) were added to the resulting slurry and stirred for 10 min. The aqueous layer was extracted with chloroform (3X, 10 mL) and the combined organic layers washed with a 1:1 mixture of saturated sodium bicarbonate ($NaHCO_3$) and brine (1X, 10 mL). The organic layer was dried over $MgSO_4$, filtered, and concentrated *in vacuo*. The crude product was recrystallized from hexanes to purify ***7b***.

7a: Yield: 82% (clear oil) ^{1}H-NMR (500 MHz, $CDCl_3$): δ 0.87 (t, 6H), 1.24 (s, 3H), 1.29 (m, 4H), 1.55 (q, 4H), 2.28 (t, 4H), 4.23 (d, 4H). ^{13}C-NMR (500 MHz, $CDCl_3$): δ 13.62, 17.70, 22.14, 26.82, 33.78, 46.14, 64.99, 173.32, 178.85. ESI-MS *m/z*: 301.0 $[M-1]^-$

7b: Yield: 71% (white solid) ^{1}H-NMR (500 MHz, $CDCl_3$): δ 0.88 (t, 6H), 1.26 (m, 24H), 1.30 (s, 3H), 1.59 (qn, 4H), 2.31 (t, 4H), 4.23 (s, 4H). ^{13}C-NMR (500 MHz, $CDCl_3$): δ 14.05, 17.23, 22.65, 24.79, 29.10, 29.23, 29.25, 29.40, 31.84, 33.97, 47.87, 64.54, 167.50, 173.05. ESI-MS *m/z*: 441.2 $[M-1]^-$

Di-branched dibenzyl tartrate ***(8)***- ***7*** was conjugated to dibenzyl tartrate (DBT) via carbodiimide coupling. ***7b*** (0.66 mmol, 0.19 g) was dissolved in DCM (5.0 mL) followed by addition of DMAP (0.66 mmol, 0.08 g) and allowed to stir for 10 min under nitrogen. DBT (0.3 mmol, 0.10 g) was added to the reaction followed by EDC (0.66 mmol, 0.13 g) and stirred overnight. The resulting solution was washed with 10% $KHSO_4$ (2X, 10 mL) and a 1:1 mixture of saturated $NaHCO_3$ and brine (1X, 10 mL). The organic layer was dried over $MgSO_4$, filtered, and concentrated *in vacuo*. ***8a*** required no further purification. ***8b*** was subjected to flash column chromatography using 12 % ethyl acetate in hexanes as the mobile phase to yield pure product.

8a: Yield: 75% (white solid) ^{1}H-NMR (500 MHz, $CDCl_3$): δ 0.88 (t, 12H), 1.15 (s, 6H), 1.30 (m, 8H), 1.55 (m, 8H), 2.26 (m, 8H), 4.19 (m, 8H), 5.13 (s, 4H), 5.73 (s, 2H), 7.31 (m, 10H). ^{13}C-NMR (500 MHz, $CDCl_3$): δ 13.68, 17.45, 22.20, 26.82, 33.69, 46.33, 64.63, 68.00, 70.84, 128.32, 128.67, 128.75, 134.43, 164.93, 171.40, 173.15. ESI-MS *m/z*: 921.4 $[M+23]^+$

8b: Yield: 65% (white solid) ^{1}H-NMR (500 MHz, $CDCl_3$): δ 0.86 (t, 12H), 1.16 (s, 6H), 1.25 (m, H), 1.57 (m, 8H), 2.24 (m, 8H), 4.17 (m, 8H), 5.13 (s, 4H), 5.73 (s, 2H), 7.31 (m, 10H). ^{13}C-NMR (500 MHz, $CDCl_3$): δ 14.08, 17.46, 22.65, 24.78, 29.12, 29.26, 29.43, 31.84, 33.95, 33.97, 46.34, 64.60, 67.97, 70.86, 128.34, 128.70, 128.74, 134.44, 164.90, 171.40, 173.13. ESI-MS *m/z*: 1201.9 $[M+23]^-$

Di-branched tartaric acid ***(9)***: Benzyl groups were removed via hydrogenolysis with palladium on carbon (Pd/C, 10% w/w) as the catalyst for 24 h in DCM (10 mL). The reaction mixture was then filtered through Celite to remove Pd/C and ***9*** concentrated *in vacuo*.

9a: Yield: quantitative (white solid) ^{1}H-NMR (500 MHz, $CDCl_3$): δ 0.87 (t, 12H), 1.31 (m, 14H), 1.57 (m, 8H), 2.32 (m, 8H), 4.20 (m, 8H), 5.62 (s, 2H). ^{13}C-NMR (500 MHz, $CDCl_3$): δ 13.64, 17.36, 22.16, 26.78, 26.82, 71.04, 167.30, 171.11, 173.77, 174.00. ESI-MS *m/z*: 717.1 $[M-1]^-$

9b: Yield: quantitative (white solid) ^{1}H-NMR (500 MHz, $CDCl_3$): δ 0.87 (t, 12H), 1.26 (m, H), 1.32 (s, 6H), 1.58 (m, 8H), 2.31 (m, 8H), 4.20 (m, 8H), 5.63 (s, 2H). ^{13}C-NMR (500 MHz, $CDCl_3$): δ 14.08, 17.37, 22.69, 24.75, 24.80, 29.11, 29.26, 29.43, 31.85, 34.07, 46.43, 64.91, 65.18, 71.01, 166.73, 171.05, 173.73, 174.00. ESI-MS *m/z*: 998.2 $[M-1]^-$

Di-branched, di-Boc-amino tartramide ***(10)***- Mono-Boc protected diamines were conjugated following a modified literature procedure [42]. ***9b*** (0.34 mmol, 0.34 g) was dissolved in DCM (5.0 mL) and cooled to 0 °C on ice. HOBt (0.68 mmol, 0.09 g) and *N*-Boc-ethylenediamine were added sequentially. DCC (1 M, 0.68 mmol, 0.68 mL) was then slowly added, and the reaction stirred for 15 min on ice. The resulting mixture was allowed to warm to room temperature and stirred overnight. The reaction was cooled to -20 °C to facilitate the urea byproduct precipitation, which was removed via filtration. The filtrate was concentrated *in vacuo* and subjected to flash column chromatography with 5% methanol in DCM as the eluent. If further purification was required, the crude ***10b*** was recrystallized in cold hexanes.

10a: Yield: 76% (white solid) ^{1}H-NMR (500 MHz, $CDCl_3$): δ 0.90 (t, 12H), 1.30 (m, H), 1.42 (m, 18H), 1.58 (m, 8H), 1.66 (s,), 2.32 (m, 8H), 3.26-3.40 (m, 8H), 4.13-4.43 (m, 8H), 5.27 (s, 2H), 5.56 (s, 2H), 6.96 (s, 2H). ^{13}C-NMR (500 MHz, $CDCl_3$): δ 13.72, 17.69, 22.19, 28.41,

26.83, 33.77, 40.49, 39.82, 46.67, 64.92, 64.80, 72.83, 79.45, 165.88, 171.23, 173.52. ESI-MS *m/z*: 1025.6 $[M+23]^+$

10b: Yield: 66% (white solid) ^{1}H-NMR (500 MHz, $CDCl_3$): δ 0.86 (t, 12H), 1.25 (m, H), 1.28 (s, 6H), 1.59 (m, 18H), 1.64 (m, 8H), 2.29 (8H), 3.25-3.38 (m, 8H), 4.11-4.41 (m, 8H), 5.25 (s, 2H), 5.55 (s, 2H), 6.93 (s, 2H). ^{13}C-NMR (500 MHz, $CDCl_3$): 14.08, 17.65, 22.64, 24.80, 28.38, 29.09, 29.24, 29.41, 31.85, 34.05, 46.68, 64.79, 64.92, 72.85, 79.44, 165.92, 171.27, 173.47, 173.59. ESI-MS *m/z*: 1305.6 $[M+23]^+$

Branched CAm ***(11)-*** Boc groups were removed to generate the final products using 4 M HCl in dioxane following the aforementioned procedure. Products were isolated *in vacuo*.

11a: Yield: quantitative (off-white paste) ^{1}H-NMR (500 MHz, $CDCl_3$): δ 0.91 (t, 12H), 1.33 (m, 14H), 1.57 (m, 8H), 2.35 (m, 8H), 3.10 (m, 4H), 3.43-3.59 (d of m, 4H), 4.18-4.43 (m, 8H), 5.63 (s, 2H). ^{13}C-NMR (500 MHz, $CDCl_3$): 13.18, 16.39, 22.01, 24.85, 33.70, 39.69, 40.82, 45.15, 65.17, 75.73, 167.30, 171.73, 173.95, 174.01. ESI-MS *m/z*: 402.4 $[(M+2)/2]^+$

11b: Yield: quantitative (off-white sticky solid) ^{1}H-NMR (500 MHz, $CDCl_3$): δ 0.89 (t, 12H), 1.33 (m, 48 H), 1.29 (s, 6H), 1.58 (m, 8H), 2.34 (m, 8H), 3.10 (m, 4H), 3.38-3.73 (d of m, 4H), 4.12-4.45 (m, 8H), 5.57 (s, 2H). ^{13}C-NMR (500 MHz, $CDCl_3$): δ13.09, 16.65, 22.32, 24.59, 28.84, 29.06, 29.08, 29.22, 31.70, 33.50, 36.82, 39.07, 46.43, 64.56, 72.52, 167.31, 171.72, 173.43, 173.51. ESI-MS *m/z*: 542.8 $[(M+2)/2]^+$

4.4.3.4. Cytotoxicity

In vitro cytotoxicity was evaluated in 3T3 fibroblasts. Cells were cultured in Dulbecco's Modified Eagle Medium (DMEM) supplemented with 10% fetal bovine serum (complete media) at 37 °C, 95% humidity, and 5% CO_2. Samples were solubilized in sterile 10 mM HEPES buffer, pH 7.4 and diluted in complete media to the desired concentrations. Cells were seeded onto a 96-well tissue culture plate at 5000 cells/well in 100 µL of complete media and allowed to attach for

24 h. Media was aspirated and replaced with CAm solutions and controls (HEPES buffer diluted with complete media) and cells were incubated under standard conditions for an additional 24 h. Cell viability was then determined using a CellTiter 96 Aqueous One Solution Proliferation Assay following manufacturer suggested protocol and absorbance was recorded using an Infinite M200 PRO plate reader (Tecan Group Ltd., Männedorf, Switzerland).

4.4.3.5. Hemolysis

Hemolytic activity of CAms was determined in human red blood cells. Red blood cells were isolated from whole blood by centrifugation at 400 x g min (Allegra 21 centrifugation, Beckman Coulter, Brea, CA) for 15 minutes. The supernatant was carefully removed via pipette aspiration and the red blood cells washed with isotonic HEPES buffer (5X, 10 mM, 0.8% NaCl, pH 7.4). The red blood cells were resuspended in isotonic HEPES buffer to 5% hematocrit. CAm stock solutions were prepared in isotonic HEPES buffer and serial diluted to predetermined concentrations for the hemolysis assays. CAm solutions (400 µL) and controls (ddH_2O and isotonic HEPES buffer) were mixed with red blood cell suspensions (100 µL) and incubated for 1 h at 37 °C. Red blood cells were pelleted via centrifugation (Labenet Spectrafuge 16 M microcentrifuge, Labnet International, Inc., Edison, NJ, 400 x g, 10 min) and the supernatant absorbance read at 410 nm using an Infinite M200 PRO plate reader (Tecan Group Ltd., Männedorf, Switzerland). Percent hemolysis was calculated with the following equation:

$$Hemolysis\ (\%) = \frac{Abs_{sample} - Abs_{buffer}}{Abs_{ddH2O} - Abs_{buffer}} * 100\%$$

The concentration of CAms was plotted against the calculated percent hemolysis, and the point on the curve corresponding to the concentration required for 50% hemolysis was taken as the HC_{50}.

4.4.6. Bacteria Cell Culture

[Bacteria cell culture was carried out by Richard M. Weeks, Department of Molecular Biology and Biochemistry, Rutgers University, Piscataway, NJ.]

Bacteria were inoculated into brain-heart infusion (BHI) agar (Becton Dickinson, Franklin Lakes, NJ) and propagated under aerobic conditions at 37 ˚C for 24 h. A single colony of each bacterial strain was transferred to BHI broth (Becton Dickinson, Franklin Lakes, NJ) and incubated under aerobic conditions at 37 ˚C for 18 – 24 h. Bacterial growth suspensions were diluted in fresh BHI medium to a concentration of 106 CFU/mL for microbroth dilution assays.

4.4.7. Minimum Inhibitory Concentration (MIC) Determination

[MIC experiments were performed by Richard M. Weeks, Department of Molecular Biology and Biochemistry, Rutgers University, Piscataway, NJ.]

CAm's MICs were determined using a broth microdilution assay. CAm stock solutions were prepared in ddH_2O and sterilized under UV light for 25 min. Stock solutions were serial diluted into a 96-well microplate in duplicate ((Becton Dickinson, Franklin Lakes, NJ) with BHI broth to 100 µL. Aliquots (100 µL) of bacterial suspensions were added to wells, and incubated at 37 °C for 24 h under aerobic conditions. The OD_{595} of bacteria were tracked using a microplate reader (Model 550, Bio-Rad Laboratories, Hercules, CA). The MIC was determined as the lowest CAm concentration that produced no visible growth after 24 h incubation.

4.4.8. Hydrophilic Dye Release from Large Unilamellar Vesicles (LUVs)

CAm's ability to target and lyse membranes was evaluated in large unilamellar vesicles (LUVs) mimicking mammalian and bacterial cell membranes following modified literature procedures [43]. LUVs were prepared via the thin film hydration and extrusion method. 1,2-dioleoyl-sn-glycero-3-phosphocholine (DOPC, 25 mg/mL) or a 1:1 mixture of DOPC/ 1,2-

dioleoyl-sn-glycero-3-phospho-(1'-rac-glycerol) (DOPG) were mixed in 20 mL scintillation vials, concentrated *in vacuo*, and further dried overnight in a vacuum desiccator. Lipid films were hydrated with 70 mM calcein in HEPES release buffer (10 mM, 150 mM NaCl, 1 mM ethylenediaminetetraacetic acid (EDTA), pH 7.4) for 1 h at 40 °C with gentle agitation. Hydrated films were subjected to 5 freeze/thaw cycles by heating vesicles at 40 °C in a water bath and freezing in dry ice at -78 °C for 15 min each. Multilamellar vesicles were extruded 11 times through a 100 nm polycarbonate membrane at 40 °C with an Avanti Mini-Extruder. Unencapsulated calcein was removed via size exclusion chromatography using Sephadex G50 Fine resin as the stationary phase and HEPES release buffer as the eluent. Phospholipid concentration was determined via a Phospholipid Assay Kit (Sigma-Aldrich) as per manufacturer suggested protocol. LUVs were diluted to 10 µM in HEPES release buffer for experiments.

CAm solutions were prepared in HEPES release buffer. Background fluorescence of LUV suspensions was read on a RF-5301PC spectrofluorimeter (Shimadzu Scientific Instruments, Columbia, MD) at an excitation wavelength of 495 nm and an emission wavelength of 515 nm. CAm solutions were added to 1 mL of LUV suspensions and fluorescence immediately read and monitored for 2 minutes. At end of experiments, 20 µL of 5% Triton X was added to samples to fully release dye from the LUV suspensions. Percent lysis was calculated using the following equation:

$$Lysis\ (\%) = \frac{F_{sample} - F_0}{F_{triton} - F_0} * 100\%$$

where F_{sample} represents the stabilized fluorescence reading after CAm addition, F_0 represents the background fluorescence, and F_{triton} represents the fluorescence recorded after full LUV lysis with Triton X.

4.5 Appendix for Chapter 3

4.5.1. Critical Micelle Concentrations of CAms

The self-assembly and folding characteristics of AMPs correlate closely with antimicrobial activity [6]. The characteristics that contribute to membrane interactions include the formation of higher order AMP aggregates, as well as their secondary structures, such as α-helix formation [6, 8, 44]. While CAms' chemical structures deviate from AMPs in several regards, it is possible that their ability to self-assemble into higher order aggregates influences membrane activity in a similar manner. As such, critical micelle concentrations (CMCs) of CAms were determined via surface tensiometry. Due to CAms' amphiphilic nature, each were shown to have defined changes in surface tension at a given concentration where they presumably self-assemble into higher order aggregates as indicated in **Table 4.2.** Solutions above the CMCs determined via surface tensiometry were subjected to analysis by dynamic light scattering (DLS) to evaluate aggregate size. However, the size of aggregates was multimodal and dynamic over the course of the experiments, indicating that they are likely not spherical in nature or phase separate. It would therefore be interesting, and a potential source of future work, to probe into the shape of aggregates via cryo-transmission electron microscopy (Cryo-TEM) and evaluate how concentration dictates aggregate morphology and phase behavior.

Table 4.2. CMCs of CAms as determined via surface tensiometry.

CAm	CMC (μg/mL)
2C-ether (*3a*)	27
4C-ether (*3b*)	57
6C-ether (*3c*)	134
2C-ester (*6a*)	79
4C-ester (*6b*)	96
6C-ester (*6c*)	163

4.5.2. Experimental

4.5.2.1. Determination of Critical Micelle Concentrations

Critical micelle concentrations (CMCs) were determined via tensiometry using a Fisher Surface Tensiometer Model 21 (Walkham, MA). The platinum ring was rinsed with acetone, methanol, and deionized water and heated with a Bunsen burner prior to measurements. A CAm stock solution was prepared in deionized water and the surface tension measured in a clean vessel in triplicate. The solution was diluted directly in the vessel with deionized water, and surface tension was measured at predetermined concentrations. The surface tension was graphed against the logarithm of CAm concentration, and the inflection point was taken as the CMC.

4.6. References

[1] Llor C, Bjerrum L. Antimicrobial resistance: risk associated with antibiotic overuse and initiatives to reduce the problem. Therapeutic Advances in Drug Safety. 2014;5:229-41.

[2] Dellit TH, Owens RC, McGowan JE, Gerding DN, Weinstein RA, Burke JP, et al. Infectious Diseases Society of America and the Society for Healthcare Epidemiology of America guidelines for developing an institutional program to enhance antimicrobial stewardship. Clinical infectious diseases. 2007;44:159-77.

[3] Boucher HW, Talbot GH, Bradley JS, Edwards JE, Gilbert D, Rice LB, et al. Bad bugs, no drugs: no ESKAPE! An update from the Infectious Diseases Society of America. Clinical Infectious Diseases. 2009;48:1-12.

[4] Zasloff M. Antimicrobial peptides of multicellular organisms. Nature. 2002;415:389-95.

[5] Brogden KA. Antimicrobial peptides: pore formers or metabolic inhibitors in bacteria? Nature reviews Microbiology. 2005;3:238.

[6] Chongsiriwatana NP, Patch JA, Czyzewski AM, Dohm MT, Ivankin A, Gidalevitz D, et al. Peptoids that mimic the structure, function, and mechanism of helical antimicrobial peptides. Proceedings of the National Academy of Sciences. 2008;105:2794-9.

[7] Shai Y. Mode of action of membrane active antimicrobial peptides. Peptide Science. 2002;66:236-48.

[8] Shai Y. Mechanism of the binding, insertion and destabilization of phospholipid bilayer membranes by α-helical antimicrobial and cell non-selective membrane-lytic peptides. Biochimica et Biophysica Acta (BBA)-Biomembranes. 1999;1462:55-70.

[9] Guilhelmelli F, Vilela N, Albuquerque P, Derengowski LdS, Silva-Pereira I, Kyaw CM. Antibiotic development challenges: the various mechanisms of action of antimicrobial peptides and of bacterial resistance. Frontiers in microbiology. 2013;4.

[10] Hancock RE, Lehrer R. Cationic peptides: a new source of antibiotics. Trends in biotechnology. 1998;16:82-8.

[11] Marr AK, Gooderham WJ, Hancock RE. Antibacterial peptides for therapeutic use: obstacles and realistic outlook. Current opinion in pharmacology. 2006;6:468-72.

[12] Alanis AJ. Resistance to Antibiotics: Are We in the Post-Antibiotic Era? Archives of Medical Research. 2005;36:697-705.

[13] Sieprawska-Lupa M, Mydel P, Krawczyk K, Wójcik K, Puklo M, Lupa B, et al. Degradation of human antimicrobial peptide LL-37 by Staphylococcus aureus-derived proteinases. Antimicrobial agents and chemotherapy. 2004;48:4673-9.

[14] Bahar AA, Ren D. Antimicrobial peptides. Pharmaceuticals. 2013;6:1543-75.

[15] Jennings MC, Ator LE, Paniak TJ, Minbiole KP, Wuest WM. Biofilm-Eradicating Properties of Quaternary Ammonium Amphiphiles: Simple Mimics of Antimicrobial Peptides. ChemBioChem. 2014;15:2211-5.

[16] Black JW, Jennings MC, Azarewicz J, Paniak TJ, Grenier MC, Wuest WM, et al. TMEDA-derived biscationic amphiphiles: An economical preparation of potent antibacterial agents. Bioorganic & medicinal chemistry letters. 2014;24:99-102.

[17] Som A, Vemparala S, Ivanov I, Tew GN. Synthetic mimics of antimicrobial peptides. Peptide Science. 2008;90:83-93.

[18] Ong ZY, Wiradharma N, Yang YY. Strategies employed in the design and optimization of synthetic antimicrobial peptide amphiphiles with enhanced therapeutic potentials. Advanced drug delivery reviews. 2014;78:28-45.

[19] Faig A, Arthur TD, Fitzgerald PO, Chikindas M, Mintzer E, Uhrich KE. Biscationic tartaric acid-based amphiphiles: charge location impacts antimicrobial activity. Langmuir. 2015;31:11875-85.

[20] Zhang Y, Algburi A, Wang N, Kholodovych V, Oh DO, Chikindas M, et al. Self-assembled cationic amphiphiles as antimicrobial peptides mimics: Role of hydrophobicity, linkage type, and assembly state. Nanomedicine: Nanotechnology, Biology and Medicine. 2017;13:343-52.

[21] Palermo EF, Vemparala S, Kuroda K. Cationic Spacer Arm Design Strategy for Control of Antimicrobial Activity and Conformation of Amphiphilic Methacrylate Random Copolymers. Biomacromolecules. 2012;13:1632-41.

[22] Vermeer LS, Lan Y, Abbate V, Ruh E, Bui TT, Wilkinson LJ, et al. Conformational Flexibility Determines Selectivity and Antibacterial, Antiplasmodial and Anticancer Potency of Cationic α-Helical Peptides. The Journal of biological chemistry. 2012;287:34120-33.

[23] Kolodkin-Gal I, Cao S, Chai L, Böttcher T, Kolter R, Clardy J, et al. A self-produced trigger for biofilm disassembly that targets exopolysaccharide. Cell. 2012;149:684-92.

[24] Mowery BP, Lee SE, Kissounko DA, Epand RF, Epand RM, Weisblum B, et al. Mimicry of antimicrobial host-defense peptides by random copolymers. Journal of the American Chemical Society. 2007;129:15474-6.

[25] Grenier MC, Davis RW, Wilson-Henjum KL, LaDow JE, Black JW, Caran KL, et al. The antibacterial activity of 4, 4′-bipyridinium amphiphiles with conventional, bicephalic and gemini architectures. Bioorganic & medicinal chemistry letters. 2012;22:4055-8.

[26] Chen CZ, Beck-Tan NC, Dhurjati P, van Dyk TK, LaRossa RA, Cooper SL. Quaternary Ammonium Functionalized Poly(propylene imine) Dendrimers as Effective Antimicrobials: Structure−Activity Studies. Biomacromolecules. 2000;1:473-80.

[27] Lind T, Polcyn P, Zielinska P, Cárdenas M, Urbanczyk-Lipkowska Z. On the Antimicrobial Activity of Various Peptide-Based Dendrimers of Similar Architecture. Molecules. 2015;20:738.

[28] Zhang Y, Li Q, Welsh WJ, Moghe PV, Uhrich KE. Micellar and structural stability of nanoscale amphiphilic polymers: implications for anti-atherosclerotic bioactivity. Biomaterials. 2016;84:230-40.

[29] Liu Y, Fan Y, Liu X-Y, Jiang S-Z, Yuan Y, Chen Y, et al. Amphiphilic hyperbranched copolymers bearing a hyperbranched core and dendritic shell: synthesis, characterization and guest encapsulation performance. Soft Matter. 2012;8:8361-9.

[30] Suwandecha T, Srichana T, Balekar N, Nakpheng T, Pangsomboon K. Novel antimicrobial peptide specifically active against Porphyromonas gingivalis. Archives of Microbiology. 2015;197:899-909.

[31] Duval E, Zatylny C, Laurencin M, Baudy-Floc'h M, Henry J. KKKKPLFGLFFGLF: A cationic peptide designed to exert antibacterial activity. Peptides. 2009;30:1608-12.

[32] Cochrane SA, Lohans CT, Brandelli JR, Mulvey G, Armstrong GD, Vederas JC. Synthesis and structure–activity relationship studies of N-terminal analogues of the antimicrobial peptide tridecaptin A1. Journal of medicinal chemistry. 2014;57:1127-31.

[33] Code of Federal Regulations. In: Administration USFaD, editor. Title 21, Chapter 1, Subchapter B-- Food for human consumption, Volume 32017.

[34] Code of Federal Regulations. In: Administration USFaD, editor. Title 21, Chapter I, Subchapter B, Part 184- Direct Food Substances Affirmed as Generally Recognized as Safe2017.

[35] Delcour AH. Outer Membrane Permeability and Antibiotic Resistance. Biochimica et biophysica acta. 2009;1794:808-16.

[36] LaDow JE, Warnock DC, Hamill KM, Simmons KL, Davis RW, Schwantes CR, et al. Bicephalic amphiphile architecture affects antibacterial activity. European Journal of Medicinal Chemistry. 2011;46:4219-26.

[37] Rotem S, Mor A. Antimicrobial peptide mimics for improved therapeutic properties. Biochimica et Biophysica Acta (BBA) - Biomembranes. 2009;1788:1582-92.

[38] Faig AM. Design, synthesis, and characterization of bioactive amphiphiles for therapeutic applications: Rutgers University-Graduate School-New Brunswick; 2015.

[39] Wieprecht T, Dathe M, Beyermann M, Krause E, Maloy WL, MacDonald DL, et al. Peptide hydrophobicity controls the activity and selectivity of magainin 2 amide in interaction with membranes. Biochemistry. 1997;36:6124-32.

[40] Dagan A, Efron L, Gaidukov L, Mor A, Ginsburg H. In vitro antiplasmodium effects of dermaseptin S4 derivatives. Antimicrobial agents and chemotherapy. 2002;46:1059-66.

[41] Han G, Tamaki M, Hruby V. Fast, efficient and selective deprotection of the tert-butoxycarbonyl (Boc) group using HCl/dioxane (4 m). Chemical Biology & Drug Design. 2001;58:338-41.

[42] Buijnsters PJ, García Rodríguez CL, Willighagen EL, Sommerdijk NA, Kremer A, Camilleri P, et al. Cationic gemini surfactants based on tartaric acid: synthesis, aggregation, monolayer behaviour, and interaction with DNA. European Journal of Organic Chemistry. 2002;2002:1397-406.

[43] Arias M, Vogel HJ. Fluorescence and Absorbance Spectroscopy Methods to Study Membrane Perturbations by Antimicrobial Host Defense Peptides. Antimicrobial Peptides: Methods and Protocols. 2017:141-57.

[44] Mani R, Tang M, Wu X, Buffy J, Waring A, Sherman M, et al. Membrane-bound dimer structure of a β-hairpin antimicrobial peptide from rotational-echo double-resonance solid-state NMR. Biochemistry. 2006;45:8341-9.

5. APPENDIX A: LIGAND-CONJUGATED AMPHIPHILIC MACROMOLECULES FOR LIPID HOMESTASIS IN ATHEROSLEROTIC APPLICATIONS

This appendix summarizes foundational and preliminary work that was done to mitigate the atherosclerotic phenotype in macrophages. It includes synthesis of several compounds and preliminary testing.

5.1. Introduction

During the atherosclerotic cascade, macrophages uncontrollably internalize oxidized lipids, leading to the foam cell phenotype, subsequent rupture, and formation of the necrotic core of plaques [1, 2]. To combat these stages of disease progression, mechanisms to reduce the cholesterol content in macrophages is critical. The Liver X Receptor (LXR) is a nuclear receptor that forms a heterodimer with the Retinoid X Receptor (RXR), resulting in transcription of lipid homeostasis genes. In particular, LXR agonism upregulates the expression of ATP-Binding Cassette Transporter A1 (ABCA1), a membrane receptor that promote cholesterol efflux [3, 4]. Reduced or absent expression of ABCA1 has been associated with the inability to transfer cholesterol to Apolipoprotein AI (ApoAI), demonstrating its critical role in promoting cholesterol efflux and mechanisms used to reduce atherosclerotic outcomes [5, 6]. LXR is activated by native oxysterols, as well as synthetic drug-like molecules [7].

The Uhrich group has previously delivered LXR agonist, GW3965, in micellar preparations of 1cM, resulting in decreased cholesterol accumulation and a 16-fold increase in ABCA1 expression in macrophages, whereas the agonist alone resulted in a 3-fold increase in ABCA1 expression [8]. Preliminary work performed by Dr. Latrisha Petersen (Department of Biomedical Engineering, Rutgers, Piscataway, NJ) encapsulated a variety of small ligands in 1cM NPs and evaluated their effect on gene transcription levels in human monocyte-derived macrophages. This data indicated that two ligands, lithocholic acid (LCA) and ursodeoxycholic

acid, resulted in increased expression of ABCA1 (**Figure 5.1**) LCA delivery resulted in enhanced expression when encapsulated in the core of NPs as compared to treatment with LCA in the absence of a delivery vehicle, whereas ursodeoxycholic acid had greater efficacy when delivered alone than in NP cores.

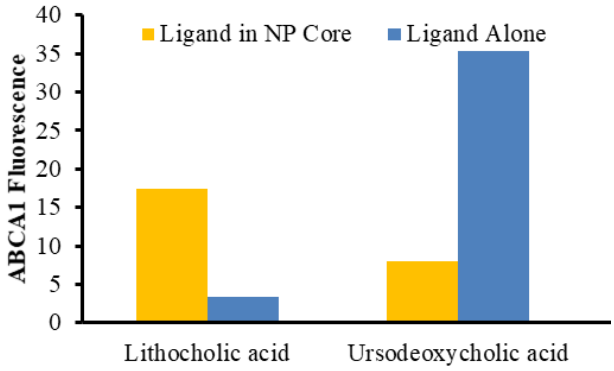

Figure 5.1. ABCA1 fluorescence intensity in macrophages treated with 1cM NPs encapsulating small molecules or treated with the ligands alone as compared to untreated basal controls.

As such, AMs were designed with either LCA conjugated to 1cM or ursodeoxycholic acid conjugated to 1cM. It is important to note that bile acids are not natural LXR ligands. However, their structural similarity to oxysterols, high affinity binding to related receptors (e.g., Farnesoid X Receptor (FXR)), and formulation into NPs may be attributable to the observed results [9].

5.2. Results and Discussion

5.2.1. Synthesis of PEGylated ligands

As the carboxylate functionality is imperative for AMs to interact with SRs to inhibit oxLDL uptake, the synthetic scheme shown in **Figure 5.2** was utilized to generate PEGylated ligands (i.e., LCA and ursodeoxycholic acid) for NP preparation and potential LXR activation with free carboxylates [10]. In doing so, PEG also serves to increase the bioavailability of these two highly hydrophobic, and thus sparingly water-soluble, ligands [11, 12]. In order to generate the

PEG-ligand conjugates, the carboxylic acids of ligands were selectively protected using benzyl bromide under basic conditions. PEG-succinate was conjugated to the benzyl protected ligand (***2***) via carbodiimide coupling to generate ***3***. The benzyl group was removed via hydrogenolysis with Pd/C to generate the free acid. .

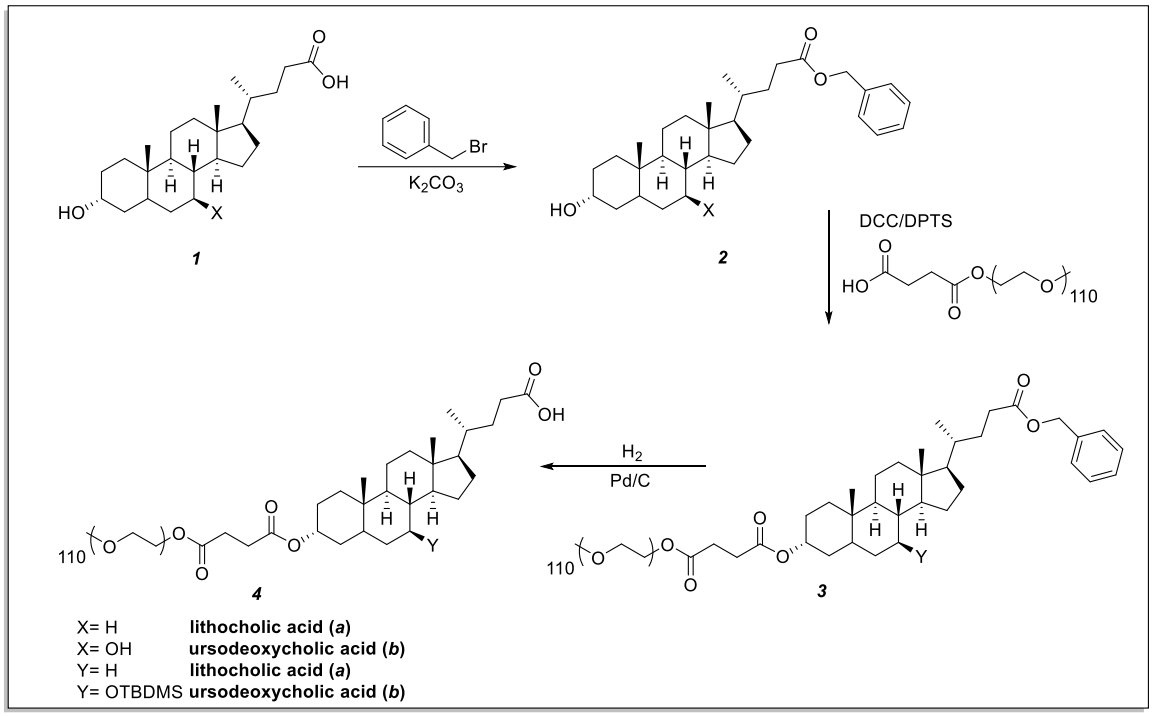

Figure 5.2: Representative synthesis of PEG-ligand conjugates bearing a free carboxylic acid

While the negative charge of these conjugates may facilitate SR interactions, they may also prevent interactions with LXR. Structure-activity relationship studies have demonstrated a correlation between high affinity binding and agonism with a stereoselective oxygen on the sterol ring of oxysterols [7]. As PEG conjugation through this site would inhibit such interactions, ligands were also conjugated to PEG through the acid moiety (**Figure 5.3)** to free the sterol oxygens to potentially interact with LXR. The hydroxyl of benzyl lithocholate (***2***) was protected with *tert*-butyldimethylsilyl chloride (TBDMS-Cl) in the presence of imidazole as an acid to generate ***5.*** The benzyl group was then removed via hydrogenolysis, and PEG was conjugated via

carbodiimide coupling to yield ***7***. To generate the free hydroxyl of ***8***, the TBDMS protecting group was cleaved using tetrabutylammonium fluoride (TBAF) under mildly acidic conditions.

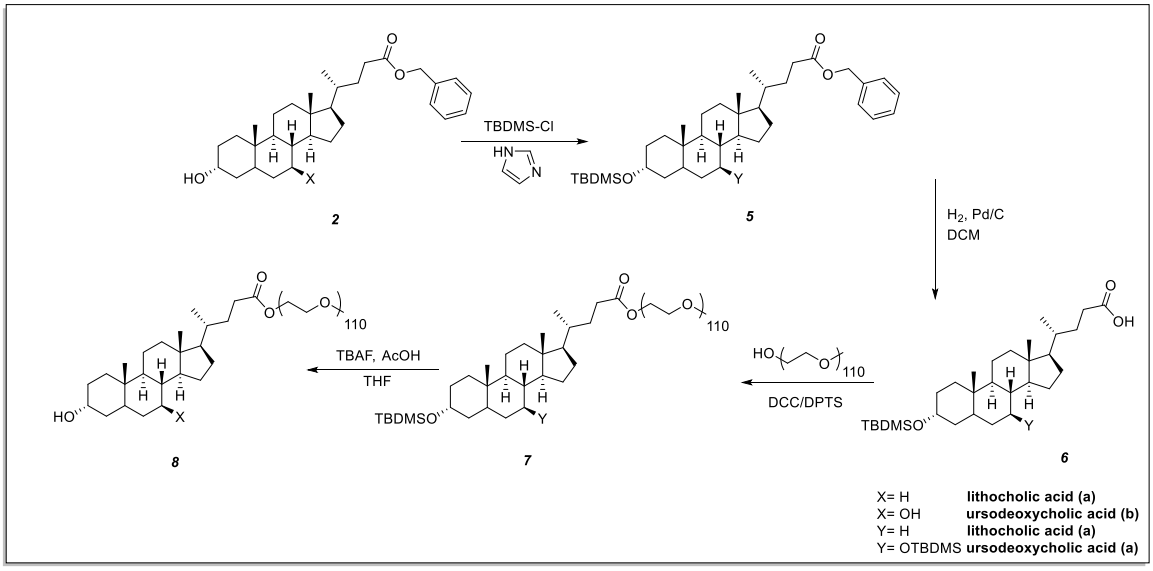

Figure 5.3: Representative synthesis of PEG-ligand conjugates bearing a free hydroxyl

The characterization of the synthetic approach, particularly the use of ^{1}H-NMR (**Figure 5.4**) to confirm the synthesis of ***4a*** will be used as an example. The successful synthesis of ***2a*** was confirmed by the presence of benzylic and aromatic protons at 5.12 ppm and 7.37 ppm respectively. FT-IR was also used to confirm the generation of ***2a*** by the disappearance of the carboxylic acid carbonyl and the generation of an ester carbonyl at 1737 cm^{-1}. The appearance and relative integration of a large PEG (3.58 ppm) and succinic linker peaks (2.61 ppm) as compared to methyl protons of ***1a***, in addition to the significant downfield chemical shift of proton at the 3 position (ipso to the hydroxyl of ***1a***) suggested successful synthesis of ***3a***. The complete absence of benzylic and aromatic protons confirmed successful benzyl deprotection and generation of ***4a***. Monodisperse peaks and molecular weight obtained from GPC measurements further confirmed complete conjugation of ***2a*** to PEG and preservation of esters upon benzyl deprotection of ***3a***.

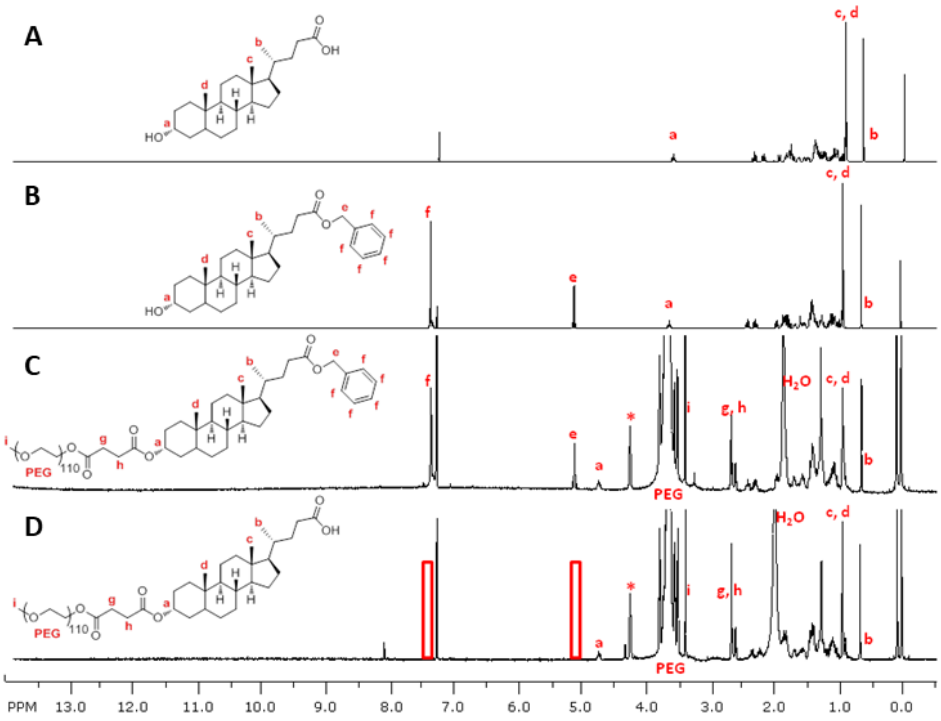

Figure 5.4. Stacked ^{1}H-NMR spectra of intermediates (LCA, ***2a***, ***3a***- A, B, C respectively) in the synthesis of PEG-LCA conjugate (***4a***- D). Peaks are labeled with letters corresponding to their structure for interpretation. Additionally, absence of peaks critical in confirming product identity are highlighted by red rectangles. The * represents the first methylene proton in PEG.

5.2.2. Self-Assembly Characterization of PEG-ligands

The ability of carboxylate-terminated compounds to self-assemble into micelles was evaluated by measuring critical micelle concentration (CMC) following a previously published pyrene-based assay [13], and micelle size was evaluated using dynamic light scattering (DLS). The results, shown in **Table 5.1.,** were compared to CMCs and micelle sizes of analogous 1cM conjugates bearing free carboxylates. CMC values of PEGylated compounds were both approximately an order-of-magnitude higher than their 1cM-conjugate counterparts. This is anticipated, as CMC values are generally lower when hydrophobicity, such as that imparted by large aliphatic region of 1cM, is increased for analogous structures [14]. Lower CMCs are desirable

for delivery applications, as they are more likely to resist dissociation upon dilution [15]. As such, 1cM based conjugates would be more likely to deliver encapsulated cargo to the site of arterial injury compared to PEGylated ligand conjugates. Micelle sizes are also significantly smaller for 1cM conjugates compared to PEGylated ligands, indicating improved stability and packing. This feature further suggests that 1cM conjugated ligands may demonstrate improved retention of encapsulated cargo upon systemic administration for biological applications.

Table 5.1. Self-assembly characteristics of LCA and ursodeoxycholic acid conjugates.

Compound	CMC (M)	Micelle size (nm)
4a	1×10^{-5}	170
4b	3×10^{-5}	179
1cMLCA	1×10^{-6}	26
1cMurso	5×10^{-6}	13

5.2.3. Nanoparticle Formulation

AMs have previously been evaluated for activity as both micelle and NP preparations. When comparing stability and activity results, NPs are superior. AM NPs exhibit higher stability and are not subject to dissociation upon dilution, they perform more effectively under serum containing conditions, and reduce oxLDL uptake more efficiently than micelle counterparts [16, 17]. As such, PEGylated ligands were formulated into NPs with various core molecules to establish compatible NP components and evaluate their effects on NP size and ζ potential. Core molecules evaluated in these experiments include M12, polystyrene (PS), and alkylLCA (described in Chapter 2). Results indicate that LCA-PEG conjugates (***4a*** and ***8a***) forms NPs of smaller diameter with either PS or alkylLCA when compared to NPs with M12 cores (**Table 5.2**). The smaller sizes of NPs with alkylLCA cores is likely attributable to favorable interactions between LCA moieties in

the core and shell. Similiarly, PS has planar moieties that are more likely to pack well with the LCA moieties on ***4a*** and ***8a*** compared to the long alkyl chains on M12. This is reflected in the comparably larger size of NPs with M12 cores. All evaluated NPs exhibited similar negative ζ potentials to those seen for AM-based NPs.

Table 5.2. Physicochemical characteristics of NPs prepared with LCA-PEG conjugates. NP formulations are written as Shell[Core]

NP Formulation	Hydrodynamic diameter (nm)	ζ Potential (mV)
4a[PS]	254	-25
4a[alkylLCA]	267	-21
4a[M12]	517	-23
8a[PS]	205	-20
8a[alkylLCA]	192	-21
8a[M12]	308	-20

5.2.4. Influence of Lithocholic Acid-Based Nanoparticles on Macrophage Gene Expression

Preliminary data entrapping LCA in the core of NPs suggested that it may agonize LXR, resulting in upregulation of genes that contribute to maintaining desirable lipid homeostasis. Therefore, NPs containing LCA-conjugates (i.e., AMs and hydrophobically modified cores) were evaluated for their impact on additional inflammatory cytokines and genes associated with lipid metabolism (**Table 5.3**). The genes evaluated include monocyte chemoattractant protein 1 (MCP-1), which is an inflammatory cytokine secreted to recruit monocytes to the site of arterial injury and matrix metalloproteinase (MMP9) which aids in the breakdown of the extracellular matrix and is associated with plaque disruption [18-20]. Lipid metabolism genes evaluated include sterol regulatory element binding protein 1 (SREBP1), a lipogenic transcription factor, peroxisome proliferator-activated receptor (PPARɣ), which leads to LXR induction and subsequent ABCA1

upregulation as well as regulation of oxLDL uptake SRs, LXRα and LXRβ, and the cholesterol efflux transporter ABCA1 [4, 21]. As shown in **Table 5.3**, there were no significant changes in transcription of any of these genes. It is possible that LCA conjugation through the hydroxyl moiety interferes with LXR interactions, polymer conjugation sterically hinders the ligand too much to interact with the narrow binding pocket, or the ligand is shielded from interactions in the NP formulation. This information provides critical details leading to the understanding of how LCA NP formulations result in ABCA1 upregulation as shown in the preliminary results. As the conjugation and subsequent NP formulation abolish activity, the next steps to understand these results would be to assess the micellar or unimeric activity of ligand conjugates. Doing so will provide pertinent information to determine if NP formulation or conjugation causes the discrepancy in results.

Table 5.3. Transcription levels of genes commonly associated with the atherosclerotic phenotype in human monocyte-derived macrophages treated with AM NPs.

	Inflammatory Cytokines		**Lipid Metabolism**				
	MCP-1	**MMP9**	**SREBP1**	**PPARγ**	**LXRα**	**LXRβ**	**ABCA1**
basal	1	1	1	1	1	1	1
1cM[M12]	2	2	1	0	2	-1	2
1cM[PS]	2	2	1	1	3	-1	1
1cM[alkylLCA]	2	2	1	1	3	-1	0
1cMLCA[M12]	2	2	1	-2	2	-1	1
1cMLCA[PS]	1	2	0	-1	2	-1	0
1cM[alkylLCA]	5	2	0	0	2	-1	1

5.2.5. Expression of LXR in *E. coli*

Gaining a better understanding of how LCA and ursodeoxycholic acid interact with LXR may provide foundational knowledge to generate ligand conjugates that retain the activity observed in preliminary results. As such, LXR was expressed in *E. coli* with the intent of performing binding

affinity studies and NMR experiments to determine the protein residues that interact with the ligands. Both isoforms of LXR were expressed in *E. coli* using various conditions to optimize expression levels and ease purification. Amplification of the plasmids was successful as confirmed via sequencing data of translated plasmid DNA (**Figure 5.6**).

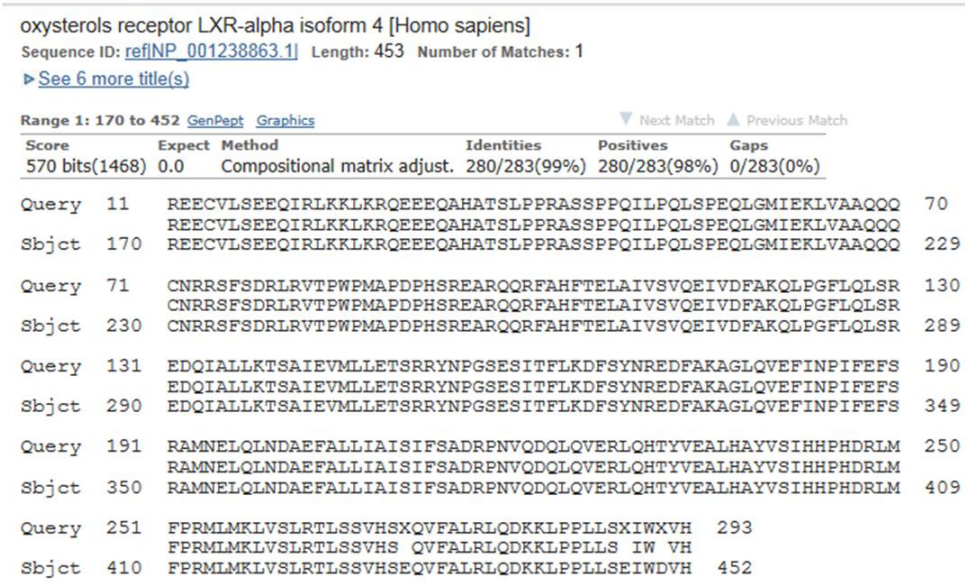

oxysterols receptor LXR-alpha isoform 4 [Homo sapiens]
Sequence ID: ref|NP_001238863.1| Length: 453 Number of Matches: 1
▸ See 6 more title(s)

Range 1: 170 to 452 GenPept Graphics ▼ Next Match ▲ Previous Match

Score	Expect	Method	Identities	Positives	Gaps
570 bits(1468)	0.0	Compositional matrix adjust.	280/283(99%)	280/283(98%)	0/283(0%)

```
Query  11   REECVLSEEQIRLKKLKRQEEEQAHATSLPPRASSPPQILPQLSPEQLGMIEKLVAAQQQ  70
            REECVLSEEQIRLKKLKRQEEEQAHATSLPPRASSPPQILPQLSPEQLGMIEKLVAAQQQ
Sbjct  170  REECVLSEEQIRLKKLKRQEEEQAHATSLPPRASSPPQILPQLSPEQLGMIEKLVAAQQQ  229

Query  71   CNRRSFSDRLRVTPWPMAPDPHSREARQQRFAHFTELAIVSVQEIVDFAKQLPGFLQLSR  130
            CNRRSFSDRLRVTPWPMAPDPHSREARQQRFAHFTELAIVSVQEIVDFAKQLPGFLQLSR
Sbjct  230  CNRRSFSDRLRVTPWPMAPDPHSREARQQRFAHFTELAIVSVQEIVDFAKQLPGFLQLSR  289

Query  131  EDQIALLKTSAIEVMLLETSRRYNPGSESITFLKDFSYNREDFAKAGLQVEFINPIFEFS  190
            EDQIALLKTSAIEVMLLETSRRYNPGSESITFLKDFSYNREDFAKAGLQVEFINPIFEFS
Sbjct  290  EDQIALLKTSAIEVMLLETSRRYNPGSESITFLKDFSYNREDFAKAGLQVEFINPIFEFS  349

Query  191  RAMNELQLNDAEFALLIAISIFSADRPNVQDQLQVERLQHTYVEALHAYVSIHHPHDRLM  250
            RAMNELQLNDAEFALLIAISIFSADRPNVQDQLQVERLQHTYVEALHAYVSIHHPHDRLM
Sbjct  350  RAMNELQLNDAEFALLIAISIFSADRPNVQDQLQVERLQHTYVEALHAYVSIHHPHDRLM  409

Query  251  FPRMLMKLVSLRTLSSVHSXQVFALRLQDKKLPPLLSXIWXVH  293
            FPRMLMKLVSLRTLSSVHS QVFALRLQDKKLPPLLS IW VH
Sbjct  410  FPRMLMKLVSLRTLSSVHSEQVFALRLQDKKLPPLLSEIWDVH  452
```

Figure 5.5. Gene sequencing data indicates that plasmid amplification was successful and corresponds to LXR. LXRα BLAST alignment is presented as an example.

Expression was evaluated in DE3(BL21) and DE3(BL21)pLysS at various induction points (i.e., OD_{600}= 0.2, 0.4, 0.6). Time points were taken at 2, 4, 6, 8, 24, and 36 h post induction. Results indicate that both proteins are expressed solely in inclusion bodies (**Figure 5.6.**), as no protein was detected in the soluble portion of homogenized cells as determined via His-Tag staining. Attempts were made to force expression out of inclusion bodies into the soluble fraction by lowering the induction temperature to 20 °C without success. As such, attempts were made to purify LXR from inclusion bodies, including denaturing with urea and β-mercaptoethanol (BME), followed by protein refolding via dialysis in buffers containing various additives (i.e., Arginine, Triton X, dithiothreitol) and various pH (i.e., 8.0, 8.5, 9.0). Despite many efforts, attempts resulted in

precipitated protein during dialysis. This was interpreted as unsuccessful attempts and proper protein folding could not be confirmed. To continue this project, more effective isolation and refolding procedures must be established to gain meaningful results.

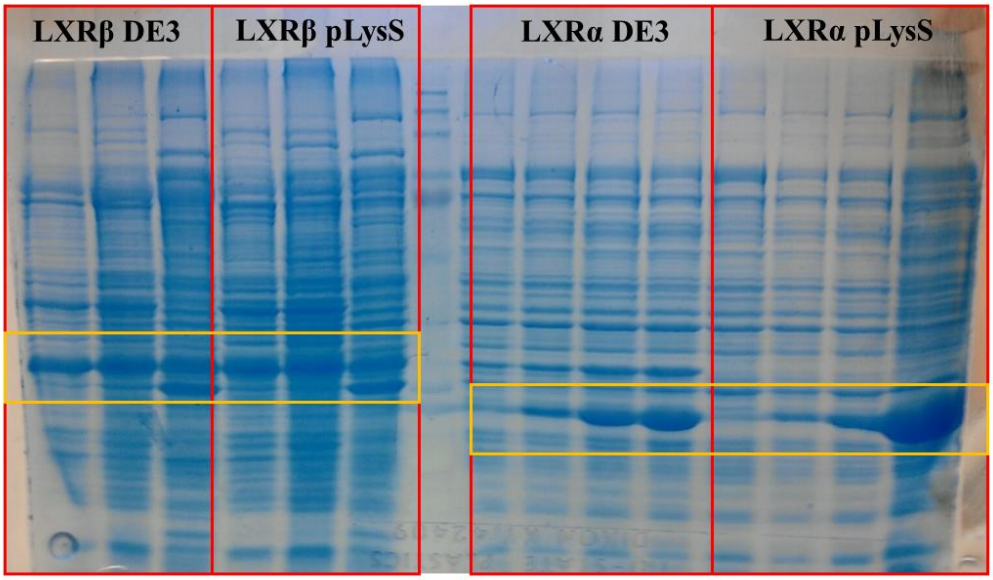

Figure 5.6. SDS-PAGE gels of LXRα and LXRβ expression in insoluble pellets from DE3(BL21) and DE3(BL21)pLysS *E. coli*. Lanes containing each cell type and LXR isoform are outlined in red boxes and LXR protein bands are outlined in yellow boxes.

5.3. Experimental

5.3.1. Synthesis of PEG-ligand Conjugates with Free Carboxylate

The synthesis of ***4a***, according to **Figure 5.2.**, will be presented as an example. The carboxylic acid of LCA (***1a***) was selectively protected using benzyl bromide under basic conditions. ***1a*** (2.66 mmol, 1.0 g) and potassium carbonate (3.19 mmol, 0.44 g) were suspended in dimethylformamide (DMF, 30 mL) under nitrogen. The reaction was allowed to stir for 30 min, followed by the slow addition of benzyl bromide (3.99 mmol, 0.47 mL). The reaction was stirred overnight. The reaction was diluted with diethyl ether (20 mL) and extracted 3X with sodium bicarbonate (20 mL) to remove unreacted ***1a***. The solvent was removed *in vacuo* and the resulting

solid triturated in hexanes to remove excess benzyl bromide to yield ***2a***. The product was conjugated to PEG-succinate via carbodiimide coupling. ***2a*** (0.11 mmol, 52 mg) and PEG succinate (0.05 mmol, 284 mg) were dissolved in dichloromethane (DCM, 5 mL) under nitrogen. 4-(dimethylamino)pyridinium-4-toluene sulfonate (DPTS, 0.083 mmol, 25 mg) was added followed by N,N'-dicyclohexylcarbodiimide (DCC, 1 M, 0.11 mmol, 0.1 mL), and the reaction stirred overnight. The reaction was cooled to 0 °C and urea byproduct removed via filtration. The filtrate was extracted 2X with 1N hydrochloric acid (HCl) and 1X with brine, followed by removal of solvent *in vacuo*. The product was precipitated in diethyl ether (15 mL) and collected by centrifugation (3500 rpm, 5 min) for a total of 5X to obtain ***3a***. The benzyl group was removed via hydrogenolysis with 10% Pd/C in DCM (5 mL) for 24 h. The heterogeneous mixture was then filtered through Celite® to remove Pd/C and the filtrate was removed *in vacuo* to obtain ***4a***.

5.3.2. Synthesis of PEG-ligand Conjugates with Free Hydroxyl

The hydroxyl o*f **2a*** was protected with TBDMSCl. ***2a*** (0.30 mmol, 140 mg) and imidazole (0.60 mmol, 40.8 mg) were dissolved in DMF (5 mL) under nitrogen. The reaction was cooled to 0 °C in an ice bath and TBDMS-Cl was separately dissolved in 1 mL of DMF and added to the reaction over 1 h. The reaction was allowed to reach room temperature and stir overnight. Volatiles were removed *in vacuo* and the crude product subjected to flash column chromatography (3:1 hexanes: ethyl acetate) to yield pure ***3a.*** The benzyl group was removed via hydrogenolysis with 10% Pd/C as a catalyst in DCM for 24 h. The heterogeneous mixture was then filtered through Celite® to remove Pd/C and the filtrate removed *in vacuo* to obtain ***6a***. The product was then directly PEGylated to yield ***7a*** via carbodiimide coupling. Water was azeotropically removed from PEG with toluene under reduced pressure 3X prior to use. mPEG-OH (0.04 mmol, 183 mg) was dissolved in DCM (5 mL) with ***6a*** (0.07 mmol, 35 mg) and DPTS (0.04 mmol, 10 mg) under nitrogen, followed by dropwise addition of DCC (1 M, 0.1 mmol, 0.1 mL) as a coupling reagent. After 24 h, the reaction was cooled to 0 °C and urea byproduct removed via filtration. The filtrate

was extracted 2X with 1N HCl and 1X with brine, followed by removal of solvent *in vacuo*. The product was precipitated in diethyl ether (15 mL) and collected by centrifugation (3500 rpm, 5 min) for a total of 5X to obtain ***7a***. The TBDMS protecting group was cleaved using excess tetrabutylammonium fluoride (TBAF, 1 M in tetrahydrofuran (THF)) under mildly acidic conditions via the addition of 0.1 mL of acetic acid. THF was removed *in vacuo* and the residue resuspended in DCM. The organic layer was washed 1X with saturated sodium bicarbonate, and 2X with deionized water. The organic layer was dried and the solvent removed *in vacuo* to obtain ***8a***.

5.3.3. Self-Assembly Characterization

Serial dilutions of each ligand-conjugate were made in deionized water from 10^{-3} M to 10^{-9} M. Aliquots of pyrene dissolved in acetone (10^{-6} M, 0.5 mL) were added to scintillation vials and the acetone evaporated. Aliquots (5 mL) of each ligand-conjugate dilution were added to pyrene films and incubated at 37 °C for 2 d. The fluorescence of each sample was measured with an emission wavelength of 390 nm, and an excitation range of 300-360 nm. As micelles are formed, pyrene maximum emission shifts from 332 to 334.5, and CMC values were taken as the inflection point when plotting the log of each concentration vs. the fluorescence ratio of $I_{334.5/332}$.

5.3.4. Nanoparticle Fabrication

[Nanoparticles were fabricated by Rebecca Chmielowski, Department of Chemical and Biochemical Engineering, Rutgers University, Piscataway, NJ]

NPs were fabricated via flash nanoprecipitation [22]. Ligand-conjugates (40 mg/mL) and hydrophobe (20 mg/mL) were separately dissolved in tetrahydrafuran (THF). A 1:1 v/v mixture of the ligand-conjugate:hydrophobe solution (0.5 mL) was filtered through a 0.2 μm PTFE filter, then rapidly mixed with phosphate buffered saline (PBS, 0.5 mL) in a confined impinging jet mixer, and

subsequently added to 4.5 mL of PBS. NP suspensions were dialyzed using a 6-8 kDa ultrafiltration membrane cut-off 3X against sterile PBS (2 L) for organic solvent removal.

5.3.5. Nanoparticle Characterization

[Nanoparticles were characterized by Rebecca Chmielowski, Department of Chemical and Biochemical Engineering, Rutgers University, Piscataway, NJ]

NP sizes and zeta (ζ) potential were measured by dynamic light scattering (DLS) using a Malvern-Zetasizer Nano Series (ZS90) in triplicate with a 90° scattering angle. NPs sizes and PDI were evaluated in PBS, and the Z-average was taken as the hydrodynamic diameter. Prior to analyzing ζ potential, NPs were dialyzed extensively against deionized water.

5.3.6. Gene Transcription

Gene expression (MCP-1, MMP9, SREBP-1, PPARɣ, LXRα, LXRβ, ABCA1) in human monocyte derived macrophages (hMDMs) was assessed using quantitative reverse transcription polymerase chain reaction (qRT-PCR). RNA was extracted from hMDMs 24 h after treatment with AM NPs or controls using an RNeasy Plus Mini Kit with Quiashredder columns according to supplier protocol. The concentration and purity of RNA was quantified using a Nanodrop 2000c. RNA was reverse transcribed to cDNA using a High Capacity cDNA Kit and RapidCycler thermal cycler (Idaho Technology). RT-PCR was carried out using a Lightcycler 480 (Roche) with Fast SYBR Green Master Mix for 45 cycles. Fold-change was calculated using ΔΔCt method and normalized to housekeeping genes (actin-β and GAPDH). All forward and reverse primers were designed by Harvard Primer Bank or Primer-BLAST and synthesized by Integrated DNA Technology.

5.3.7. LXR Expression

BL21(DE3) and BL21(DE3)pLysS competent *E. coli* cells were defrosted on ice. hLXRα-His6 and hLXRβ-His6 plasmids were added to cell suspensions and incubated on ice for 30 min.

Cells were heat shocked at 42 °C for 90 s, then incubated on ice for 2 min. Lysogeny Broth (LB, 1.0 mL) was added and the tubes inverted to aid mixing. Cells were grown at 37°C with shaking for 45 min. Cells were pelleted via centrifugation (5000 rpm, 3 min) and 850 µL of media removed. The cell pellet was resuspended in the remaining LB. Ampicillin (30 µL, 1:3 dilution of 2000X stock) was spread on LB-agar plates, followed by spreading of resuspended cells. Plates were grown overnight at 37 °C.

A single colony was added to LB (50 mL, 50 µg/mL ampicillin) and grown at 37 °C overnight to generate a starter culture. Sterile flasks were prepared containing 1.2 g of LB and 50 µg/mL ampicillin in 60 mL of water, and flasks were inoculated with 1 mL of starter culture. Cells were grown at 30 °C and the optical density at 600 nm (OD_{600}) was measured at predetermined time points. When the OD_{600} reached the desired reading, the flasks were cooled to 25 °C, and isopropyl β-D-1-thiogalactopyranoside (IPTG, 1 M) was added to induce expression. Aliquots were taken at predetermined time points to optimize conditions. Cells were harvested via centrifugation (3500 g for 15 min) and analyzed via sodium dodecyl sulfate polyacrylamide gel electrophoresis (SDS-PAGE).

Gels were run using 10% SDS gels in Tris-Glycine running buffer for 20 min at 100 V, followed by 1 h at 150 V. After running, gels were submerged in water and microwaved (1 min) for a total of 3 washes. Cells were then stained using Coomassie Safe Stain according to manufacturer protocol, and destained with deionized water. When staining for His-Tag, gels were first fixed in Fixing Solution (100 mL ethanol, 20 mL acetic acid, 80 mL water) for 1 h and stained with His-Tag Invision Stain following manufacturer protocol. Gels were destained with phosphate buffer (20 mM sodium phosphate, pH 7.8).

In an attempt to isolate LXR isoforms from inclusion bodies, urea was added to inclusion body precipitates to denature the protein. Protein was then placed in a dialysis membrane and dialyzed against different folding buffers. Folding buffers of the following recipes were utilized:

1.) 25 mM Tris buffer, 300 mM NaCl, 0.2 M arginine, 1% Triton X, pH 8.0

2.) 25 mM Tris buffer, 300 mM NaCl, 0.2 M arginine, 1% Triton X, pH 8.5

3.) 25 mM Tris buffer, 300 mM NaCl, 0.2 M arginine, 1% Triton X, pH 9.0

4.) 25 mM Tris buffer, 300 mM NaCl, 0.25 mM DTT, pH 8.5

5.5 References

[1] Moore KJ, Tabas I. Macrophages in the pathogenesis of atherosclerosis. Cell. 2011;145:341-55.

[2] Hansson GK, Libby P. The immune response in atherosclerosis: a double-edged sword. Nature reviews Immunology. 2006;6:508.

[3] Ohashi R, Mu H, Wang X, Yao Q, Chen C. Reverse cholesterol transport and cholesterol efflux in atherosclerosis. QJM: An International Journal of Medicine. 2005;98:845-56.

[4] Chawla A, Boisvert WA, Lee C-H, Laffitte BA, Barak Y, Joseph SB, et al. A PPARγ-LXR-ABCA1 pathway in macrophages is involved in cholesterol efflux and atherogenesis. Molecular cell. 2001;7:161-71.

[5] Bodzioch M, Orsó E, Klucken J, Langmann T, Böttcher A, Diederich W, et al. The gene encoding ATP-binding cassette transporter 1 is mutated in Tangier disease. Nature genetics. 1999;22.

[6] Brooks-Wilson A, Marcil M, Clee SM, Zhang L-H, Roomp K, van Dam M, et al. Mutations in ABC1 in Tangier disease and familial high-density lipoprotein deficiency. Nature genetics. 1999;22.

[7] Janowski BA, Grogan MJ, Jones SA, Wisely GB, Kliewer SA, Corey EJ, et al. Structural requirements of ligands for the oxysterol liver X receptors LXRα and LXRβ. Proceedings of the National Academy of Sciences. 1999;96:266-71.

[8] Iverson NM, Plourde NM, Sparks SM, Wang J, Patel EN, Shah PS, et al. Dual use of amphiphilic macromolecules as cholesterol efflux triggers and inhibitors of macrophage athero-inflammation. Biomaterials. 2011;32:8319-27.

[9] Kalaany NY, Mangelsdorf DJ. LXRS and FXR: the yin and yang of cholesterol and fat metabolism. Annu Rev Physiol. 2006;68:159-91.

[10] Wang J, Plourde NM, Iverson N, Moghe PV, Uhrich KE. Nanoscale amphiphilic macromolecules as lipoprotein inhibitors: the role of charge and architecture. International journal of nanomedicine. 2007;2:697.

[11] Hofmann AF, Mysels KJ. Bile acid solubility and precipitation in vitro and in vivo: the role of conjugation, pH, and Ca2+ ions. Journal of lipid research. 1992;33:617-26.

[12] Mukhopadhyay S, Maitra U. Chemistry and biology of bile acids. Current Science. 2004;87:1666-83.

[13] Tian L, Yam L, Zhou N, Tat H, Uhrich KE. Amphiphilic scorpion-like macromolecules: design, synthesis, and characterization. Macromolecules. 2004;37:538-43.

[14] Chen L-J, Lin S-Y, Huang C-C. Effect of hydrophobic chain length of surfactants on enthalpy− entropy compensation of micellization. The Journal of Physical Chemistry B. 1998;102:4350-6.

[15] Trivedi R, Kompella UB. Nanomicellar formulations for sustained drug delivery: strategies and underlying principles. Nanomedicine (London, England). 2010;5:485-505.

[16] York AW, Zablocki KR, Lewis DR, Gu L, Uhrich KE, Prud'homme RK, et al. Kinetically Assembled Nanoparticles of Bioactive Macromolecules Exhibit Enhanced Stability and Cell-Targeted Biological Efficacy. Advanced Materials. 2012;24:733-9.

[17] Chan JW, Lewis DR, Petersen LK, Moghe PV, Uhrich KE. Amphiphilic macromolecule nanoassemblies suppress smooth muscle cell proliferation and platelet adhesion. Biomaterials. 2016;84:219-29.

[18] Loftus IM, Naylor AR, Goodall S, Crowther M, Jones L, Bell PR, et al. Increased matrix metalloproteinase-9 activity in unstable carotid plaques. A potential role in acute plaque disruption. Stroke. 2000;31:40-7.

[19] Gough PJ, Gomez IG, Wille PT, Raines EW. Macrophage expression of active MMP-9 induces acute plaque disruption in apoE-deficient mice. Journal of Clinical Investigation. 2006;116:59-69.

[20] Kanda H, Tateya S, Tamori Y, Kotani K, Hiasa K-i, Kitazawa R, et al. MCP-1 contributes to macrophage infiltration into adipose tissue, insulin resistance, and hepatic steatosis in obesity. Journal of Clinical Investigation. 2006;116:1494.

[21] Li Y, Xu S, Jiang B, Cohen RA, Zang M. Activation of sterol regulatory element binding protein and NLRP3 inflammasome in atherosclerotic lesion development in diabetic pigs. PloS one. 2013;8:e67532.

[22] York AW, Zablocki KR, Lewis DR, Gu L, Uhrich KE, Prud’homme RK, et al. Kinetically Assembled Nanoparticles of Bioactive Macromolecules Exhibit Enhanced Stability and Cell-Targeted Biological Efficacy. Advanced materials (Deerfield Beach, Fla). 2012;24:733-9.

6. APPENDIX B: GREEN SYNTHESIS OF ALKYLATED SUGARS AND AMPHIPHILIC MACROMOLECULES

6.1. Results and Discussion

In the past several decades, the increasing prevalence of sustainability has led to a surge in "greening" synthetic procedures. This trend is present at the academic level as well as the industry level in pharmaceutical and personal care products [1-3]. While green chemistry has a foundation in sustainability, it also seeks to reduce hazards associated with particular chemicals and processes to ensure the safety of the scientist, as well as the environment [4]. Anastas and Warner define green chemistry as "the utilization of a set of principles that reduces or eliminates the use or generation of hazardous substances in the design, manufacture and applications of chemical products."[4]

This subsection summarizes attempts and successful steps taken towards greening the synthesis of foundational molecules used in the Uhrich lab to mitigate the generation of hazardous substances and reduce the generation of waste. These molecules include M12 and T12, the two most commonly used hydrophobic domains for small molecule and polymeric amphiphiles synthesized in the Uhrich lab (**Figure 6.1,** left). It also includes 1cM and 1cT, the amphiphilic polymeric compounds generated from conjugating M12 or T12 to poly(ethylene glycol) (PEG) (**Figure 6.1**, right).

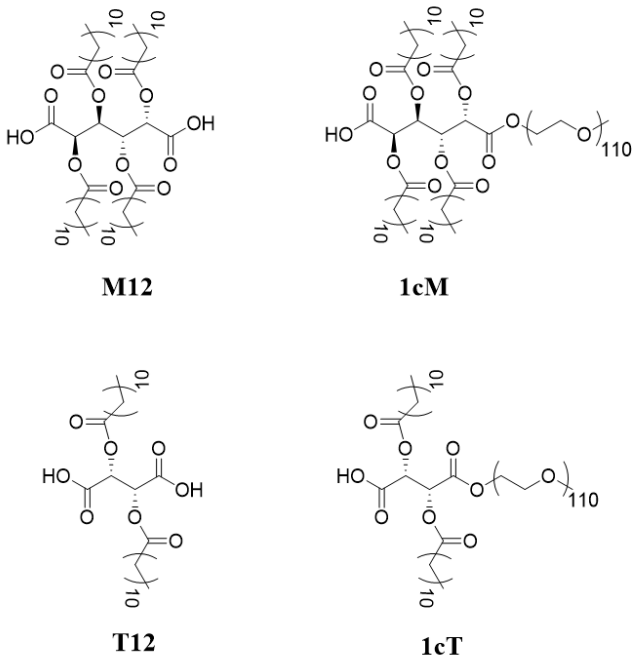

Figure 6.1. Chemical structures of foundational molecules for which green syntheses were attempted. Hydrophobes, M12 and T12 are shown on the left, and AMs 1cM and 1cT are shown on the right.

6.1.1. Preparation of T12 with Pyridine

Procedures used by the Uhrich group to synthesize the commonly used hydrophobic domains, M12 and T12, utilize excess acid chloride (i.e., 50 eq.) [5]. Doing so generates a large amount of hazardous waste and quenching excess acid chloride generates hydrogen gas, which is highly flammable. As such, the reaction was modified to use only a slight excess of acid chloride (i.e., 4 eq.), pyridine as a catalyst, and a green solvent, 2-methyltetrahydrofuran (2-MeTHF) to aid reaction mixing (**Figure 6.2**). 2-MeTHF is a green alternative to traditional synthetic reaction solvents, as it can be derived from renewable resources (e.g., furfural) and has excellent stability compared to analogous solvents such as THF [6].

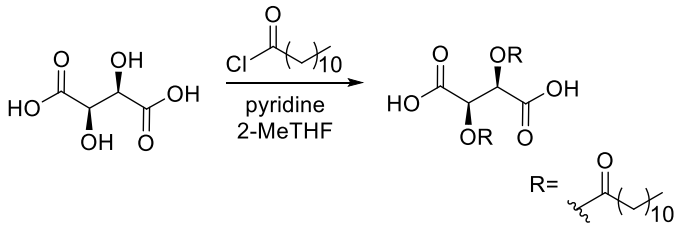

Figure 6.2. Synthetic approach utilized to green the synthesis of T12.

The synthesis of T12 using just double stoichiometric amounts of lauroyl chloride was successful as evidenced by ^{1}H-NMR, as shown in **Figure 6.3.** The product was isolated in high purity, but only a yield of 15 % was obtained, compared to ~70 % yield using traditional approaches. While progress was made in utilizing greener reaction conditions, yield was significantly compromised. To be considered as a viable alternative, reaction conditions require optimization.

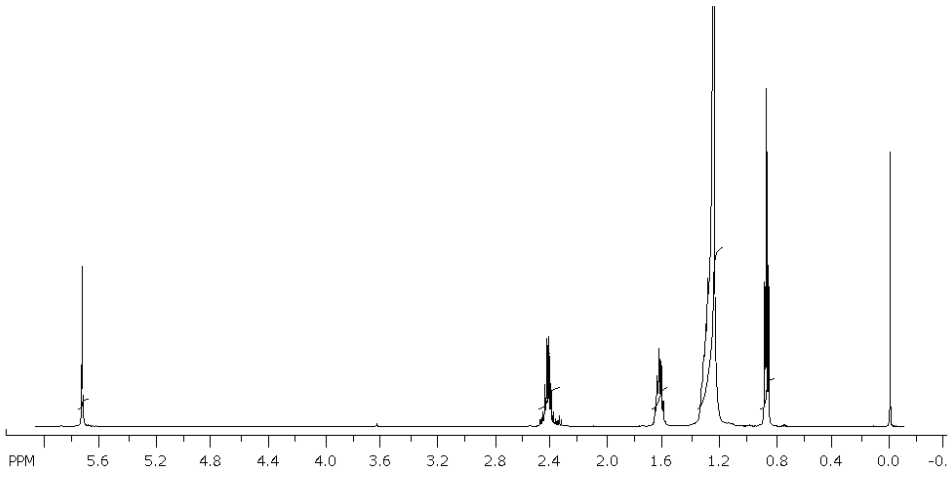

Figure 6.3. ^{1}H-NMR of T12 synthesized using green alternative approaches.

Synthesis of T12 with pyridine as the catalyst was also attempted in cyclopentylmethylether (CPME). Compared to ethereal solvents, CPME has low peroxide formation and high boiling point (i.e., 106 °C), reducing explosion and inhalation risks to the chemist [7]. Although product was successfully generated and collected via hexanes precipitation, it was significantly contaminated with pyridine. Future attempts to isolate the product with more

thorough washing or slower precipitation may yield pure product. Similar reaction conditions with 4 equivalents of pyridine in 2-MeTHF, with temperatures up to 80 °C, were also attempted for the synthesis of M12, but yielded no product, likely due to the insolubility of mucic acid.

6.1.2. Solventless Preparation of 1cM and 1cT

The preparation of 1cM and 1cT requires a co-solvent system of dichloromethane (DCM) and dimethylformamide (DMF). DCM is a potential carcinogen, rapidly permeates most commonly utilizes laboratory gloves, and has a low boiling point, exposing the chemist to toxic fumes [8]. DMF is mutagenic, has known reproductive and teratogenic effects, and decomposes to toxic gases upon exposure to high temperatures [9]. One approach to green synthetic reactions is to generate the same product via a solventless system to reduce the amount of waste generated, which also eliminates the hazards associated with the solvent. As such, the synthesis of 1cM and 1cT were attempted via a solventless reaction using *para*-toluenesulfonic acid (PTSA) under melt conditions (**Figure 6.4.**) following literature precedence [10].

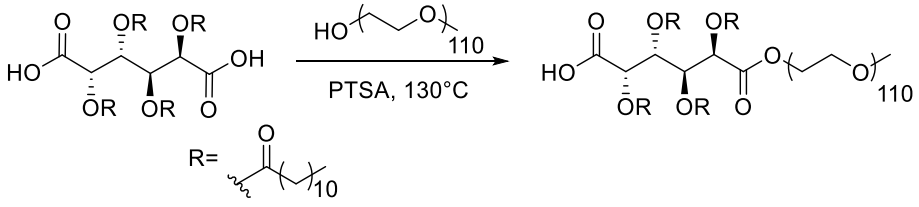

Figure 6.4. General solventless synthetic approach used to generate AMs.

This synthetic approach successfully yielded both 1cM and 1cT as evidenced by ^{1}H-NMR spectroscopy (**Figure 6.5.**). During the reaction, PEG melts and appears to dissolve the other reactant. After only a few hours, pure product can be obtained using traditional work-up procedures. This synthetic approach offers a potential green alternative by reducing safety hazards and hazardous waste generation. Attempts were also made to directly PEGylate mucic acid under identical reaction conditions without success.

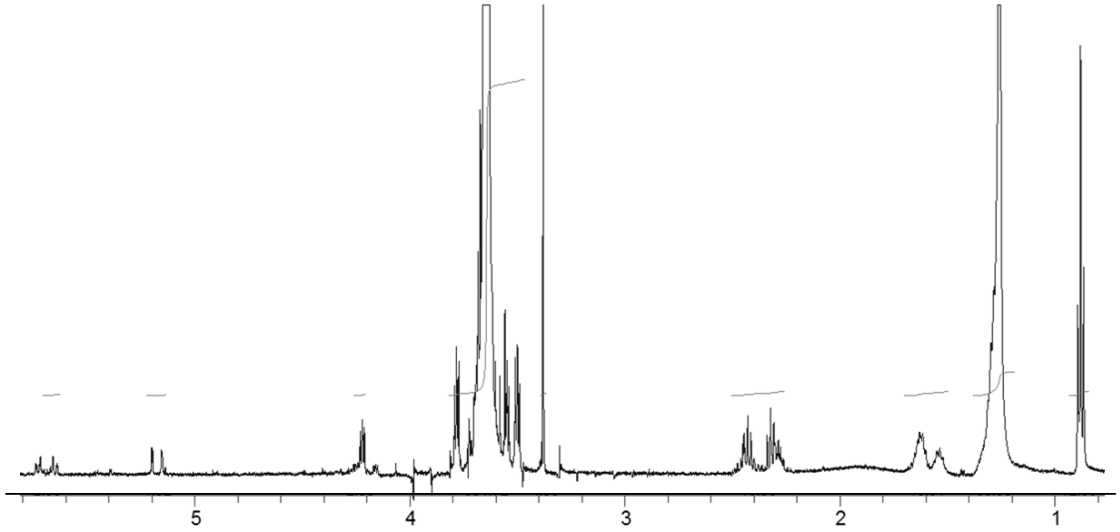

Figure 6.5. ^{1}H-NMR spectrum of pure 1cM isolated from solventless reaction of PEG and M12 catalyzed by PTSA.

6.1.3. Synthesis of 1cT with Alternative Coupling Agents

The traditional synthesis of 1cM and 1cT utilize N,N'-dicyclohexylcarbodiimide (DCC) as the coupling reagent. DCC is a skin and lung sensitizer that poses potential health hazards, particularly to individuals that use the chemical repeatedly [11]. (1-Cyano-2-ethoxy-2-oxoethylidenaminooxy)dimethylamino-morpholino-carbenium hexafluorophosphate (COMU) is a potential alternative to DCC as it is it does not contain a benzotriazole moiety, rendering it non-explosive, and the byproducts are water soluble, easing product purification [12]. COMU has demonstrated high efficiency in peptide coupling reactions, and was thus, attempted using -NH_2 terminated PEG rather than -OH terminated PEG following the scheme in **Figure 6.6.** [13].

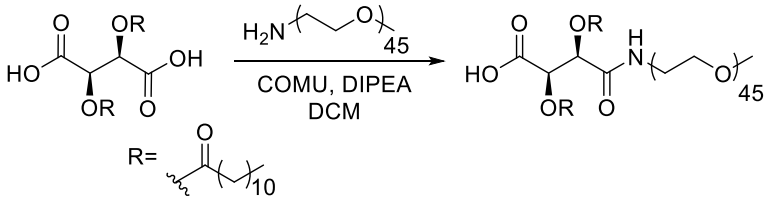

Figure 6.6. Synthetic approach used to generate 1cT-amide using COMU as coupling agent

1cT-amide was successfully generated using this approach as evidenced by ^{1}H-NMR spectroscopy. In an effort to further green the protocol, DCM was replaced with 2-MeTHF. Doing so would not only reduce the hazards associated with DCM, but it could also potentially increase yields. The workup protocol requires an extraction, in which DCM is the solvent for the organic phase. This extraction is highly prone to emulsion formation and DCM must be drained from the separatory funnel and replaced during each wash. Both factors likely lead to loss of product via transfer between several pieces of glassware. Despite attempts at replacing the solvent, no product was generated.

6.1.4. Alternative Work-Up Procedures for Isolation of M12

As no alternative reaction conditions resulted in successful synthesis of M12, efforts were made to reduce generated waste and hazards associated with the purification protocol. M12 solubility was evaluated in green solvents, including 2-MeTHF and CPME, and was found to be soluble in 2-MeTHF but insoluble in CPME. As such, diethyl ether was replaced with 2-MeTHF for the extraction and hexanes was replaced with CPME for the isolation step of the traditional protocol. Doing so was successful in isolating pure product. Isolation via centrifugation was most effective, as less solvent had to be used to wash and purify the product. The product could also be isolated via vacuum filtration, but required copious amounts (~20 mL compared to ~5 mL) of CPME to yield pure product.

6.2. Experimental

6.2.1. Preparation of T12 with pyridine

Tartaric acid (3.3 mmol, 0.50 g) and lauroyl chloride (13.3 mmol, 3.06 mL) were added to a round bottom flask and dissolved in 2-MeTHF (2.0 mL) under nitrogen. The reaction was stirred at room temperature for 24 h. The formed precipitate was vacuum filtered and the filtrate washed with deionized water (15 mL, 2X) and brine (15 mL, 1X). The organic layer was concentrated *in*

vacuo and poured over chilled hexanes (800 mL) on ice. The reaction was allowed to stir for 30 min, followed by vacuum filtration.

T12: Yield: 15% (brown solid) ^{1}H-NMR (500 MHz, $CDCl_3$): δ 0.89 (t, 6H), 1.25 (m, 32 H), 1.64 (m, 4H), 2.43 (m, 4H), 5.75 (s, 2H)

6.2.2. Solventless Preparation of 1cM and 1cT

mPEG-OH was azeotropically dried with toluene prior to use. M12 (0.25 mmol, 0.25 g), mPEG-OH (0.10 mmol, 0.50 g), and PTSA were added to a round bottom flask with a stir bar. The flask was heated to 130 °C with stirring under nitrogen for 3 h. The reaction was cooled to room temperature and dicholoromethane (DCM, 10 mL) and a minimal amount of dimethylformamide (DMF, ~1 mL) was added to the reaction flask to solubilize the contents. The reaction was washed with hydrochloric acid (HCl, 1 N, 10 mL, 1X) and brine (2X). The organic layer was dried over magnesium sulfate ($MgSO_4$) and the solvent removed *in vacuo*. The product was then precipitated in cold diethyl ether and isolated via centrifugation (3500 rpm, 5 min, 5X).

1cM: Yield: 78% (white solid) ^{1}H-NMR (500 MHz, $CDCl_3$): δ 0.87 (t, 12H), 1.26 (m, 64H), 1.60 (d of m, 8H), 2.42 (d of m, 8H), 3.37 (s, 3H), 3.62 (m, ~500 H), 4.22 (m, 2H), 5.14 (d, 2H), 5.72 (d of d, 2H). MALDI: Mw= 5.4

1cT: Yield: 40% (white solid) ^{1}H-NMR (500 MHz, $CDCl_3$): δ 0.86 (t, 6H), 1.26 (m, 32H), 1.61 (m, 4H), 2.31 (m, 4H), 3.39 (s, 3H), 3.65 (m, ~500 H), 4.22 (m, 2H), 5.44 (d, 2H)

6.2.3. Synthesis of 1cT with Alternative Coupling Agents

mPEG-NH_2 (2kDa) was azeotropically dried with toluene prior to use. mPEG-NH_2 (0.10 mmol, 200 mg) was dissolved in DCM (7.0 mL) under nitrogen. T12 (0.30 mmol, 145 mg) and diisoproylethylamine (DIPEA, 0.20 mmol, 0.04 mL) were added to the reaction flask and allowed

to stir for 15 min. (COMU, 0.15 mmol, 64 mg) was added and the reaction allowed to stir for 24 h. The reaction was washed with HCl (1N, 10 mL, 4X) and dried over $MgSO_4$. The organic solvent was removed *in vacuo* and the product precipitated in diethyl ether (40 mL). The product was isolated by centrifugation (3500 rpm, 5 min, 5X).

1cT: (white solid) ^{1}H-NMR (500 MHz, $CDCl_3$): δ 0.87 (t, 6H), 1.26 (m, 32H), 1.63 (m, 4H), 2.42 (m, 4H), 3.38 (s, 3H), 3.65 (m, ~200 H), 5.55 (s, 2H)

6.2.4. Alternative Work-Up Procedures for Isolation of M12

The standard synthetic protocol for generation of M12 was carried out as previously reported. Aliquots were taken following the reaction for alternative work up procedures.

The aliquot volume (~1 mL) was diluted with 2-MeTHF (1.0 mL) and washed with deionized water (2 mL, 5X). The organic layer was concentrated *in vacuo* and CPME (2.0 mL) was added to precipitate M12. The product was isolated via centrifugation (3500 rpm, 5 min) and washed with CPME (3 mL, 2X) to isolate the pure product as a white powder.

M12: (white solid). ^{1}H-NMR (500 MHz, $CDCl_3$): δ 0.64 (t, 12H), 1.03 (m, 64H), 1.35 (d of m, 8H), 2.1 (d of m, 8H), 4.84 (s, 2H), 5.48 (s, 2H).

6.3. References

[1] Constable DJ, Dunn PJ, Hayler JD, Humphrey GR, Leazer Jr JL, Linderman RJ, et al. Key green chemistry research areas—a perspective from pharmaceutical manufacturers. Green Chemistry. 2007;9:411-20.

[2] Clark JH. Green chemistry: today (and tomorrow). Green Chemistry. 2006;8:17-21.

[3] Anastas PT, Beach ES. Changing the Course of Chemistry. Green Chemistry Education: American Chemical Society; 2009. p. 1-18.

[4] Anastas PT, Warner JC. Green chemistry: theory and practice: Oxford university press; 2000.

[5] Tian L, Yam L, Zhou N, Tat H, Uhrich KE. Amphiphilic scorpion-like macromolecules: design, synthesis, and characterization. Macromolecules. 2004;37:538-43.

[6] Pace V, Hoyos P, Castoldi L, Domínguez de María P, Alcántara AR. 2-Methyltetrahydrofuran (2-MeTHF): A Biomass-Derived Solvent with Broad Application in Organic Chemistry. ChemSusChem. 2012;5:1369-79.

[7] Watanabe K. The Toxicological Assessment of Cyclopentyl Methyl Ether (CPME) as a Green Solvent. Molecules. 2013;18:3183.

[8] Material Safety Data Sheet- Dichloromethane. In: ScienceLab.com, editor. http://wwwsciencelabcom/msdsphp?msdsId=99260602013.

[9] Material Safety Data Sheet- N,N-Dimethylformamide. In: ScienceLab.com, editor. http://wwwsciencelabcom/msdsphp?msdsId=99238132013.

[10] Molinero L, Ladero M, Tamayo JJ, García-Ochoa F. Homogeneous catalytic esterification of glycerol with cinnamic and methoxycinnamic acids to cinnamate glycerides in solventless medium: Kinetic modeling. Chemical Engineering Journal. 2014;247:174-82.

[11] Material Safety Data Sheet- N,N-Dicyclohexylcarbodiimide. In: ScienceLab.com, editor. http://wwwsciencelabcom/msdsphp?msdsId=99237402013.

[12] El-Faham A, Funosas RS, Prohens R, Albericio F. COMU: A Safer and More Effective Replacement for Benzotriazole-Based Uronium Coupling Reagents. Chemistry-A European Journal. 2009;15:9404-16.

[13] El-Faham A, Albericio F. Peptide Coupling Reagents, More than a Letter Soup. Chemical Reviews. 2011;111:6557-602.

7. APPENDIX C: SMALL CATIONIC AMPHIPHILES BEARING MULTIPLE CHARGES FOR ANTIMICROBIAL APPLICATIONS

7.1. Results and Discussion

Previous studies have confirmed that the hydrophilic lipophilic balance (HLB) of cationic amphiphilic molecules (CAms) is critical to activity and specificity for bacterial cells over mammalian cells [1-3]. As such, a series of CAms was synthesized with two cationic charges and a single alkyl chain of varying length and hydrophobic characteristics. Alkyl chain length was varied by conjugating various fatty acids to the cationic head group, and hydrophobic structure was varied by incorporating double bonds in the hydrophobic domain.

CAm synthesis was carried out according to **Figure 7.1.** Boc-protected diaminopropanol (***1***) was conjugated to each fatty acid using standard carbodiimide coupling procedures. Boc-groups were removed with hydrochloric acid (HCl) in dioxane to generate the final products (***3***) as chloride salts as confirmed via ^{1}H-NMR.

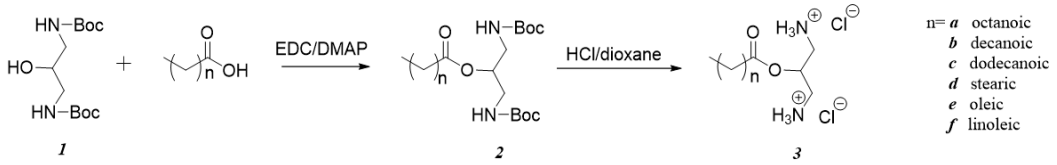

Figure 7.1. Synthetic approach used to generate CAms with two cationic head groups and a single alkyl tail. Fatty acid identities are indicated for each CAm.

Following successful synthesis, CAms were evaluated for cytotoxicity against a model mammalian fibroblast cell line. All CAms displayed very high levels of cytotoxicity and were not further pursued for antimicrobial applications (**Figure 7.2.**). CAms with eighteen carbon long fatty acid tails killed all cells at concentrations as low as 10 μg/mL. However, shorter tail lengths (i.e., eight to ten carbons) clearly demonstrated that hydrophobic tail length was directly

correlated with poor cytocompatibility. The shortest tail length, eight carbons, had the most desirable cytocompatibility profile, being cytocompatible at 10 µg/mL, with approximately 50% viable cells remaining at 100 µg/mL after 24 h. While these results are not desirable, they reveal pertinent information that can aid in the development of future CAm generations.

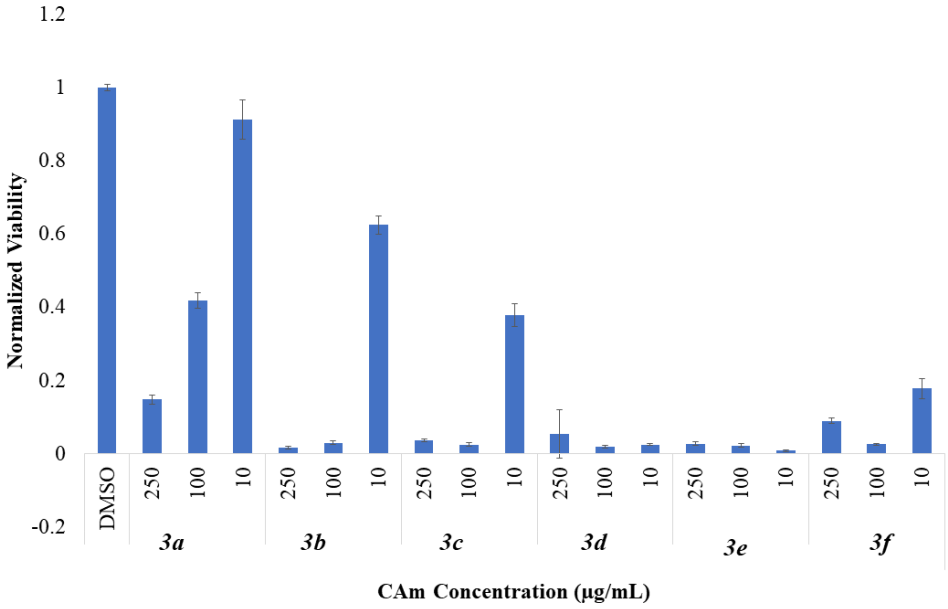

Figure 7.2. Cytocompatibility profiles of CAms against 3T3 fibroblasts after 24 h indicating an increase in toxicity with increasing alkyl chain length.

7.2. Experimental

7.2.1. Synthesis of Boc-Protected CAms with Multiple Charges

Synthesis of ***2b*** will be presented as an example. Dodecanoic acid (0.61 mmol, 0.67 g) and 4-dimethylaminopyridine (DMAP, 1.0 mmol, 0.13 g) were dissolved in dichloromethane (DCM) under nitrogen with stirring. ***1*** (0.47 mmol, 0.15 g) was added, followed by (EDC, 1.0 mmol, 0.13 g). The reaction was stirred overnight at room temperature. The crude mixture was washed with potassium bisulfate (10%, 15 mL, 2X) and brine (15 mL, 1X) and the organic layer

dried over $MgSO_4$, filtered and concentrated *in vacuo*. The crude mixture was purified via column chromatography with ethyl acetate: hexanes (1:1). ***2*** was obtained as a clear oil.

2a: Yield: 42% (clear oil) ^{1}H-NMR (500 MHz, $CDCl_3$): δ 0.86 (t, 3H), 1.27 (m, 14C), 1.42 (s, 18C), 1.62 (m, 2H), 2.29 (t, 2H), 3.31 (m, 4H), 4.85 (br, 2H), 5.64 (m, 1H).

2b: Yield: 68% (clear oil) ^{1}H-NMR (500 MHz, $CDCl_3$): δ 0.87 (t, 3H), 1.25 (m, 16C), 1.42 (s, 18C), 1.56 (m, 2H), 2.28 (t, 2H), 3.29 (m, 4H), 4.92 (br, 2H), 5.67 (m, 1H).

2c: Yield: 69% (clear oil) ^{1}H-NMR (500 MHz, $CDCl_3$): δ 0.87 (t, 3H), 1.42 (m, 18C), 1.53 (s, 18C), 1.60 (m, 2H), 2.29 (t, 2H), 3.28 (m, 4H), 4.93 (br, 2H), 5.61 (m, 1H).

2d: Yield: 72% (clear oil) ^{1}H-NMR (500 MHz, $CDCl_3$): δ 0.88 (t, 3H), 1.27 (m, 28C), 1.42 (m, 18C), 1.66 (m, 2H), 2.30 (t, 2H), 3.18 (m, 4H), 4.25 (br, 2H), 5.44 (m, 1H).

2e: Yield: 52% (clear oil) ^{1}H-NMR (500 MHz, $CDCl_3$): δ 0.89 (t, 3H), 1.27 (m, 34H), 1.42 (m, 18C), 1.62 (m, 2C), 2.0 (t, 2H), 2.40 (m, 2H), 3.20 (m, 4H), 5.33 (q, 2H), 5.44 (m, 1H).

2f: Yield: 38% (yellow oil) ^{1}H-NMR (500 MHz, $CDCl_3$): δ 0.88 (t, 3H), 1.29 (m, 14H), 1.42 (m, 18C), 1.61 (m, 2C), 2.03 (t, 4H), 2.41 (m, 2H), 2.83 (t, 2H), 4.69 (br, 2H), 5.33 (m, 4H), 5.45 (m, 1H).

7.2.2. Synthesis of CAms with Multiple Charges

2 was suspended in HCl in dioxane (4 M, 5 mL) at 0 °C. The reaction was stirred for 20 min on ice then allowed to warm to room temperature and stir overnight. Volatiles were removed *in vacuo* and the product precipitated in cold diethyl ether (15 mL).

7.3. References

[1] Faig A, Arthur TD, Fitzgerald PO, Chikindas M, Mintzer E, Uhrich KE. Biscationic tartaric acid-based amphiphiles: charge location impacts antimicrobial activity. Langmuir. 2015;31:11875-85.

[2] Zhang Y, Algburi A, Wang N, Kholodovych V, Oh DO, Chikindas M, et al. Self-assembled cationic amphiphiles as antimicrobial peptides mimics: Role of hydrophobicity, linkage type, and assembly state. Nanomedicine: Nanotechnology, Biology and Medicine. 2017;13:343-52.

[3] Strøm MB, Haug BE, Skar ML, Stensen W, Stiberg T, Svendsen JS. The pharmacophore of short cationic antibacterial peptides. Journal of medicinal chemistry. 2003;46:1567-70.